

**A Thesis Submitted for the Degree of PhD at the University of Warwick**

**Permanent WRAP URL:**

<http://wrap.warwick.ac.uk/98307>

**Copyright and reuse:**

This thesis is made available online and is protected by original copyright.

Please scroll down to view the document itself.

Please refer to the repository record for this item for information to help you to cite it.

Our policy information is available from the repository home page.

For more information, please contact the WRAP Team at: [wrap@warwick.ac.uk](mailto:wrap@warwick.ac.uk)

GRAIN BOUNDARY ENERGIES  
IN COPPER

by

RAMLI OMAR

A thesis submitted to the University of Warwick for admission  
to the degree of Doctor of Philosophy.

Department of Physics  
University of Warwick  
COVENTRY CV4 7AL

April 1987

ABSTRACT

The dependence of grain boundary energy on boundary orientation was studied in copper annealed at 1000°C. Grain boundary orientations and the disorientations across the boundaries were measured. A rotation matrix notation is used to interpret selected area electron channelling patterns observed in a scanning electron microscope. The Herring and Shewmon torque terms were investigated using wire specimens having a "bamboo" structure. The Herring torque terms were determined using the Hess relation. The (110) section of the  $\Sigma_{11}$   $\gamma$ -plot (i.e. the variation of grain boundary energy with boundary orientation) was evaluated. In this plot, minima in energies were found at the (311) and (332) mirror planes.  $\Sigma_3$  and  $\Sigma_9$  boundaries were investigated in sheet specimens. The (110) and (111) sections of the  $\Sigma_3$   $\gamma$ -plot were evaluated. In addition to the sharp cusps occurring at the  $\Sigma_3$  {111} planes, the further shallower cusps occur at the incoherent  $\Sigma_3$  boundaries with the interfacial planes approximately parallel to {322} in one crystal and {11.44} in the other crystal. Flat and curved  $\Sigma_9$  boundaries were investigated. The break up of  $\Sigma_9$  boundaries into two  $\Sigma_3$  boundaries and the relation between the  $\Sigma_3$  and  $\Sigma_9$   $\gamma$ -plots was also examined. The (110) section of the  $\Sigma_9$   $\gamma$ -plot was constructed.

ACKNOWLEDGEMENTS

I wish to express my deep and sincere gratitude to my supervisor, Dr. Helmut Mykura, for introducing me to an interesting field of study and for his constant encouragement and guidance throughout this work and in the preparation of this thesis.

I would also like to thank the numerous other people who assisted me during this work, especially Mr. Gerald Smith and Mr. Steve York for their technical assistance, Mr. Roy McLeod for help in the production of some of the photographs and Mrs. Catherine Gow for typing the thesis.

I am indebted to the Malaysian Government for the granting of a studentship during the period of study.

I wish to record my love and deep thanks to my wife, Naini, for her unlimited encouragement over the years. My love to my daughters, Nur Adyani and Nur Ilani, for their patience. Sincere thanks to my family in Malaysia for their unfailing support and encouragement.

DECLARATION

This thesis is submitted to the University of Warwick in support of my application for admission to the degree of Doctor of Philosophy. It contains an account of my own work performed at the Department of Physics of the University of Warwick, in the period December 1983 to April 1987, under the supervision of Dr. H. Mykura. No part of it has been used previously in a degree thesis submitted to this or any other University. The work described in this thesis is the result of my own independent research except where acknowledged in the text.

Ramli Omar

April 1987

CONTENTS

|   |      |
|---|------|
| List of Illustrations                             | viii |
| List of Tables                                    | xvi  |
|   | Page |
| <u>CHAPTER 1: INTRODUCTION</u>                    | 1    |
| <u>CHAPTER 2: GRAIN BOUNDARY STUDIES</u>          | 4    |
| 2.1 Importance of grain boundary energy studies   | 4    |
| 2.2 Grain boundary structure                      | 6    |
| 2.2.1 General geometrical aspects                 | 6    |
| 2.2.2 Models                                      | 8    |
| 2.2.3 Special and general grain boundaries        | 16   |
| 2.3 Shewmon and Herring torque terms              | 18   |
| 2.4 Bamboo structure                              | 22   |
| 2.5 Anisotropies of the grain boundary energy     | 23   |
| 2.5.1 Variation with disorientation, $\theta$     | 23   |
| 2.5.2 Variation with inclination, $\phi$          | 25   |
| 2.5.3 Variation with impurity                     | 28   |
| 2.5.4 Variation with temperature                  | 28   |
| <u>CHAPTER 3: THEORETICAL BACKGROUND</u>          | 30   |
| 3.1 Methods of grain boundary energy measurements | 30   |
| 3.1.1 Relative energies                           | 30   |
| 3.1.1.1 Grain boundary grooving                   | 31   |
| 3.1.1.2 Twin boundary grooving                    | 35   |
| 3.1.2 Absolute energies                           | 37   |

|   |    |
|---|----|
| 3.2 Grain boundary faceting   | 38 |
| 3.3 Grain boundary morphology in sheet  | 45 |
| <u>CHAPTER 4: DISORIENTATION DETERMINATIONS</u>   | 48 |
| 4.1 General theory and applications of selected<br>area electron channelling patterns<br>(s.a.c.p.'s) | 48 |
| 4.2 Experimental technique for obtaining<br>s.a.c.p.'s in the scanning electron micro-<br>scope (SEM) | 54 |
| 4.2.1 Specimens preparation   | 54 |
| 4.2.2 Setting-up procedures   | 54 |
| 4.3 Orientation determinations using s.a.c.p.'s   | 58 |
| 4.3.1 The stereographic projection  | 58 |
| 4.3.2 The generation and indexing of the<br>unit triangle map   | 60 |
| 4.3.3 Relative rotation between s.a.c.p.<br>and normal micrographs                                    | 63 |
| 4.3.4 Complete orientation determinations   | 66 |
| 4.4 Disorientation across a boundary  | 68 |
| 4.4.1 Rotation matrix   | 68 |
| 4.5 Accuracy of disorientation determination  | 71 |
| <u>CHAPTER 5: MEASUREMENTS ON GRAIN BOUNDARIES IN "BAMBOO<br/>STRUCTURE" COPPER WIRES</u>             | 73 |
| 5.1 Experimental arrangements   | 73 |

|  |  |    |
|--|--|----|
| 5.1.1  | Preparation of specimens   | 73 |
| 5.1.2  | Microscopy   | 74 |
| 5.1.3  | Tilt angle $\phi$ of boundary plane<br>determinations                | 75 |
| 5.1.4  | Boundary type determinations   | 76 |
| 5.2  | Results and discussion   | 77 |
| 5.2.1  | Orientations and Herring torques<br>measured                         | 77 |
| 5.2.1.1  | Detailed analysis of $\Sigma 11$<br>boundaries                       | 82 |
| 5.2.2  | 'Kinking' in wires   | 83 |
| 5.2.3  | Grain boundary sliding   | 85 |
| <u>CHAPTER 6: MEASUREMENTS ON SPECIAL BOUNDARIES IN COPPER</u> |  |    |
|  | <u>SHEETS</u>  | 86 |
| 6.1  | Experimental arrangements  | 86 |
| 6.1.1  | Specimen preparation   | 86 |
| 6.1.2  | Microscopy   | 87 |
| 6.1.3  | Tilt angle $\phi$ of boundary plane<br>determinations                | 87 |
| 6.2  | Condition for a boundary (like B in<br>Figure 6.1(a)) not to migrate | 88 |
| 6.3  | $\Sigma 3$ boundaries  | 90 |
| 6.3.1  | Results and discussion   | 90 |
| 6.3.1.1  | $\gamma$ -plot and $\Gamma$ -plot                                    | 93 |



-vii-

|  |     |
|--|-----|
| 6.4 $\mathcal{L}_9$ boundaries               | 95  |
| 6.4.1 Results and discussion                 | 96  |
| <u>CHAPTER 7: <u>GENERAL CONCLUSIONS</u></u> | 100 |
| <u>REFERENCES</u>                            | 105 |

LIST OF ILLUSTRATIONS

| <u>Figure</u> |   | <u>Following page</u> |
|---------------|---|-----------------------|
| 2.1           | Formation of a $\sqrt{2}$ coincidence site lattice (CSL) for a rotation of $36.9^\circ$ about [001] for a simple cubic structure.   | 11                    |
| 2.2           | Formation of DSC-lattice in the same structure of Figure 2.1.   | 13                    |
| 2.3           | Equilibrium configuration of intersection of three general interfaces.  | 21                    |
| 2.4           | SEM micrograph showing a "bamboo structure" in a copper wire annealed at $1000^\circ\text{C}$ .   | 22                    |
| 2.5           | Variation of grain boundary energy with disorientation for low-angle [001] tilt boundaries in copper.   | 24                    |
| 3.1           | Equilibrium configuration at the intersection of grain boundary with surface showing equivalent forces.   | 33                    |
| 3.2           | Equilibrium configuration at intersection of pair of twin boundaries with surface showing equivalent forces.  | 36                    |
| 3.3           | Section of a faceted grain boundary, showing the various angles defining the facet crystallography.   | 41                    |
| 4.1           | (a) Changes in the geometry of an incident beam during scanning over a flat crystal surface.<br>(b) Shows the variation of backscattering signal intensity as a function of scan angle $\theta$ . | 49                    |

| <u>Figure</u>  | <u>Following page</u> |
|--|-----------------------|
| 4.2 A typical selected area electron channelling pattern (s.a.c.p.) of copper at 30kV showing crystallographic features of the pattern.                                | 50                    |
| 4.3 Line diagram showing electron optical ray paths in lower portion of SEM:<br>(a) normal mode and (b)-(d) s.a.c.p. mode.   | 50                    |
| 4.4 A typical polycrystalline copper specimen with a small twin in the centre of field of view:<br>(a) normal and (b)-(d) "through-focus series" in the s.a.c.p. mode. | 51                    |
| 4.5 Setting-up procedures for obtaining s.a.c.p. in the Cambridge Stereoscan 250 MKJ.  | 56                    |
| 4.6 Unit triangle map of copper at 20kV in back-scattered mode.  | 62                    |
| 4.7 Unit triangle map of copper at 40kV in backscattered mode.   | 62                    |
| 4.8 Indexing guide for the f.c.c. system showing the major bands and poles.  | 62                    |
| 4.9 Rotation of s.a.c.p. at 40kV for different "Working distance" settings.  | 65                    |
| 4.10 Relative rotation between s.a.c.p. and ordinary micrographs as a function of working distance at 30kV.  | 65                    |
| 4.11 Relative rotation between s.a.c.p. and ordinary micrograph as a function of final lens current at 30kV.   | 65                    |

| <u>Figure</u>  | <u>Following page</u> |
|--|-----------------------|
| 4.12 Relative rotation between s.a.c.p. and ordinary micrographs as a function of accelerating voltage for a given working distance.   | 66                    |
| 4.13 A typical example of a "complete" orientation determination using s.a.c.p. from copper specimen.  | 67                    |
| 4.14 The stereographic projection resulting from the s.a.c.p. shown in Figure 4.13.  | 68                    |
| 4.15 Graphical measurements in the stereographic projection of the direction cosines $A_{ij}$ between the $\langle 100 \rangle$ directions of one crystal and the $\langle 100 \rangle$ directions of the other crystal. | 70                    |
| 4.16 Graphical construction in the stereographic projection of the axis about which a single rotation of an angle $\Theta_R$ will cause coincidence of one crystal with the other.                                       | 71                    |
| 5.1 Experimental set-up used for (a) horizontal and (b) hanging wires preparation.   | 73                    |
| 5.2 A typical SEM micrograph in backscattered mode of a grain boundary groove in copper annealed at $1000^\circ\text{C}$ .   | 74                    |
| 5.3 A schematic diagram of "bamboo structure" wire defining the tilt angle $\phi$ , the area of  |                       |

Figure

Following page

|   |    |
|---|----|
| the horizontal plane A and the area of the tilt plane $A_g = A/\cos\phi$ .  | 75 |
| 5.4 Normalized torque term determinations for grain boundaries in wire specimens.   | 76 |
| 5.5 Graphical construction in the stereographic projection for the determination of the boundary type.  | 76 |
| 5.6 Distribution of normalized torque terms measured in (a) horizontal and (b) hanging copper wires annealed at 1000°C.                                   | 79 |
| 5.7 The highest measured torque term in a hanging copper wire annealed at 1000°C.   | 79 |
| 5.8 Distribution of the ratio of grain boundary energy to surface energy measured from (a) horizontal and (b) hanging wires of copper annealed at 1000°C. | 80 |
| 5.9 A typical grain boundary in a bamboo structure copper wire with the orientation shown to be $\Sigma_{11}$ .   | 82 |
| 5.10 Torque terms $\frac{1}{\gamma_s} \left( \frac{\gamma_{gb}}{\gamma_s} \right)$ for $\Sigma_{11}$ boundaries in copper near {311} mirror plane.        | 82 |
| 5.11 Grain boundary energy anisotropy for $\Sigma_{11}$ boundaries centred on (a){311} and (b){332} mirror planes.  | 83 |
| 5.12 A {110} section through the $\gamma$ -plot for the $\Sigma_{11}$ boundary.   | 83 |

| <u>Figure</u>   | <u>Following page</u> |
|---|-----------------------|
| 5.13 (a) SEM micrograph of copper wire showing "kinking" at grain boundaries. (b) The terms used to define the Shevmon mechanism and gravitational torques.   | 84                    |
| 5.14 SEM micrograph of copper wire showing an "upward" sliding.   | 85                    |
| 6.1 (a) SEM micrograph of a polycrystalline copper sheet annealed at 1000°C showing some twin boundaries. (b) A schematic section of the sheet defining the terms used for the determination of boundary inclination. | 88                    |
| 6.2 (a) and (b) SEM micrographs of front and back surfaces of a copper sheet specimen annealed at 1000°C. (c) the trace of one of the $\Sigma_3$ twin systems.  | 90                    |
| 6.3 (a) SEM micrograph of one of the $\Sigma_3$ twin boundaries appearing in Figure 6.2 and the corresponding s.a.c.p.'s. (b) The orientation of the $\Sigma_3$ twin boundary shown in (a).                           | 90                    |
| 6.4 The orientation of the incoherent $\Sigma_3$ twin boundaries if they were perpendicular to the specimen surface and coherent $\Sigma_3$ {111} planes.   | 90                    |
| 6.5 Distribution of the incoherent $\Sigma_3$ twin boundaries if they were perpendicular to the specimen surface and coherent $\Sigma_3$ {111} planes.  | 90                    |

| <u>Figure</u>   | <u>Following page</u> |
|---|-----------------------|
| 6.6 The orientations of the incoherent $\Sigma_3$ twin boundaries measured from copper sheets annealed at 1000°C.   | 91                    |
| 6.7 Plot of $\frac{1}{\gamma_e} \left( \frac{\gamma_e}{\gamma_\phi} \right)$ against the angle from $\langle 110 \rangle$ zone for the incoherent $\Sigma_3$ twin boundaries.   | 92                    |
| 6.8 Optical micrograph of a typical pair of coherent $\Sigma_3$ twin boundary in copper and the corresponding interferogram.  | 94                    |
| 6.9 Optical micrograph of a typical incoherent $\Sigma_3$ twin boundary in copper and the corresponding interferogram.  | 94                    |
| 6.10 (a) $(0\bar{1}1)$ and (b) $(111)$ sections through the $\Gamma$ -plot and the Wulff shape for the $\Sigma_3$ twin boundaries.  | 95                    |
| 6.11 (a) $(110)$ section through the $\Sigma_9$ $\Gamma$ -plot obtained by adding together two $\Sigma_3$ $\Gamma$ -plots in the proper direction. (b) $(\bar{1}14)$ section through the $\Sigma_9$ $\Gamma$ -plot obtained by adding together two $\Sigma_3$ $\Gamma$ -plots in the $[110]$ and $[221]$ directions and then drawing an elliptical $\Sigma_3 + \Sigma_3$ $\Gamma$ -plot through them. | 95                    |
| 6.12 SEM micrographs showing the anchored $\Sigma_3$ boundaries, (a) at one end and (b) at both ends, formed by the intersection of coherent $\{111\}$ planes.  | 96                    |

Figure

Following page

- |      |   |    |
|------|---|----|
| 6.13 | SEM micrograph showing a curved $\Sigma 9$ boundary.  | 96 |
| 6.14 | (a) and (b) SEM micrographs showing the same macroscopically flat $\Sigma 9$ boundary on both sides of the specimen surface. (c) The trace of the boundaries. (d) The orientation of the $\Sigma 9$ $(114)_1/(114)_2$ boundary appearing in (a) and (b).  | 96 |
| 6.15 | (a) SEM micrograph showing facets of $\Sigma 9$ boundary. (b) SEM micrograph on the other side of (a) showing the break up and non break-up of the $\Sigma 9$ boundary. (c) The trace of the boundaries. (d) The orientation of the $\Sigma 9$ $(771)_1/(557)_2$ boundary appearing in (a) and (b). | 97 |
| 6.16 | Vertical sections PP and QQ through $\Sigma 9$ specimen shown in Figure 6.15(c).  | 97 |
| 6.17 | SEM micrograph showing typical triangular $\Sigma 3$ twins at the $\Sigma 9$ boundary in copper annealed at 1000°C.   | 97 |
| 6.18 | Optical micrograph of a typical $\Sigma 9$ boundary in copper annealed at 1000°C and the corresponding interferogram.   | 98 |
| 6.19 | (110) section through the $\Sigma 9$ $\chi$ -plot.  | 99 |



Figure

Following page

6.20 (a) and (b) SEM micrographs of <sup>the</sup> front and back surfaces of <sup>a</sup> copper sheet showing a complex curvature of the  $\xi_9$  boundary. (c) The trace of the boundaries. (d) The orientation of the curved  $\xi_9$  boundary appearing in (a) and (b).

LIST OF TABLES

| <u>Table</u> |  | <u>Following page</u> |
|--------------|--|-----------------------|
| 1            | Details of 10 typical boundaries<br>measured in copper wires                           | 79                    |
| 2            | Details of E11 boundaries  | 79                    |
| 3            | Details of E25b boundaries   | 79                    |
| 4            | Details of 8 typical incoherent E3<br>boundaries measured in copper sheet<br>specimens | 90                    |
| 5            | Typical sets of parallel planes on a<br>common <110> zone in E3                        | 93                    |

## CHAPTER 1: INTRODUCTION

Most practical applications of solid materials involve polycrystalline aggregates, rather than large single crystals. Such an aggregate is made up by a number of generally randomly oriented single crystals, more usually referred to as grains, and the junction between these grains is known as a grain boundary. In a pure metal the differences between adjacent grains are differences in crystallographic orientation. In more typical materials of technological importance there may also be differences in composition between adjacent grains or between grains and boundary regions, or variations in lattice dimensions from one grain to another, or in combination of all of these properties. A grain boundary is thus a region of disorder in the crystal structure. This disorder gives rise to various properties which may be either beneficial or deleterious in some metallurgical processes. Consequently it is important to study the exact nature of these interfaces.

A grain boundary may be described in several ways (e.g. Gifkins 1969). The choice of an appropriate description is usually governed by the property or problem being focused and discussed. A grain boundary may be considered as a defect in the crystal structure or as a mismatch in the crystal lattice. Its structure and properties can then be described in terms of arrays of dislocations, in terms of areas of good and bad fit in the structure, or in terms of coincidence relationships between the neighbouring crystal lattices. Alternatively it can be treated as an amorphous region and its behaviour and properties studied without specifying the detail of the

atomic structure.

A grain boundary, as a disordered region, can be regarded as having associated with it a definite amount of free energy per unit area, namely, the grain boundary energy. The magnitude of this energy will obviously depend on several factors such as crystal disorientation, boundary inclination, temperature and impurity levels. The variation with impurity levels may well be brought about by segregation of solute atoms to the boundary. Measurements of absolute grain boundary energies are rather difficult, as very sensitive techniques are required (e.g. Mondros 1969). Instead, such energies are usually measured relative to some reference surface or grain boundary. Such measurements are often used in preference to direct structural studies to yield information about the properties and behaviour of grain boundaries and, in fact, also provide a useful indirect way of studying the structure of boundaries.

Most experimental measurements of grain boundary energies are based on a local equilibrium configuration of some system of intersecting interfaces. Such a configuration can be achieved after specimens are annealed at high temperatures for sufficiently long periods. Extensive studies on the variation of grain boundary energy with crystal disorientation have been made (e.g. Gleiter and Chalmers 1972). This variation leads to the Shewmon torque terms acting on the crystals, and causes a change in disorientation (Shewmon 1966). Much less work has been done on the variation of grain boundary energy with boundary inclination, under a condition of fixed crystal disorientation. This variation can conveniently be represented by a

' $\gamma$ -plot', exactly like the surface energy of a crystal. The dependence on this factor leads to the Herring torque term, which describes the couple acting on the boundary plane and tends to rotate it towards position of lower energy (Herring 1951). As a result of this dependence, in extreme cases, faceting of the grain boundary can occur. In faceting, the grain boundary breaks up into segments of different orientation, whose total energy is less, even though the total area is greater. Also, a boundary can break up into two boundaries whose total disorientation equals that of the initial boundary, with a new crystal appearing. Again the total energy of the two boundaries must be less than that of the original boundary.

It is the objective of this dissertation to report observations on the effect of boundary inclination on <sup>the</sup> energy of grain boundaries in copper. In particular, the  $\gamma$ -plot of  $\Sigma 3$  boundaries (usually referred to as the first order twin boundaries) was studied. The break up of  $\Sigma 9$  boundaries (second order twin boundaries) into two  $\Sigma 3$  boundaries and the relation between the  $\Sigma 3$  and  $\Sigma 9$   $\gamma$ -plots was investigated, using sheet specimens. The Shewmon and Herring torque terms were investigated using 'bamboo' structure wire specimens. The  $\Sigma 11$   $\gamma$ -plot was evaluated.

The disorientation across a boundary was expressed in terms of the rotation matrix. This was obtained from the orientations of the two crystals plotted on a stereographic chart. The orientations were obtained using selected area electron channelling patterns (s.a.e.c.p's) observed in the scanning electron microscope (SEM).

## CHAPTER 2: GRAIN BOUNDARY STUDIES

### 2.1 Importance of grain boundary energy studies

The presence of grain boundaries in polycrystalline materials has a marked effect on a variety of properties (Gleiter and Chalmers 1972). During heat treatment they can both initiate and block phase transformations, migrate to give recrystallization, act as accelerated diffusion paths, and influence the distribution of pores, solute and precipitates. Generally speaking, grain boundaries play an important role in the development of microstructure. Under service conditions the grain boundaries continue to play a significant part. At elevated temperatures they can act as sources and sinks for point defects and dislocations, and can also slide, thereby helping to initiate failure by the nucleation and growth of cavities. These effects are of extreme importance in a wide range of materials used under creep conditions in, for example, nuclear reactors, power generating plant and turbine blading. Grain boundary embrittlement by solute segregation and/or precipitation at grain boundaries during heat treatment can also lead to premature failure at ambient temperatures by intergranular fracture or stress corrosion cracking. Certain low-alloy steels for steam power plant components and aluminium alloys for airframes are particularly vulnerable examples. Against this, however, the ability of grain boundaries to act as barriers to plastic flow and crack growth still makes them an indispensable feature of the microstructure of engineering materials requiring both strength and toughness. Grain refinement remains the simplest microstructural process that the metallurgist can employ which will increase the

strength whilst also increasing the toughness.

In recent years, there has been extensive interest in many of the grain boundary dependent processes mentioned above. They have been increasingly studied in both metallic and non-metallic materials. Concurrent with this, there has been a significant development in theoretical and experimental techniques towards a better understanding of the detailed atomic structure of grain boundaries and of the defects which may exist in them. More recently, the direct observation of the atomic structure of grain boundaries has become feasible owing to the increased point-to-point resolution of modern microscopes such as the high-resolution transmission electron microscope (HRTEM), and also with the help of the powerful computer image simulation (Robinson 1986). Applications of such an improved technique have established that not only do the images strikingly illustrate structural features of grain boundaries, but they can also yield quantitative information on atomic positions. However, pursuing this atomic approach is both experimentally and theoretically complex since it works well only for special, simple types of boundaries. Consequently, this approach is of little use in studying randomly occurring boundaries in a wide range of materials, which is generally the situation of interest.

Since such direct techniques are limited to certain types of specimens, it is, in general, necessary to proceed by indirect methods in order to obtain information about the structure of a boundary. These consist, of necessity, of the observation or measurement of a property of a boundary and the comparison of the results with the prediction

resulting from theories of the structure of grain boundaries. One of the few properties which is commonly measured is the energy of a grain boundary. As mentioned in the introduction, this quantity depends on several parameters and this dependence is obviously very complex. Consequently, the majority of investigations into grain boundary energy are made by studying the dependence on only one parameter while keeping the others fixed. This means that attention is focused on more restricted systems. In the simplest case, for example, the orientation difference is given by a single angle of tilt and the boundary plane is made the symmetry plane, so that the boundary can be defined by a single parameter. Otherwise, the measurements only give an energy of average grain boundaries, involving a number of rather ad-hoc assumptions and simplifications. Again, the extension of these restricted situations to the general boundary is rather difficult since it seems likely that the properties of grain boundaries in specially prepared simple bicrystals may be quite different from those of a typical grain boundary in a polycrystalline aggregate. This latter type of grain boundary is usually the common form found in every day situations.

## 2.2 Grain Boundary Structure

### 2.2.1 General geometrical aspects

Since the grains in a single phase polycrystalline specimen are generally in many different orientations, thus many different types of grain boundary are therefore possible. Various techniques have been used to determine the orientation of the crystal and several



descriptions have been employed to describe the orientation relationships between the two adjoining crystals. One of the most useful techniques which can be used for the determination of the crystal orientation is by using the s.a.c.p. observed in the SEM. The orientation relationships between the adjacent crystals can be described in terms of the rotation matrix. Both, the technique and the description, have indeed been used in this work as will be discussed fully in chapter 4.

In general, five degrees of freedom are needed to describe the orientation relationships between the two grains abutting at a grain boundary (e.g. Christian 1975). Two of these are used to define the axis of disorientation, one to define the angle of disorientation and a further two degrees of freedom to define the orientation of the boundary plane with respect to one set of crystal axes. The rotation matrix (and consequently the angle-axis pair) constitutes a unique description of a boundary in the triclinic system. In the other crystal classes, there are a multiplicity of choices of the angle-axis pair, arising from the symmetry within the class. For boundaries between cubic crystals there are 24 equivalent descriptions, the choice of the most meaningful usually being governed by minimum angle of disorientation.

While the axis of rotation will not generally be simply oriented with respect to either grain or the grain boundary planes, there are two special types of boundary that are relatively simple. These are pure tilt and pure twist boundaries. A pure tilt boundary occurs when the axis of rotation is parallel to the plane of the boundary, whereas

a pure twist boundary is formed when the rotation axis is perpendicular to the boundary plane. One can visualize these boundaries easily with a simple cubic lattice.

It is sometimes suggested (e.g. Christian 1975) that in addition to the above five parameters, three further degrees of freedom are required to specify the components of any relative translation of the atoms of one crystal relative to the atom sites of the other. A ninth degree of freedom may be necessary to specify the position of the boundary itself. However, of these nine degrees of freedom, only the first five can in principle be imposed geometrically on an experimental sample and the other four are restricted by the existence of the structure of relaxed grain boundaries.

#### 2.2.2 Models

Many of the early theories on grain boundary structure are covered in the book by McLean (1957) and more recent ones have been critically reviewed <sup>in</sup> numerous articles, for example, by Gleiter (1982), Sutton (1984) and Fischmeister (1985). Thus only a brief discussion of these theories will be presented here.

The description of grain boundaries in terms of arrays of dislocations which was developed by Frank (1950) and Read and Shockley (1950) is still generally accepted as a satisfactory model for low angle boundaries. The arrays of edge dislocations which accommodate tilt components and the arrays of screw dislocations which accommodate twist components have both been observed many times in many materials.

The extension of the dislocation model to high angle boundaries

is rather difficult. As the angle of disorientation between the grains increases, the separation between the dislocations get smaller. This eventually leads to the overlap of the dislocation cores when the disorientation exceeds  $\sim 10^{\circ}$ - $15^{\circ}$  and results in the loss of identity of individual defects. Above this angular disorientation the high angle grain boundary regime is entered and the dislocation model is no longer sufficient.

Various models, which tend to ignore geometry either partially or completely, were proposed to explain high angle grain boundary structure (McLean 1957). These models were mainly concerned with explaining or formulating the behaviour of a boundary sensitive property or group of properties. One such model envisaged the grain boundary region as a layer of supercooled liquid. This liquid layer approach however does not find much support for metallic materials, but it may well be relevant to polycrystalline ceramics.

The starting point for all the recent models of grain boundary structure in metals and alloys is the transition lattice model due to Bargreaves and Hill (e.g. McLean 1957). Here the boundary region is thought to be comprised of atoms occupying sites which are transitional between those required to define the grains on each side of the boundary. Over the years, various estimates for the actual thickness of this transition region were put forward but then it has proved possible to directly image the boundary region using field ion microscopy (FIM) which shows that this region is very narrow (Brandon et al. 1964).

A large number of developments of the transition lattice model

were made (e.g. McLean 1957). Again, the models that arose out of these developments tend to concentrate on explanations of boundary dependent properties and ignore, at least partially, geometrical considerations. The best known models of this type of approach, in the current context, is that they recognise a variation in boundary structure over the boundary plane and this aspect is common to most of the recent models.

However, the models discussed thus far have taken very little consequence of the geometry either across the boundary or of the boundary region itself. In turn the models so far considered treat all high angle boundaries as similar, whereas experimental observations suggest that certain boundary geometries are associated with special behaviour. Consequently, grain boundaries are usually divided into two broad classes, namely, special boundaries and general boundaries, as will be discussed in the next section. The geometrical models predicting the existence of special boundaries were developed a long time ago. The first of these was the coincidence site lattices model (CSLs). The historical development of this model is covered in the paper by Grimmer et al. (1974).

The CSL model is of importance because it determines the periodicity of the atomic structure of the grain boundary. A three-dimensional CSL is formed when two interpenetrating crystal lattices, with the same lattice parameter, which have one lattice point in common, are related by any of a series of special rotations through the common points to yield more coincidence sites. The reciprocal density of coincidence sites relative to crystal lattice sites is

denoted by  $\Sigma$ , where  $\Sigma$  is an odd integer. The highest possible degree of coincidence in the cubic system, apart from a perfect crystal, is for a first order twin for which is  $\Sigma 3$ . A number of different mathematical notations are available for describing rotations (Lange 1967). The angle-axis pair relationships for the CSL are relatively easily generated. A simple example in two-dimensions of  $\Sigma 5$  for a simple cubic lattice generated by a rotation of  $36.9^\circ$  about  $[001]$  is shown in Fig. (2.1). It can be seen that a CSL is generated which has a cell five times bigger than the primitive cell. The primitive unit cell of the CSL has, by definition, a volume of  $\Sigma$  times that of the primitive unit cell of the crystal. Early on it was recognised that boundaries having a high density coincidence site lattice orientation (i.e. a low value of  $\Sigma$ ) were associated with special properties (e.g. Aust and Rutter 1956).

It was recognised that some 'spread' in the angle-axis pair relationship might be accommodated, in the real case, by invoking networks of coincidence site lattice dislocations (Brandon et al., 1964). Further, the orientation of the boundary plane with respect to the coincidence site lattice was expected to be important (Brandon et al. 1964). It was suggested that the boundary would attempt to follow a densely packed plane in the coincidence site lattice. A further consequence of this approach is the suggestion that, if a boundary is constrained to lie at an angle to a close-packed plane in the coincidence site lattice, it will therefore tend to take up a stepped structure such that it has a maximum area in the densely packed planes of the coincidence site lattice.

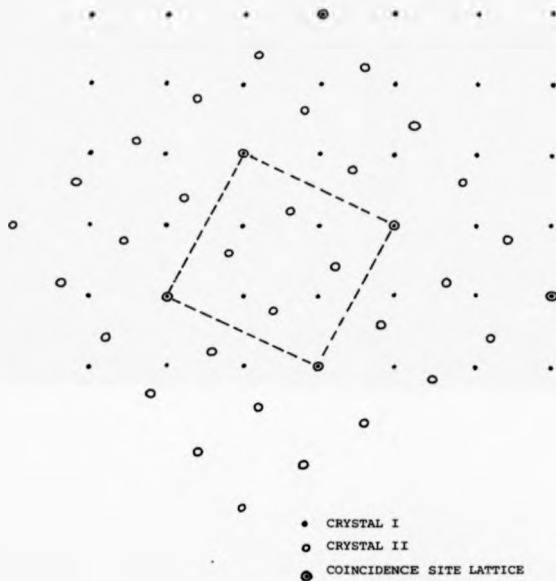


figure 2.1 Formation of a  $\Sigma 5$  coincidence site lattice for a rotation of  $36.9^\circ$  about  $[001]$  for a simple cubic structure. The unit cell of the coincidence site lattice is shown by broken lines.

A development of the CSL model was made by Bishop and Chalmers (1968) who envisaged a regular repeating pattern of ledges arising from deviations from perfect coincidence. This model, the coincidence ledge/dislocation model, sees deviations from coincidence primarily in terms of ledges. In practice after relaxation the repeating structural unit from either starting point becomes identical. This structural unit model (e.g. Gleiter 1971) again stresses the periodicity of fit-misfit across the boundary plane.

Bollmann (1970) introduced a concept known as the O-lattice. He proposed that regions of good atomic fit in a boundary should not be identified solely by coincidence of points of the two crystal lattices, but also by coincidences of interior cell points. The point is considered to be a coincidence if for any cell of one crystal lattice the interior coordinates of a point (expressed as a fraction of the cell edges) are identical with the interior coordinates of that same point measured relative to a cell of the other crystal lattice. Thus a CSL is simply a sublattice of the O-lattice. It turns out that there is a large number of O-lattices for a given relative orientation of the two lattices, since there are many transformations which can be used to transform one crystal lattice to the other. For a given O-lattice, each O-lattice point may be used as an origin for the transformation linking the two crystal lattices; the O-lattice is therefore a "lattice of origin". The O-lattice spacing is a continuous function of the transformation and this spacing therefore varies continuously with crystal disorientation, in contrast to the discontinuous behaviour of the CSL. The physical significance of this

approach is best seen in the light of the low angle boundary case.

A boundary with a disorientation that differs slightly from that of a coincidence relationship relaxes to the structure of the coincidence boundary with a superimposed network of the secondary grain boundary dislocations (GBDs). The formal theory for such GBDs has been given by Bollmann (1970). The function of the secondary GBD is to localize the deviation from the coincidence boundary reference structure. Their role is therefore analogous to that of discrete primary dislocations preserving the ideal crystal lattice in a low angle boundary. However, the Burgers vectors of secondary GBDs are not crystal lattice vectors, but vectors of the appropriate displacement shift complete (DSC) lattice. The DSC lattice for a particular boundary defines all the vector displacements of one crystal lattice respect with the second which are possible under the condition that the overall pattern of the boundary structure produced by the two interpenetrating lattices remains unchanged. The simplest way to see the geometrical basis of the DSC lattice is to refer to the interpenetrating crystal lattices in which a CSL exists as shown in Fig. (2.2). The base vectors of the DSC lattice are shown at the centre of the diagram. An important property of the DSC lattice is that the lattice spacing in the plane perpendicular to the axis of disorientation tends to vary reciprocally with the spacing of the CSL. This means that as the degree of lattice coincidence matching decrease, the CSL tends to become large and the DSC lattice tends to become smaller.

Secondary GBDs may be employed to form networks referred to as



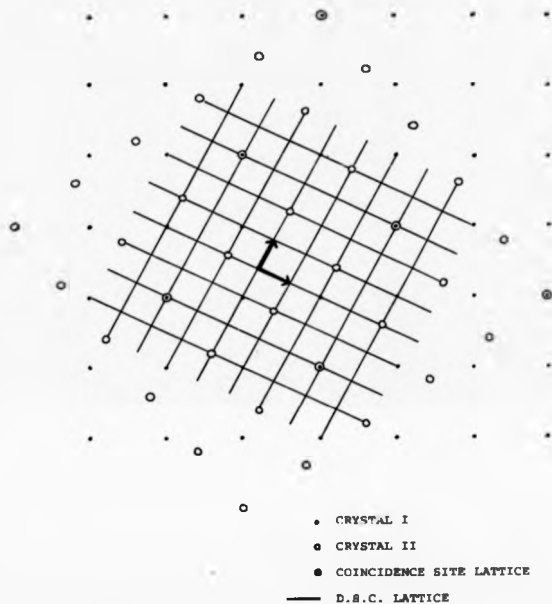


Figure 2.2 Formation of DSC-lattice in the same structure of Figure 2.1. The base vectors of the DSC-lattice are shown at the centre of the diagram.

secondary G-lattice or  $O_2$ -lattice (Bollmann 1970, Smith and Pond 1976). The  $O_2$ -lattice formulation requires that the secondary DSC Burgers vectors for  $\hat{L}_1$  (a single crystal) are identical to the primary lattice Burgers vectors and it requires that all primary vectors are included as possible DSC vectors. However, for a given rotation between two crystal lattices the  $O_2$ -lattice will depend upon the CSL chosen as a basis.

A plane matching (PM) model has been introduced by Pumphrey (1972). This model proposes that a high angle grain boundary across which a single set of low index planes is continuous is one of low energy. This could occur in any crystal system provided that the planes were sufficiently densely packed, for example, in fcc crystals the planes are {200}, {220} and {111}. The model does not attach any particular importance to the boundary plane.

The difference between CSL and PM models is that while CSL requires that only those boundaries at specific disorientation are of low energy, the PM model requires that all boundaries created by rotations about a low index axis are of relatively low energy. Thus a PM boundary may be regarded formally as the limiting case of a CSL boundary when  $\hat{L}_1$  approaches infinity (Warrington and Grimmer 1974). When a set of relatively low index planes is slightly mismatched across a boundary, relaxation occurs in such a way as to produce local alignment of the planes as far as is possible in the region of the interface. Such an array would be analogous to the arrays of dislocations which accommodate small angular deviation from coincidence disorientations described above. However, in this case,

it is the alignment of planes which is conserved rather than a pattern of two-dimensional atomic matching in the interface. Far from high density coincidence orientations, their Burgers vectors will presumably be equal to the interplanar spacing measured in the boundary plane. Thus the PM description is actually not an independent model but is merely another way of representing the line structures of certain boundaries which are already well accounted for by the more general GBD model.

In recent years, the atomic structure of grain boundaries has been studied extensively using computer simulation. Much of this work has been reviewed recently by Sutton (1984). In general, the procedure has been to find the total energy as a sum of the interaction energies between individual atoms. The interaction energies, in turn, are derived from a suitable interatomic potential function. The minimum energy configuration of the ensemble making up the boundary is then found by computer calculation. Despite the apparent simplicity of this technique, several difficulties are frequently encountered such as proper choice of the interatomic potential, problems with non-central forces, establishment of proper boundary conditions and finding relaxation techniques capable of determining the configuration of true minimum energy. Fortunately, from the standpoint of determining atomic structure, it appears that the results are not highly sensitive to the exact form of the interatomic potential. Most of the calculations have been static calculations, and therefore refer to the situation at 0°K where entropy effects do not contribute. Also, most of the calculations have been made for

relatively short-period boundaries, since relatively small computational cells could be used. Nevertheless, a number of interesting results have emerged. In general, the boundary regions are very narrow, and crystallinity is maintained almost up to the boundary plane in agreement with the direct observations (Brandon et al. 1964).

Recent studies of the occurrence of minimum energy boundaries in noble metals and noble metal alloys (e.g. Sauter et al. 1977, Erb et al. 1982) indicate that for a full description of the grain boundary structure and energy, the change of the electronic structure in the boundary should not be disregarded. Also, the effect of temperature, pressure, etc. on the boundary structure should not be neglected.

#### 2.2.3 Special and general grain boundaries

In general, the experimental properties of grain boundaries are in agreement with the <sup>expected</sup> transition from low angle to high angle behaviour. A high angle boundary however is not necessarily without order. In particular, certain groups of high angle boundaries will have special properties such as structure, energy, diffusion, migration, etc., which make them quite different from those of disordered boundaries. The former boundaries are usually called 'special' grain boundaries and the latter 'general' grain boundaries. Clear experimental evidence which proves the existence of special boundaries has been reviewed by Pumphrey (1976).

Special grain boundaries will occur when two adjoining grains have some particular (rational) geometrical relationship. The geo-

metrical models of grain boundaries discussed in Section (2.2.2) allow, to some extent, the correlations of specific properties to the existence of intrinsic GBDs which define a well ordered periodic intergranular area. According to the CSL model, special grain boundaries arise when the two grains are in a relative orientation leading to a coincidence site lattice (CSL orientation). It turned out that angular coordinates of the boundaries exhibiting special properties do coincide with the angular values for the CSL with low  $\Sigma$ . Conventionally, this is attributed to the fact that the grain boundary occurring in the CSL with low  $\Sigma$  demonstrates a periodic structure and lower energy as compared with general boundaries. However, since the CSL model depends upon the presence of coincident sites, the number of such sites will decrease with increasing values of  $\Sigma$ . Also, for boundaries, with higher  $\Sigma$  values, the disorientation angles become close to one another. Thus it is difficult to identify an appropriate CSL orientation. So an upper limit of  $\Sigma$  has to be set ( $\Sigma_{\max}$ ) in order to categorize between special and general boundaries. It is regarded as special when  $\Sigma < \Sigma_{\max}$ , while it is regarded as general when  $\Sigma > \Sigma_{\max}$ . There are experimental observations which indicate that special properties exist for values of  $\Sigma$  up to about 33 (Herrmann et al. 1976, Goodhew et al. 1978). However, the maximum value of  $\Sigma$  at which a CSL has physical meaning is not known.

The CSL theory would be of limited interest if the special structures occurred only at exact CSLs disorientations. In fact the properties of the special boundaries are partially maintained for small angle deviation from the exact CSLs disorientations. Several

methods for determination of the deviation from the exact CSL disorientation,  $\Delta\theta_d$ , have been demonstrated and several criteria of specialness (a significant upper limit of  $\Delta\theta_d$ ) have been proposed (Deschamps et al. 1987). However, the criteria of specialness must be used cautiously because the maximum value of the deviation from the exact CSL orientations which can be admitted is far from being well established and orientation dependences of grain boundary properties have a sharply non-monotonic character with extrema at the special angles. Also, the maximum deviation at which the dislocation cores have physical existence is not clear at present. Furthermore, the analogy with low angle boundaries, however, should be treated with caution, as some high angle boundaries may have relaxed structures other than dislocation networks.

### 2.3 Shewmon and Berring torque terms

The central thermodynamic quantity which characterizes interfaces in solids is the free energy, a reflection of inadequate atomic bonding in the relatively disordered atomic structure of the interface. This quantity depends on the crystallographic orientation of the interface, temperature and the presence of adsorbed species arriving from the matrix. In a wide variety of solid-state phenomena, for example, in the formation of equilibrium microstructures, this quantity often plays a critical role. For a single component system, this interfacial energy  $\gamma_i$  at a temperature  $T$  can be related to the interfacial energy at absolute zero,  $\gamma_0$ , by the usual form of thermodynamic relation

$$\gamma_i = \gamma_o - TS_i \quad (2.1)$$

where  $S_i$  is the interfacial entropy. This entropy term has been discussed by Ewing (1971) but remains the most difficult factor to quantify. There are very few measurements available of the variation of  $\gamma_i$  with temperature for any interface. In many cases, the entropy term is small and may be neglected. Therefore, it is <sup>only</sup> possible to evaluate  $\gamma_o$  by studying  $\gamma_i$ .

By neglecting the entropy term and impurity effects, the interfacial energy therefore depends only on the crystallographic orientation. One of the techniques which enable this effect to be studied is the sintering experiment due to Shewmon (1966). He has suggested that, in the case of two metal single crystal spheres that have been sintered together enough to form a boundary, the interfacial energy of the system will decrease when the torque terms act on the spheres to rotate them relative to one another so as to form a grain boundary whose energy is lower than that of the initial stages. In this geometry, all five degrees of freedom of the boundary will be changed by the movement of spheres so as to decrease the grain boundary energy. These torque terms are usually known as the Shewmon torque term.

A modification of the Shewmon's experiment has been made by Gleiter's group (e.g. Herrmann 1976). In this case a large number of small metal single crystal spheres are sintered onto a single crystal substrate. During the sintering, a neck of the metal grows at the area

of contact. This neck contains a grain boundary which occupies the narrowest part of the neck and lies in a plane close to the plane of the substrate. They have shown that most spheres do rotate into CSL orientations within experimentally reasonable sintering times.

Under a condition of fixed crystal disorientation the Shewmon torque terms cannot act, the grain boundary energy then depends only on boundary inclination. This dependence leads to other types of torque terms called the Herring torque terms as will be discussed below. The inclination dependence of grain boundary energy is conveniently represented geometrically in terms of a ' $\gamma$ -plot' exactly like in the case of surface energy.

Since the classic treatment of metallurgical microstructures by Smith (1948), the interfaces of grains or phases have been considered to possess an interfacial energy or an associated interfacial tension which acts in all direction in the plane of the interface, exerting a 'pull' upon the grain edges, and opposed to that of other interfaces along their mutual line of intersection. The equilibrium configurations that develop in a three-dimensional polycrystalline material can therefore be treated as a balancing of interfacial energy vectors in the plane of the interfaces, intersecting in a common point of reference.

Herring (1951) has treated the general case of intersecting interfaces which applies to solid-solid intersections in polycrystalline solids, and the intersection of internal interfaces with a free surface (solid-vapour interface). By considering the equilibrium condition at a triple junction of resolved interfacial



energy vectors, he proposed that these vectors can be expressed by an equation of the form

$$\sum_{i=1}^3 \left[ \gamma_i \underline{t}_i + \left( \frac{\partial \gamma_i}{\partial \Omega_i} \right) \Omega_i \right] = 0 \quad (2.2)$$

where  $\underline{t}_i$  denotes a unit vector in the  $i^{\text{th}}$  interface perpendicular to and directed away from the line of intersection;  $\Omega_i = \underline{l}_i \times \underline{t}_i$ , where  $\underline{l}_i$  is a unit vector along the line of intersection and;  $\gamma_i$  is the interfacial energy of the  $i^{\text{th}}$  interface. The associated forces of magnitude  $\left( \frac{\partial \gamma_i}{\partial \Omega_i} \right)$  then result using a right-handed convention in performing the cross-product. These forces are the Herring torque terms which may be considered as forces which act normal to the interfaces (Fig. 2.3) and tend to rotate them toward positions of lower energy. Mullins (1963) has shown that this equation is also applicable to any number of interfaces meeting in a common line. Under certain conditions the Herring torque terms can be neglected, then Equation (2.2) reduces to the form of the simple triangle of forces which was originally proposed by Smith (1948), that is

$$\frac{\gamma_1}{\sin \Omega_1} = \frac{\gamma_2}{\sin \Omega_2} = \frac{\gamma_3}{\sin \Omega_3} \quad (2.3)$$

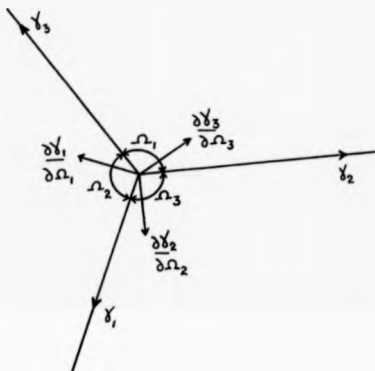


**Figure 2.3** Equilibrium configuration of intersection of three general interfaces.  $\Omega_i$  are the dihedral angles,  $\gamma_i$  are the interfacial energies and  $\frac{\partial \gamma_i}{\partial \Omega_i}$  are the Herring torque terms.

#### 2.4 Bamboo structure

In some cases wire samples are preferred to other geometrical types of samples because of the simpler stress system, and because the grain boundaries in fine wires are more easily described in the geometry of the system, with the result that the grain boundary energy contribution can be more accurately determined.

It is well established that one of the main difficulties in studying grain boundary properties is the fact that each boundary needs five degrees of freedom to describe it. However, to simplify the measurements, one can use a 'bamboo structure' wire (Fig. 2.4). In such a specimen the disorientation across a boundary is fixed for a given pair of crystals during the time in which local equilibrium is achieved. Thus the problem of describing the boundary reduces to that of two degrees of freedom.

A bamboo structure is formed when a fine wire is annealed at high temperatures. At such temperatures atomic movement in crystals is possible by diffusion. As a result of thermal activation, the atoms in the wire are fairly mobile and the grain boundaries migrate. Eventually, the wire takes the form of a series of large grains, extending across the diameter of the wire and as annealing time continues, the boundaries between these grains take up equilibrium configurations. The grain boundaries generally do not lie perpendicular to the wire axis after the annealing treatment, but rather are at apparently random angles to it. Such geometrical arrangement of the boundary planes in fact are due to the Herring torque terms which act on the boundary planes and try to rotate them

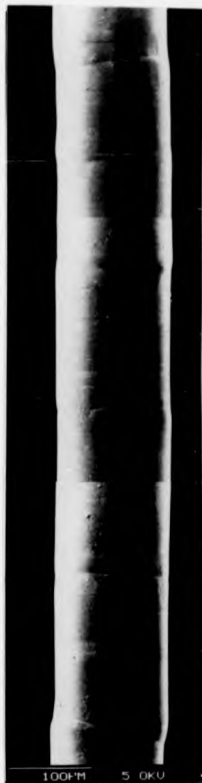


Figure 2.4 SEM micrograph showing a "bamboo structure" in a copper wire annealed at 1000°C in a dry 10% H<sub>2</sub>: 90% N<sub>2</sub> atmosphere.

toward minimum energy positions. Usually the average size of crystals in a bamboo structure wire is described by the average length of crystals and the diameter of the wire.

## 2.5 Anisotropies of the grain boundary energy

The experimental observations on grain boundary energies are mainly concerned with what is the effect of crystal orientation, boundary inclination, temperature and impurities on the energy of grain boundaries. Measurements of the boundary energy as a function of these parameters provide an important tool on the study of the grain boundary structure since the energy of a boundary is one of the most useful descriptions of boundary characteristics which can be measured relatively easily. Here the anisotropies of the grain boundary energy due to those parameters will be discussed. Several methods which have been used to measure the grain boundary energy will be discussed in the next chapter.

### 2.5.1 Variation with disorientation, $\theta$

The variation of a grain boundary energy with disorientation has been studied fairly extensively. This effect on grain boundary energy is described by the well-known treatment of Read and Shockley (1950) in which the energy expression is derived from the dislocation model of a grain boundary, that is

$$\gamma_b = \frac{Gb\theta}{4\pi k}(A - \ln \theta) = E_b \theta (A - \ln \theta) \quad (2.4)$$

where  $k = 0.5$  for the  $[001]$  twist boundary and  $(1 - \nu)$  for the tilt boundary,  $G$  is the shear modulus,  $\nu$  Poissons ratio,  $\theta$  the rotation angle,  $b$  is the modulus of the Burgers vector and  $A$  is a constant which depends on the core energy of an individual dislocation.

Early measurements of boundary energy as a function of  $\theta$  showed good agreement with the Equation (2.4), even for angles as large as  $40^\circ$  (Read 1953). This was somewhat surprising, because for high angle boundaries ( $\theta > 15^\circ$ ), the dislocation cores overlap to such an extent that the derivation of Equation (2.4) based on linear-elastic energy considerations ceases to be valid. It was subsequently found that Equation (2.4) does indeed give a good fit to the data for low-angle boundaries, and that the apparent fit for high angles is fortuitous since it is only obtained by changing the constant  $E_0$  and  $A$  from the values fitted at low angles. This is demonstrated by the data for tilt boundaries in copper in Fig. (2.5) (Gjostein and Rhines 1959). The theoretical curve fits the data very well up to about  $5^\circ$  or  $6^\circ$ . If van der Merwe's equation (van der Merwe 1952) is used, the experimental data can be described up to about  $9^\circ$ .

In general the  $\gamma_s - \theta$  relations will have several prominent cusps at certain disorientation angles which in fact correspond to the existence of boundaries of relatively good atomic fit. Two particular types of boundary which are characterized by a low energy have long been established. The ample evidence for the low energy of low-angle boundaries and coherent twin boundaries has been reviewed by Inman and Tipler (1963). Little is known, however, on the  $\gamma_s - \theta$  relations of high-angle boundaries which are not coherent twins. The shape of this

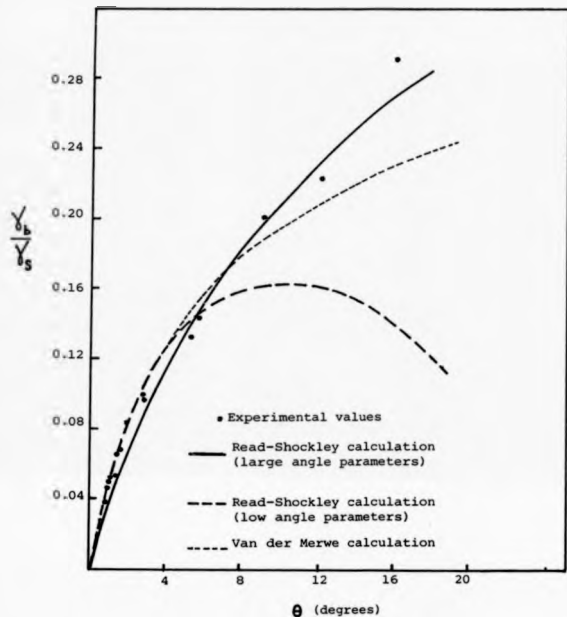


Figure 2.5

Variation of grain boundary energy with disorientation for low-angle [001] tilt boundaries in copper. Theoretical fits of the Read-Shockley equation using either high-angle or low-angle data shown (Gjostein and Rhines 1959).

plot is of basic interest as it provides information on the atomic structure of the boundaries. In fact, there are experimental observations which show that not all high angle boundaries have the same energy and these have been reviewed by Goodhew (1980). He concludes that boundaries of locally low energy can often be described in terms of CSL orientation relationships and small energy cusps exist around many CSL orientations even with high values of  $\Sigma$ ; also, there may still be low energy boundaries at disorientations not readily described by a CSL. The failure to reveal energy cusps in some of the earlier studies may have been due to several reasons and has been summarized by several authors (Gleiter and Chalmers 1972, Pumphrey 1976 and Shewmon 1966).

#### 2.5.2 Variation with inclination, $\phi$

There is little experimental information on the directional dependence of grain boundary energy. As discussed earlier, Herring's complete analysis of equilibrium at three planar interfaces intersecting in a line demonstrates the existence of torques which tend to rotate the grain boundaries into orientations of lower energy. Although this effect is usually neglected in grain boundary studies, there are observations which suggest that grain boundary torques are as large as those measured for free surfaces.

The cusps discussed in the preceding section were related to the curves showing the grain boundary energy versus the disorientation relationship. Equally, a plot of the boundary energy versus the inclination describes the energy per unit area of a boundary plane



between two crystals of fixed disorientation when the boundary changes its inclination between these crystals driven by the Herring torque terms. For a specific inclination this  $\gamma_b$ - $\phi$  relation may also have cusps similar to the  $\gamma_b$ - $\theta$  relation. Conveniently, the depth of the cusps is characterized by the maximum normalized slope (maximum directional torque) of the energy relation, that is,  $\frac{1}{\gamma_b} \left( \frac{\partial \gamma_b}{\partial \phi} \right)$ .

In an older study of metal wires exhibiting a bamboo structure Hees (1952) observed that some of the grain boundaries were not perpendicular to the wire axis. In such a system, the geometrical condition for a minimization of the grain boundary energy is that the normalized directional torque  $\frac{1}{\gamma_b} \left( \frac{\partial \gamma_b}{\partial \phi} \right) = -\tan \phi$ , where in this case  $\phi$  was measured with respect to the wire axis. He found that the normalized torque terms on random grain boundaries in high purity aluminium ranged from 0.10 to 0.29  $\text{rad}^{-1}$ , with the majority between 0.14 and 0.19  $\text{rad}^{-1}$ . He also estimated the normalized torque terms on the coherent twin boundary in aluminium to be at least 1.7  $\text{rad}^{-1}$ . From studies on boundary morphology in annealed high purity aluminium sheet Miller and Williams (1967) found that the grain boundary torque varies from zero to about 0.3  $\text{rad}^{-1}$ , having a median value of 0.10  $\text{rad}^{-1}$  and a nodal value of 0.06  $\text{rad}^{-1}$ . Gjostein (1969) in reinterpreting the measurements of Murr (1968), concluded that grain boundary torque should be relatively large compared to the ratio  $\frac{\gamma_t}{\gamma_b}$  (where  $\gamma_t$  is the energy of a coherent twin boundary). Assuming that the energy of a random grain boundary is relatively constant, the observed distribution in the measured values of  $\left( \frac{\gamma_t}{\gamma_b} \right)$  (Murr 1968) may be used to estimate the grain boundary torque. Basterfield and Miller (1969)

showed that the observed wide spread in the energy ratio  $\frac{\gamma_s}{\gamma_b}$  could be accounted for by assuming a value of about  $0.1 \text{ rad}^{-1}$  for the torque of the grain boundaries. In studies of faceted high angle  $\langle 10\bar{1}0 \rangle$  tilt boundaries in high purity zinc for the disorientation range from  $31^\circ$  to  $36.5^\circ$  Bishop et al. (1971) found that the minimum value for the normalized torque terms on the facets varies between  $0.09$  and  $0.55 \text{ rad}^{-1}$ .

Gleiter (1970) has studied high angle tilt boundaries in a copper-aluminium alloy as a function of boundary inclination. In this study, a single recrystallized grain at a high angle disorientation was nucleated to many adjacent subgrains to create a number of triple junctions. He found that the energy of a high angle tilt boundary does vary with its inclination, with the symmetrical boundaries having the lowest energy. One of the boundaries studied was approximately at a  $23^\circ$  orientation to the subgrains and a substantial minimum in energy was found at the symmetrical inclination. The other boundary was at a  $25^\circ$  orientation and only showed a small minimum at the symmetrical orientation. However, the actual magnitude of torques measured in this study are unreliable.

Further evidence which supports the view of the dependence of the grain boundary energy on boundary inclination is due to the experiments of Masteller and Bauer (1976). In this study the grain boundary torques were estimated from the displacement of a boundary in high purity aluminium bicrystals. This means that this method is independent of an attainment of configurational equilibrium. From measurements made on certain  $\langle 110 \rangle$  symmetrical boundaries, they found

that the (111) and (113) twin boundaries are characterized by large values of torque at all temperatures investigated, whereas the (112) twin boundary is characterized by a large value only at relatively low temperatures. They concluded that a qualitative ranking of the magnitude of normalized values of torque suggests that the largest value is associated with the (111) twin boundary followed by, in order of decreasing magnitude, the (113), (112) and (221) twin boundaries and the  $10^\circ$  low-angle boundary. In fact, this ranking is in accord with progressively decreasing degrees of atomic fit at the boundary as predicted from CSL theory. Further, since the magnitude of the normalized grain boundary torques is proportional to the depth of the cusp in the  $\gamma$ - $\delta$  relations, such cusps, therefore, are consistent with the significant degree of dependence of grain boundary energy on boundary inclination.

#### 2.5.3 Variation with impurity

Segregation of solute atoms to the boundary is especially effective in reducing the grain boundary energy. There is some evidence (Pumphrey 1976) that the energy of random high angle boundaries is reduced much more as the solute concentration is increased than the energy of special boundaries, which in turn suggests that a preferred segregation of solute atoms at random boundaries occurs. In a nominally pure metal, however, the effect of solute atoms on grain boundary energy is less or not significant at all.

#### 2.5.4 Variation with temperature

Since most techniques which are used to measure the energy of a

grain boundary are limited to temperatures near the melting point, only very little information is known about the temperature dependence of the grain boundary energy.

McLean and Mykura (1966) have measured the ratio of coherent twin boundary to surface energy in platinum and cobalt over the temperature ranges 920°C to 1560°C and 880°C to 1290°C respectively. They found that for platinum the ratio decreased from 0.060 at 920°C to 0.016 at the melting point, whereas for cobalt the variation was less than the experimental error. The temperature dependence of the surface energy can be estimated from the semi-empirical Eotvos equation (e.g. Hodgson 1972) for the surface tension. The predicted coefficient of the surface energy for platinum is much smaller than the observed change in the energy. This suggests that the energy of coherent twin boundaries varies greatly with temperature.

The thermodynamic treatment of the variation of grain boundary energy with temperature indicates that this in fact is contributed by two terms (Gleiter and Chalmers 1972). The first term is the extra entropy of a grain boundary compared with the same amount of material in the grain interior. The second term comes from the change of the solute concentration at a grain boundary as a function of temperature. This term exists only for grain boundaries in solid solutions. Both terms may be relatively small for special grain boundaries and high for random boundaries. Hence the difference in the temperature coefficients of the two kinds of grain boundaries should be more pronounced in solid solution than in absolutely pure metals.

## CHAPTER 3: THEORETICAL BACKGROUND

### 3.1 Methods of grain boundary energy measurement

Numerous methods have been devised to measure grain boundary energies of various types and several reviews of these have appeared in the literature (e.g. Gleiter and Chalmers 1972, Hondros 1970, Inman and Tipler 1963). In general, the types of experiment performed fall into two groups depending on the techniques employed, some give absolute values and others produce relative values for pairs of interfaces. The latter type of measurements can also be used to derive absolute values of one of the energies if the other is known. The technique employed in the present work for determining grain boundary energies is based on measurements of the equilibrium configuration of intersecting interfaces. The experimental measurement being made is of the groove angle formed at the intersection of a grain boundary with the surface of a specimen. Other methods will also be discussed briefly. All of these techniques will be discussed in terms of the two groups mentioned above.

#### 3.1.1 Relative energies

The methods which are usually used to measure grain boundary energies are the relative ones in which the grain boundary energy is measured with respect to some standard such as surface energy. At high temperatures, rapid atomic movements permit intersecting interfaces to approach an equilibrium configuration, consistent with a minimum in interfacial energy. Most techniques are based on the observation of such an equilibrium configuration and the application

of Equations (2.2) and (2.3). The basic notion of a triangle of forces (Equation 2.3) has widely been applied to various intersecting interface arrangements, to yield ratios of interface energies. The most commonly used situations are the intersection of three grains, grain boundary - surface intersections, coherent twin boundary - surface intersections and coherent twin boundary - grain boundary intersections.

Aust and Chalmers (1950) prepared tricrystals by controlled freezing of molten metal. The sample consists of a bicrystal to which a third crystal which has a large orientation difference with the two, is added. After annealing at a high temperature the three boundary intersection reaches its equilibrium configuration. By assuming all the boundaries are perpendicular to the specimen surface, from measurements of the angles of intersection, the relative boundary energy can then be evaluated using Equation (2.3). Configurational equilibrium at twin boundary - grain boundary intersections has been studied by a number of investigators, for example, Murr and co-workers (e.g. 1969 and 1971), who have used electron microscopy to give 'three-dimensional' pictures of intersections which thus eliminate the need to assume that boundaries are perpendicular to the specimen surface.

#### 3.1.1.1 Grain boundary grooving

When metals or alloys are annealed at sufficiently high temperatures in vacuum or inert gas atmosphere, the grain boundaries will equilibrate with the surface and form a groove along the line of intersection of the grain boundary with the surface. The ultimate

motivation for the formation of the groove is the reduction in interfacial energy of the system. Chalmers et al. (1948) were among the first to describe this thermal grooving at the intersection of a solid-solid interface with the surface as a condition of interfacial free energy minimization. Mullins (1957 and 1960) has treated the conditions of groove formation theoretically on the basis that solid surface energy is independent of crystallographic orientation.

This change in surface profile will take place whenever there exists a mechanism by which atoms can be transported at a sufficiently fast rate. The possible mechanisms that can contribute to the formation of groove profiles are surface diffusion, volume diffusion in the solid, volume diffusion in the vapour (or liquid) phase and evaporation-condensation. Mullins considered each of these mechanisms in turn assuming negligible effect from the others. In practice, it would be expected that all four mechanisms operate simultaneously in the process of grain boundary grooving, but it is usually found that one mechanism is dominant, depending on annealing conditions.

Measurements of groove dimensions and growth rate can be used to determine the ratios of grain boundary energies to surface energies and diffusion coefficients from the equation describing groove growth (e.g. Gjoesten 1963). However, because of difficulties in ensuring that only  $\frac{a}{A}$  single transport mechanism operates, more reliable results are obtained using measurements of the angle formed at the groove root in various thermal etching phenomena to determine energy ratios from interfacial equilibrium conditions.

The equilibrium condition at the root of  $\frac{a}{A}$  grain boundary groove

is determined by the application of the Herring equations (Equation 2.2). For the grain boundary groove depicted in Fig. (3.1), the equilibrium condition is (resolving forces perpendicular to the general specimen surface)

$$\gamma_b \cos \phi - \frac{\partial \gamma_b}{\partial \phi} \sin \phi = \gamma_p \sin P + \gamma_q \sin Q - \frac{\partial \gamma_p}{\partial P} \cos P - \frac{\partial \gamma_q}{\partial Q} \cos Q \quad (3.1)$$

using the symbols as defined in Fig. (3.1). In order to determine grain boundary energies from measurements of the profiles of grain boundary grooves, certain simplifying assumptions are usually made. These are

(i) that the grain boundary is perpendicular to the surface of the specimen i.e.  $\phi = 0$ .

(ii) that the anisotropy of the surface energy is negligible i.e.  $\gamma_p = \gamma_q = \gamma_s$  ,  $\frac{\partial \gamma_p}{\partial P} = \frac{\partial \gamma_q}{\partial Q} = 0$

and (iii) that the groove is symmetrical.

Therefore, Equation (3.1) then reduces to the simplified form

$$\frac{\gamma_b}{\gamma_s} = 2 \cos\left(\frac{D}{2}\right) \quad (3.2)$$

so that the ratio of the grain boundary energy to surface energy can be obtained simply from a knowledge of the dihedral angle  $D$ .

Assumption (i) can be satisfied by using extremely thin specimens whose thickness is less than the equilibrium grain size at the grooving temperature. The grain boundary then tends to line up



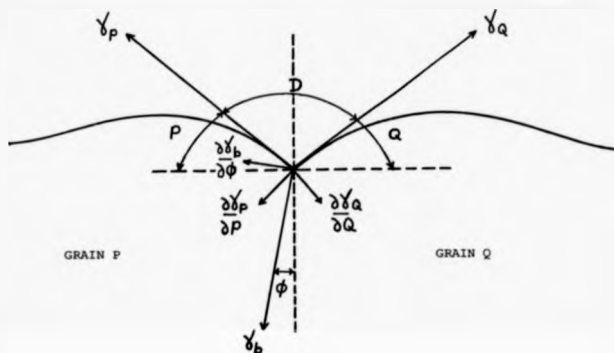


Figure 3.1 Equilibrium configuration at the intersection of grain boundary with surface showing equivalent forces. Angles  $P$  and  $Q$  are the wedge angles which can be measured interferometrically.

normal to the surface. If this is so, assumption (iii) is thus unnecessary; otherwise, for asymmetric grooves, the angles P and Q can be measured separately. Annealed bulk specimens may not exhibit symmetrical intersections in which case, additionally, large unbalance torques may exist, arising from the variation of  $\gamma_s$  with surface orientation and the variation of  $\gamma_b$  with the orientation of the boundary plane (under a condition of fixed crystal disorientation). As it would be extremely laborious to determine all these parameters for a number of individual boundaries, the usual approach has been to rely on the fact that, for a large number of random boundaries, the torque terms are equally likely to be positive or negative and therefore they should not affect the average of a large number of  $\frac{\gamma_b}{\gamma_s}$  ratio measurements, provided there is no marked preferred orientation in the specimen.

The accuracy of the method using grain boundary grooves to measure the boundary energy depends mainly on the accurate measurement of the groove angle D which may be determined directly on a section of the specimen perpendicular to the surface. This technique, however, is laborious, and precautions have to be taken to prevent damage to the surface cutting and polishing the section. More accurate results can be obtained by the use of interference microscopy as described by numerous researchers (e.g. Mykura 1954 and 1963, Tolson and Wood 1956). The highest accuracy in measuring the groove angle may be reached by using the electron microscope to obtain highly magnified images of the grain boundary groove (e.g. Inman et al. 1963, McLean 1973).

The surface torque terms in pure nickel at 1000°C have been determined from measurements of the geometry of twin boundary - surface intersections (see Section 3.1.1.2) by Hodgson and Mykura (1973), using interferometric technique. They found that, except within 10° of the (100) pole and 5° of (111) pole, the surface energy anisotropy was less than 2% and hence had negligible effect on the  $\frac{\gamma_b}{\gamma_s}$  ratios. They also found that, the average correction to individual values of the  $\frac{\gamma_b}{\gamma_s}$  ratio was 20%, but the effect of the surface torque term corrections on the average value of the ratio was less than the experimental error in the ratio. However, in their studies, anisotropy of grain boundary energy was not taken into account since they assumed that the grain boundary runs perpendicular to the specimen surface. Possible inclination of the grain boundary to the surface can be checked by examining both sides of the specimen, but this check still relies on the assumption that the boundary plane is flat. Both grain boundary torque terms and boundary inclination will contribute some error to the  $\frac{\gamma_b}{\gamma_s}$  ratio.

#### 3.1.1.2 Twin boundary grooving

Annealing twins are a well-known feature of recrystallized f.c.c. metals. Mykura (1957 and 1961) first reported on the intersection of twin boundaries with a surface in a pure metal, and demonstrated that the slope of the  $\gamma$ -plot can be determined by applying Herring's equation (Equation 1.2) for the equilibrium angles at twin boundary-surface intersections. Mykura often observed that at the intersection of pairs of coherent twin boundaries with the

surface, if a groove was formed at one of the junctions, a ridge formed at the other coherent twin boundary-surface intersection. The relative magnitudes of the various forces in balance at equilibrium have a marked effect on the morphology of interfaces (see Section 3.3). The energy of a coherent twin boundary is well known <sup>to be</sup> very small ( $\gamma_{\text{TB}} \sim \gamma_{\text{GS}}/50$ ) and may often be smaller than the magnitude of the surface torque terms due to the anisotropy of the surface energy. Consequently, when a pair of twin boundaries is considered (Fig. 3.2), then by symmetry the torque terms at the twin boundary-surface intersection will be of opposite sign, and the 'inverted groove' shape of one of the twins can occur.

If such a pair of twin boundary-surface intersections (Fig. 3.2) is analysed by applying Herring's equation, resolving the forces parallel to the twin boundary to eliminate the boundary torque, the following expressions result

$$\gamma_{\text{E}} = \gamma_{\text{G}} \cos A + \gamma_{\text{A}} \cos B - \frac{\gamma_{\text{G}}}{\sin A} \sin A - \frac{\gamma_{\text{A}}}{\sin B} \sin B \quad (3.3a)$$

and

$$\gamma_{\text{E}} = -\gamma_{\text{G}}' \cos A' - \gamma_{\text{A}}' \cos B' + \frac{\gamma_{\text{G}}'}{\sin A'} \sin A' + \frac{\gamma_{\text{A}}'}{\sin B'} \sin B' \quad (3.3b)$$

using the symbols as defined in Fig. (3.2). In order to obtain a useful form, it is then necessary to make some simplifying assumptions. If it is reasonably assumed that the surface energy is a slowly varying function of orientation and because grain Q and grain Q' have the same orientation, it follows that

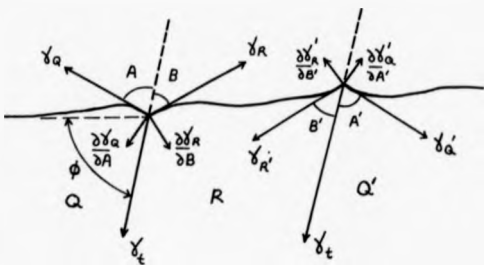


Figure 3.2 Equilibrium configuration at intersection of pair of twin boundaries with surface showing equivalent forces (twin boundary torque omitted).

$$\gamma_a = \gamma_a' , \quad \gamma_b = \gamma_b' , \quad \frac{\partial \gamma_a}{\partial A} = \frac{\partial \gamma_a'}{\partial A'} \quad \text{and} \quad \frac{\partial \gamma_b}{\partial B} = \frac{\partial \gamma_b'}{\partial B'}$$

It is also assumed that  $\gamma_a = \gamma_b = \gamma_s$ , where  $\gamma_s$  is the average surface energy. Addition or subtraction between Equations (3.3a) and (3.3b) followed by suitable algebraic manipulation then yields the expression which can then be used to determine the  $\gamma_s/\gamma_s$  ratios and the surface torque terms. This technique has been used by several investigators (e.g. Mykura 1961, Hodgson and Mykura 1973).

### 3.1.2 Absolute energies

Absolute values of the grain boundary energy can be obtained by the measurements of dihedral angles between three boundaries or from the angle of a surface groove (as described in Section 3.1.1) provided that the energy of one boundary or the surface energy is known. Various methods have been reported in the literature for measuring the absolute value of the surface energy of a solid. Among these are the zero-creep rate technique (Udin 1952), the capillary depression method (Van Vlack 1951), the controlled cleavage method (Gilman 1960), the helium bubble method (Barnes et al. 1960) and the intersections between twin boundary (of known energy) and the surface (see Section 3.1.1.2). If the absolute value of the surface energy is known then the grain boundary energy can then be calculated from the measurement of the groove angle.

Astrom (1956) has devised a precise calorimetry technique for the determination of absolute values of grain boundary energies. This method is based upon the measurement of the total grain boundary

energy obtained by measuring the energy released during grain growth in granules of metals a few millimeters in diameter. While Astrom's calorimetric method of measuring grain boundary energy is a very attractive one because of its direct approach, it has not been extensively utilized by other investigators, primarily because of the precision required in obtaining accurate calorimetric results. Another method of measuring absolute grain boundary energy was used by Mullins (1956) who applied a magnetic field to a notched bicrystal of bismuth. Because the magnetic susceptibility of bismuth is anisotropic and the grain boundary was trapped at its ends by the notches, the applied magnetic field then bowed out the trapped boundary until the restoring effect of its tension just balanced the magnetic pressure. The grain boundary energy could then be calculated from measurements of the boundary curvature on microsections, the crystal orientations on each side of the boundary, the magnetic anisotropy, and the magnitude of the applied field. Such specialized methods are obviously only applicable to a very restricted number of materials.

### 3.2 Grain boundary faceting

The dependence of grain boundary energy on boundary inclination under a condition of fixed crystal disorientation leads in some circumstances to the occurrence of grain boundary faceting. Clearly, as defined in the introduction, the motivation of the process is to reduce the total energy of the system by converting to orientations of lower energy. The break up of a grain boundary into segments of different orientation is usually referred to as an equilibrium

faceting. The splitting of a grain boundary into two boundaries whose total disorientation equals that of the initial boundary, with a new grain appearing, is usually called a grain boundary dissociation. Faceting of this type has to be distinguished from kinetic faceting which can occur during the growth of a new grain or phase when slowly growing crystal faces become prominent, giving the interface a faceted appearance. However, only the former type of faceting will be considered here.

Equilibrium faceting at the solid-vapour interfaces, where it is usually termed thermal faceting, has been studied fairly extensively and was reviewed by Moore (1963). Much less investigation has been made on equilibrium faceting at a grain boundary. The observation of the faceting of a grain boundary implies that facets (low energy boundary planes) exists and such faceting has indeed been found in a number of systems on both macroscopic and microscopic scales and was reviewed by Balluffi (1979).

The energetics of faceting of a grain boundary can, in principle, be investigated graphically using the  $\gamma$ -plot (also called the Wulff plot) in a manner exactly analogous to the thermal faceting case. Here, the radius vector of the  $\gamma$ -plot represents the orientation of the boundary (i.e. the direction of the boundary plane normal  $\hat{n}$ ) and the magnitude proportional to the grain boundary energy. The equilibrium shape of the crystal can then be found through the Wulff construction (e.g. Christian 1975). Faceting of a grain boundary may then occur when the Wulff-plot contains sufficiently deep minima or cusps, and the average boundary inclination corresponds to



one of relatively high energy. An initial boundary then breaks up into low energy facets when the effect of increasing the total area is more than compensated for by effects due to the lower energy per unit area of the facets.

A systematic method for finding the condition for faceting when the  $\gamma$ -plot of surface energy is known has been given by Herring (1951). In fact, this is the same for the grain boundary energy case. The Herring criterion for faceting consists of a construction of a sphere drawn through the origin of the  $\gamma$ -plot which is tangent to the  $\gamma$ -plot at a given orientation of the initial boundary. If the Herring tangent sphere lies everywhere inside the  $\gamma$ -plot except at the tangent (or contact) point, an initial boundary of the given orientation will be stable with respect to a faceted boundary. If, however, the  $\gamma$ -plot passes inside the tangent sphere at any point, then a faceted boundary will be more stable than the initial boundary. Therefore, the Herring construction depicts the physical requirement that the singular facets (the low-index planes corresponding to the cusp orientations in the  $\gamma$ -plot) revealed by faceting have a sufficiently low energy to bring about a reduction in the total grain boundary energy of the system on faceting despite the increase in area.

Mullins and Sekerka (1962) have shown vectorially that faceting problems can be related to the  $\gamma$ -plot and Wulff equilibrium shape. Their more generalized treatment confirms the earlier geometrical deductions of Herring (1951). They also have defined a polar plot called the  $\Gamma$ -plot. This is the smallest plot that will yield the given original Wulff shape under a Wulff construction, that is, it is

contained in all other  $\gamma$ -plots leading to the same shape. In other words, any  $\gamma$ -plot which lies outside the  $\Gamma$ -plot will be unstable against faceting. The difference between the  $\gamma$ -plot and the  $\Gamma$ -plot for a given boundary, therefore, gives the maximum reduction in the total grain boundary energy that can be achieved by faceting.

The same test for faceting conditions can be made much more conveniently using the reciprocal  $\gamma$ -plot (the polar plot of  $\frac{1}{\gamma}$ ) (Frank 1963, Meijering 1963). In this case, an 'external tangent plane' is used and orientations within the points of contact of the plane on this plot are the same unstable orientations as can be found using the Herring construction. The great majority of cases of equilibrium faceting that have been observed are associated with cusps in the  $\gamma$ -plot but this is not a condition for faceting.

The simple example of grain boundary faceting occurs when a singular facet plane is inclined at an angle  $\alpha$  to the initial grain boundary plane. By considering Fig. (3.3), where AC represents the singular facet plane which is crystallographically defined, has an energy  $\gamma_s$  and is inclined at an angle  $\alpha$  to the plane of <sup>the</sup> initial boundary; the plane CE is a (non-low index) continuation facet with an energy  $\gamma_f$ . The total energy of the faceted boundary can then be written as

$$E_{tot} = \frac{\gamma_s \sin \beta + \gamma_f \sin \alpha}{\sin \beta} \quad (3.4)$$

If the singular plane AC is fixed by the crystal orientation, thus, the total energy of the system can change by letting the

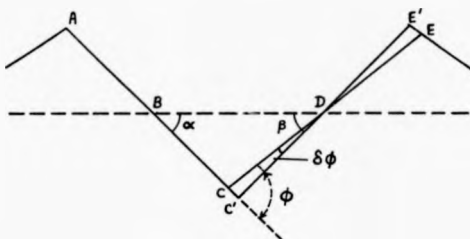


Figure 3.3 Section of a faceted grain boundary showing the various angles defining the facet crystallography; the low index facet AC inclined at an angle  $\alpha$  to the initially flat boundary, the continuation facet CE rotated about D to achieve the equilibrium angle .

continuation plane CE rotate about D to C'E' to achieve the equilibrium contact angle  $\phi$ . By substituting  $\beta = \phi - \alpha$  into the Equation (3.4) and then differentiating the equation with respect to  $\phi$  in order to find the minimum value of  $E_{tot}$ , this gives

$$\gamma_s = \gamma_p \cos \phi - \frac{\partial \gamma_p}{\partial \phi} \sin \phi \quad (3.5)$$

Therefore, at equilibrium, there is a definite angle of contact between the singular facet and the continuation facet given by Equation (3.5) in terms of the relative energy  $\frac{\gamma_s}{\gamma_p}$  and the Herring torque term  $\frac{1}{\gamma_p} \frac{\partial \gamma_p}{\partial \phi}$ . The angle  $\alpha$  does not occur in Equation (3.5) which means that the contact angle  $\phi$  is independent of  $\alpha$ , provided that  $\alpha$  is in the faceting region (i.e.  $\phi > \alpha$ ). If  $\phi < \alpha$ , then the grain boundary will not break up into facets.

When considering a possible rotation of the actual plane away from the low index position AC (Fig. 3.3), similar to the rotation of CE, the fact that  $\frac{\partial \gamma_p}{\partial \phi}$  changes sign discontinuously at the low index orientation causes difficulty. So by performing a similar analysis as was used in obtaining Equation (3.5), the result, therefore, can only be represented as an inequality,

$$\frac{\partial \gamma_s}{\partial \phi} > \gamma_s \sin \phi + \frac{\partial \gamma_p}{\partial \phi} \cos \phi \quad (3.6)$$

Equations (3.5) and (3.6) are essentially Herring's equation (Equation 2.2) with one of the three interfacial energies equal to zero. For certain conditions,  $\frac{\partial \gamma_p}{\partial \phi}$  is small and can be

neglected, so that Equations (3.5 and 3.6) become approximately

$$\gamma_o = \gamma_\phi \cos \phi \quad (3.7)$$

$$\frac{\partial \gamma_o}{\partial \phi} > \gamma_\phi \sin \phi \quad (3.8)$$

giving 
$$\frac{1}{\gamma_o} \left( \frac{\partial \gamma_o}{\partial \phi} \right) > \tan \phi \quad (3.9)$$

Equations (3.7) and (3.9) were used by a number of investigators (e.g. Bishop et al. 1971) to estimate the ratio of the facet energies of low index to high index facets and the Herring torque terms on the faceted boundaries respectively.

Both the Wulff construction for equilibrium shape and the Herring criterion for faceting assume that there is a known  $\gamma$ -plot and then deduce the equilibrium shape from it. In practice, things go in the reverse order, that is, a knowledge of  $\gamma$ -plots comes from, for example, measurements of Herring torque terms which are then integrated to give the  $\gamma$ -plot (Mykura 1961). The experimental measurements are almost always made on specimens which are isothermally annealed at a high temperature and then examined at room temperature. It is assumed that the high temperature shape can be "quenched in" for low temperature examination.

The shape of a macroscopically flat grain boundary will stay flat during cooling, provided that the form of the  $\gamma$ -plot is such that the faceting condition is not satisfied. The increase in anisotropy of the  $\gamma$ -plot with decrease in temperature is such that for a wide

range of orientations, facets will become stable on cooling. The stability range for simple facets is, as discussed above, given by Equation (3.5). In the more general case, Gruber (1963) has shown that the faceting condition is such that

$$\gamma_s + \frac{\partial^2 \gamma}{\partial \alpha^2} < 0 \quad (3.10)$$

for facets to be stable. If the inequality is reversed, then an initially flat boundary is stable. The range covered by Equation (3.10) is usually referred to as a 'spontaneous faceting range'. Gjoestein (1963) has shown that Equation (3.7) is equivalent to the condition that the magnitude of the slope of a plot of  $\frac{1}{\gamma} \left( \frac{\partial \gamma}{\partial \alpha} \right)$  versus  $\alpha$  should be greater than unity, i.e.

$$\left| \frac{\partial}{\partial \alpha} \left[ \frac{1}{\gamma} \left( \frac{\partial \gamma}{\partial \alpha} \right) \right] \right| > 1 \quad (3.11)$$

The most frequently observed facet boundary is the first order twin ( $\Sigma 3$ ) boundary in f.c.c. metals which very readily facets into a common coherent twin boundary and incoherent twin boundary. Crystallographically, the coherent twin boundary is the planar interface parallel to the  $\{111\}$  twinning plane, whereas the incoherent twin boundary which is not parallel to this twinning plane is also frequently planar but the plane of the interface depends on the material (e.g. Fullman 1951).

A grain boundary dissociation has also been observed most frequently in the f.c.c. metals. Fullman and Fisher (1951) have noted

that the dissociation of a grain boundary is possible provided that the energy sum of two resultant boundaries is less than the energy of the starting boundary. The most commonly observed grain boundary dissociation is the second order twin ( $\Sigma 9$ ) boundary which splits up into two first order twin ( $\Sigma 3$ ) boundaries (e.g. Vaughan 1970). It was shown that other special boundaries such as  $\Sigma = 27, 33, 51$  and  $99$  were also able to dissociate (Fionova et al. 1981). As a result of dissociation low energy special boundaries were formed, most commonly including the  $\Sigma 3$  boundary. However, conditions for the process and its mechanism are not clear at present. It is not proved for certain that new special boundaries in the structure of a polycrystal always appear from the dissociation. Nonetheless, a number of mechanisms for this process have been proposed (Vaughan 1970 and Fionova et al 1981).

The faceting of grain boundaries has been studied for a number of metallic systems of high purity. It is common when the grain boundary energy of some grain boundary inclinations has been reduced by impurity adsorption, but rare when the specimens are pure. The theory of faceting discussed above is independent of the size of the facets. When a 'kink energy' for an atom at a point where the boundary changes inclination (facet edge) is considered in addition to the grain boundary energy, then larger facets are found to be more stable than the smaller ones.

### 3.3 Grain boundary morphology in sheet

When a thin metal sheet is well annealed at high temperatures, a number of grains will appear to have a giant size extending through

the thickness of the specimen due to the recrystallization and grain growth processes. A grain boundary groove always occurs along the line where a grain boundary intersects the specimen surface. Most investigators, while acknowledging the possibility that the grain boundary energy may be anisotropic, have usually made the opposite assumption, except for such cases as low angle boundaries, where the boundary energy is known to vary with disorientation, and twin boundaries where the boundary energy must vary strongly with boundary direction. However experimental observations have shown that the energies of other high angle boundaries do depend upon boundary orientation, as briefly reviewed in Section (2.5.2).

Dunn (1966) following Mullins' (1958) earlier analysis, has derived an expression for grain boundary mobility in sheet material when the driving force for grain growth is supplied by boundary curvature and an anisotropy of surface energy. McLean and Mykura (1965) have also considered surface energy induced secondary recrystallization in platinum sheet and obtained a relation from which could be determined whether or not boundaries would migrate under a given set of conditions. However, in their studies, the anisotropy of grain boundary energy was not taken into account. The anisotropy of grain boundary energy (grain boundary torque) is important and must be taken into consideration in grain boundary studies since it can have a marked effect on grain boundary morphology in sheet.

Consider a stationary grain boundary penetrating a sheet specimen for a number of the following simple cases,

- (1) If all interfacial energies are assumed to be isotropic, the



system would attain minimum energy when the boundary was perpendicular to the sheet surface.

- (ii) If surface energy is alone assumed to be anisotropic, the boundary would then become smoothly curved when viewed on a plane perpendicular to the sheet surface in order to minimize the interfacial energy of the system. Mullins (1958) has shown that such boundaries (except in the region of triple points) should have the catenoid shape developed by suitably anchored boundaries, that is the shape assumed by a soap film stretched between two parallel circular frames.
- (iii) If grain boundary energy (in addition to surface energy) is assumed to be anisotropic, the boundary would then attempt to straighten and to rotate toward its position of minimum interfacial energy, while at the same time attempting to become curved as in the case (ii) above. These phenomena would obviously cause complex curvature to be introduced into the boundary, as indeed was found to be the case in aluminium sheets by Miller and Williams (1967).

Therefore, the anisotropy of both the grain boundary energy and surface energy is important in determining the morphology of grain boundaries in sheet specimens.

#### CHAPTER 4: DISORIENTATION DETERMINATION

Various methods have been used for the determination of the crystallographic orientation of single crystal solid specimens. The Laue X-ray method is the standard technique for the orientation determination of large single crystals (e.g. Cullity 1978), but for individual small crystals in a polycrystalline specimen, the selected area electron channelling pattern technique in the scanning electron microscope (SEM) is the most useful one. This technique has been used extensively in the present work. It seems appropriate, before discussing the details of the experimental technique for obtaining the s.a.c.p.'s in the SEM and the orientation determinations using such patterns, to discuss briefly the general theory and applications of s.a.c.p.'s. A detailed discussion on this subject is covered in the paper by Joy et al. (1982), who also gives the references to the earlier literature.

##### 4.1 General theory and applications of selected area electron channelling patterns (s.a.c.p.'s)

The study of crystalline materials in the SEM has been greatly advanced by the discovery of electron channelling patterns (e.c.p.'s) from bulk specimens (Coates 1967). These patterns arise because the manner in which the incident electron beam is scattered by the specimen depends on the angle the beam makes with the crystallographic planes within the specimen.

As an electron beam scans the flat surface of a single crystal

as in Fig. 4.1(a), its angle to the lattice plane changes and thus the backscattered signal will vary typically as shown in Fig. 4.1(b).

Major changes in the profile occur whenever the incidence angle  $\theta$  is equal to the Bragg angle  $\theta_B$ , i.e. for the values of  $\theta$  that satisfy the Bragg equation.

$$2d\sin\theta = n\lambda \quad (4.1)$$

where  $d$  is the crystallographic plane spacing,  $\theta$  the Bragg angle,  $n$  the order of the reflection and  $\lambda$  the electron wavelength. At point P and Q,  $\theta = \theta_B$ , so between these positions the beam incidence angle  $\theta < \theta_B$  and the backscattering signal is seen to be high, while before P and after Q,  $\theta > \theta_B$  and the back-scattering signal falls. The backscattering signal profile as a function of the beam position therefore consists of a bright band of contrast with an angular width  $2\theta_B$ . This is flanked on either side by higher order lines corresponding to the  $2\theta_B$  values obtained in the Equation (4.1) by putting  $n=2,3$ , etc. The mechanism of contrast formation may be explained theoretically by regarding a diffracted beam as consisting of two types of superimposed Bloch waves (Joy et al. 1982). Since in a real crystal there are many other crystallographic planes running in many directions, these contribute analogous changes in signal profile, and so complex patterns occur in the image representing the symmetry of the lattice about the beam direction. The geometry of the patterns is similar to Kikuchi patterns (e.g. Thomas 1970). Tilting or rotating of the specimen causes the patterns to move laterally or rotate respectively, but lateral movement of the specimen does not affect the patterns. Although the reflective mode is often used to

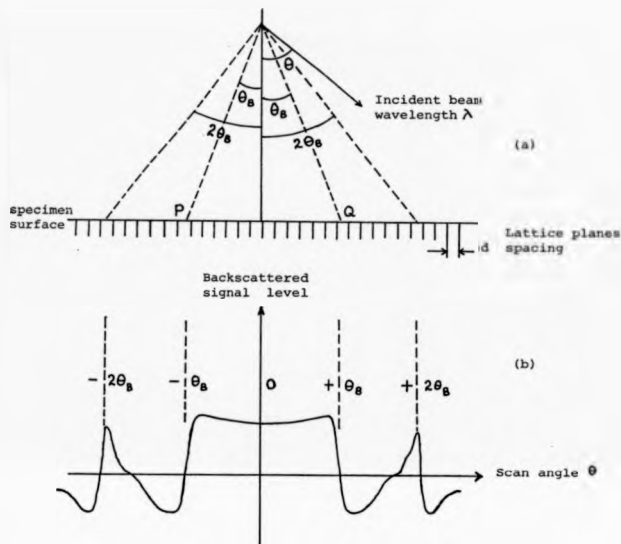
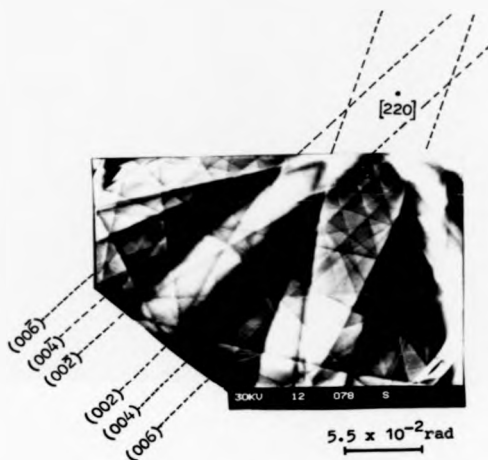


Figure 4.1 (a) Changes in the geometry of an incident beam during scanning over a flat crystal surface. The incidence angle  $\theta$  will vary from being greater than the Bragg angle  $\theta_B$  to being smaller than  $\theta_B$ , and at two symmetric positions P and Q, the first-order reflections occur when  $\theta = \theta_B$ . Similarly the higher-order reflections occur when  $\theta = n\theta_B$  where  $n = 2, 3$ , etc. (b) Shows the variation of backscattering signal intensity as a function of scan angle  $\theta$  results from condition in (a). (Joy 1974).

detect channelling patterns, they can also be seen in the emissive and absorptive modes.

The great disadvantage of the operating conditions described thus far is that to achieve a large angle of scan, a low magnification must be used which in turn necessitates a large single crystal specimen (typically about 3mm in diameter). Consequently it is not suitable for examining individual grains of interest in polycrystalline specimens. This limitation can be overcome by using a s.a.c.p. method where the change in angle of the incident electron beam relative to the lattice plane is obtained with minimal lateral motion of the probe occurring. Two methods of producing s.a.c.p.'s have been proposed. Coates (1967) suggests that this might be obtained by using a stationary electron beam and rocking the specimen. Alternatively, the specimen is kept stationary and the beam is rocked about a point on the specimen surface. This latter method is the most common technique used on several types of instruments such as Cambridge Stereoscan and Philips. A typical s.a.c.p. of copper <sup>using</sup> 30kV incident electrons obtained by <sup>the</sup> rocking beam method, as will be described below, is shown in Fig. 4.2. On the pattern are indicated the crystallographic orientations of the planes and directions relevant to the pattern.

The electron ray paths in <sup>the</sup> lower portion of SEM in the normal (micrograph) and s.a.c.p. (rocking beam) modes are as shown diagrammatically in Figs. 4.3(a) and (b-d) respectively. In the normal mode of operation, the scanning action is performed by using two sets of scan coils located between lenses 2 and 3. The angular divergence  $2\alpha$  of the final electron probe is controlled by the final



**Figure 4.2** A typical selected area electron channelling pattern (s.a.e.c.p.) of copper at 30 kV showing crystallographic features of the pattern; hkl designates diffracting plane.

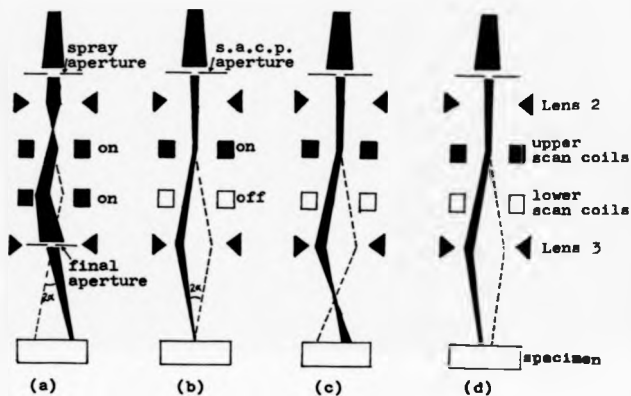


**Figure 4.3** Line diagram showing electron optical ray paths in lower portion of SEM. (a) normal (micrograph) mode (b) s.a.c.p. mode, in focus, (c) s.a.c.p. mode, overfocus, and (d) s.a.c.p. mode, under focus (Joy and Bocker 1971).

aperture. For the resulting micrograph to be in focus, the final lens is adjusted until the electron probe is focussed on the specimen surface. In the s.a.c.p. mode, the rocking beam action can be achieved by deactivating the lower set of scan coils. Since the presence of a small final aperture would restrict the rocking beam action, the final aperture slide is usually made to be a large hole. In this case, the final aperture no longer defines the beam divergence. To limit the beam divergence, a small aperture ( $\sim 50\mu\text{m}$  in diameter) must be used. This aperture is normally placed at the position above the scan coils. The crossover position depends on the strength of the final lens. Varying the vertical position of the crossover changes the area scanned in the s.a.c.p. mode (Fig. 4.3(b-d)). The change in scanned area as a function of crossover position can be used to produce a "through-focus series", in which the crossover point is sequentially placed above, at and below the specimen surface (Figs. 4.3 and 4.4).

In Fig. 4.4(a), a  $\times 300$  magnification micrograph of a typical area in a polycrystalline copper is shown. The beam is nearly normal to the specimen surface at all points. In the s.a.c.p. mode of operation with the crossover point above the surface, a large area is scanned, and across this area, the beam-specimen angle changes through a considerable angle due to the rocking action (Fig. 4.3(b)). Thus the grain labelled A in the normal image (Fig. 4.4(a)) can be recognized in the s.a.c.p. image (Fig. 4.4(b)). It can be seen that the effective magnification of grain A increases as the crossover point is brought closer to the specimen surface, and hence the area scanned



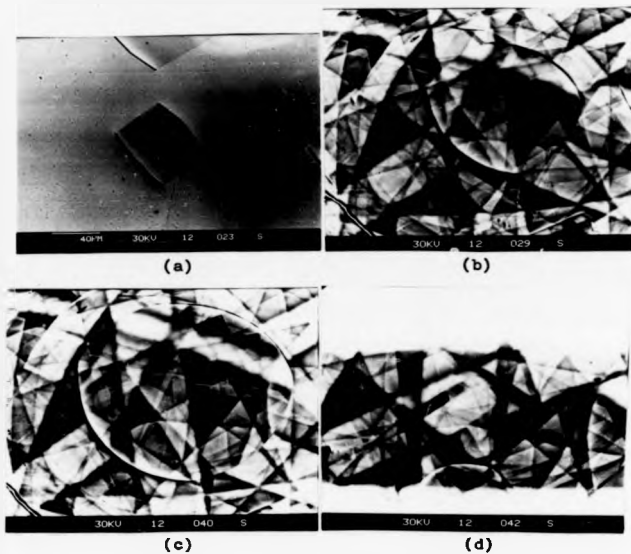


**Figure 4.4** A typical polycrystalline copper specimen with a small twin (labelled A) in the centre of field of view, (a) normal (micrograph) mode, (b)-(d) "through-focus series" in the s.a.c.p. mode. The "focus" position corresponds approximately to (c).

decreases. More of the channelling pattern of grain A, located at the centre of the image, is observed as the crossover point is brought closer and closer to the specimen surface. When the crossover is coincident with the surface, the magnification is a maximum; the s.a.c.p. of grain A is thus obtained and its orientation relative to the beam is found to be about  $5^\circ$  off the  $[112]$  pole (Fig. 4.4(c)). When the crossover point is moved below the specimen surface, the area scanned increases and grains surrounding grain A are again observed (Fig. 4.4(d)), but the image is now reversed by  $180^\circ$  from the image of Fig. 4.4(b), since the first scan ray now strikes the left side of the field first, instead of the right. The through-focus series can be carried out rapidly, since all that is involved in changing the image in the sequence illustrated in Figures 4.4(b-d) is to change the s...length of the final lens by approximately 0.1amp. The through-focus series thus provides a rapid means to identify precisely and rapidly the area from which the s.a.c.p. is obtained.

As discussed above, the selected area from which the pattern is obtained is  $A_{\min}$  minimum when the crossover is coincident with the specimen surface. If the focusing were perfect, this crossover would be practically a geometric point and the effective magnification would be nearly infinite. However, lens defects, principally spherical aberration, cause the crossover to have a finite lateral size. The minimum obtainable diameter  $D_{\min}$  of this area is given by

$$D_{\min} = \frac{1}{2} C_s \alpha^3 \quad (4.2)$$

where  $C_s$  is the final lens spherical aberration coefficient and  $\alpha$  is the semiangle of rock. The coefficient  $C_s$  is a decreasing function of lens excitation, and hence it is advantageous to operate with the specimen as close as possible to the pole piece of the final lens, so the excitation can be maximized. The interrelationship of the minimum selected area size, angle of rock and working distance from the final lens has been determined in detail for a particular system by Booker and Stickler (1972). The minimum specimen area size from which the pattern is arising can be deduced relatively easily when the through-focus series is performed as described previously. The perfect adjustment produces a pattern from an area of about  $5 \mu\text{m}$  in diameter, or even smaller depending on an optimum conditions setting.

The s.a.c.p. technique has been used for a variety of applications in material investigations as listed in the papers by Davidson (1984) and Schulson (1977). In general, two main types of information can be obtained from s.a.c.p.'s. First, from the geometry of the patterns, crystallographic orientations, crystal structures, lattice parameters, etc., can be determined. These crystallographic features can be deduced either by analysis or by comparing the patterns with a standard map containing the stereographic unit triangle. Second, from the quality of the patterns such as the changes in contrast, form and resolution, information can be obtained concerning the occurrence of lattice defects at particular specimen locations.

#### 4.2. Experimental technique for obtaining s.a.c.p.'s in the scanning electron microscope (SEM)

##### 4.2.1 Specimen preparation

High purity copper wire and sheet specimens used in the present work were prepared as will be described in Chapter 5 and 6 respectively.

Since s.a.c.p. comes from relatively near to the surface layer (less than 100nm thick), careful specimen preparation is really important. The specimen surface must be as clean as possible and free from any mechanical damage. Excessive films, such as oxides, will cause a general blurring or loss of contrast of the pattern. Mechanical damage such as plastic deformation which may be due to bending or mechanical polishing leads to line broadening and attendant reductions in contrast. It has been reported that if the specimen surface has a roughness, a distortion and excessive films 50nm to 100nm in thickness, it is impossible to obtain s.a.c.p. from such area of the specimen (Nakagawa 1986). The requirements of a smooth and strain free surface are most readily met by chemical or electrochemical polishing rather than mechanical polishing. An excellent pattern is easily generated when the annealed specimens (prepared as described in Chapters 5 and 6) are put in the SEM without further treatment.

##### 4.2.2 Setting-up procedures

A basic procedure for obtaining s.a.c.p.'s with the SEM has been outlined by Joy and Booker (1972). However, the appropriate procedure

will obviously depend on the type of instrument used. This description relates specifically to the Cambridge Stereoscan 250 MK 3. When switched to s.a.c.p., the operating mode of the column is quite different from normal, so before continuing it will be appropriate to make a note here of the notation and the function of the lenses used in this mode.

- C<sub>1</sub>: Current adjusted by the 'spot size' coarse control which controls the beam diameter (gun diameter demagnification) and also the angular resolution of the s.a.c.p.
- C<sub>2</sub>: Current adjusted by the 'spot size' fine control, which is adjusted so that it produces a beam cross over in the plane of the upper scan coils (the lower scan coils are automatically switched off when the SEM is switched to the 's.a.c.p.' mode) and a conjugate point on the specimen surface. Adjustment of C<sub>2</sub> current focuses the pattern and this lens is sometimes known as 'the pattern focusing lens'.
- C<sub>3</sub>: Current adjusted by the 'focus' control which is adjusted so that the electron beam pivots precisely on the specimen surface. The adjustment of C<sub>3</sub> current to achieve this condition is at first sight a little complicated and is known as setting 'the point of infinite magnification'.

The instrument was also equipped with a backscattered detector (BSD) and this is important because for backscattered electrons, the image contrast is much greater (40%). The setting-up procedures for obtaining s.a.c.p.'s in the particular type of instrument used in this

work is as shown in Fig. 4.5 which can be summarized as the following steps:

- ( 1 ) The specimen is set normal to the optic axis of the microscope (zero tilt) and at working distance (WD) of 5 to 10mm.
- ( 2 ) An image is focussed (in normal mode) using  $C_3$  lens current. An interesting area is selected and moved to the centre of the viewing screen.
- ( 3 ) A 'small' aperture of diameter about 50 $\mu$ m is inserted; the acceleration voltage is  $\overset{\text{set}}{A}$  at 40kV (see the problem later) and the filament is made to be fully saturated and well-centred.
- ( 4 ) The SEM is then switched to 's.e.p.' (on the 'optibeam' control).
- ( 5 )  $C_1$  is set to 1.0 amp and  $C_2$  to 2.0 amp.
- ( 6 ) A normal image is obtained.
- ( 7 ) The 'small' aperture is centred by wobbling and focussing in the usual way.
- ( 8 )  $C_1$  is then set to 1.0 amp and  $C_2$  to 0.4 amp.
- ( 9 ) The gun is aligned by setting the small gun alignment knobs to zero (both pointing upwards) and the knobs of the large gun alignment are adjusted until the signal (indicated by the meter) is maximised.
- (10) The 'magnification' is set to about X30.
- (11) The SEM is then switched to 's.a.c.p.' mode (on the 'optibeam' control).

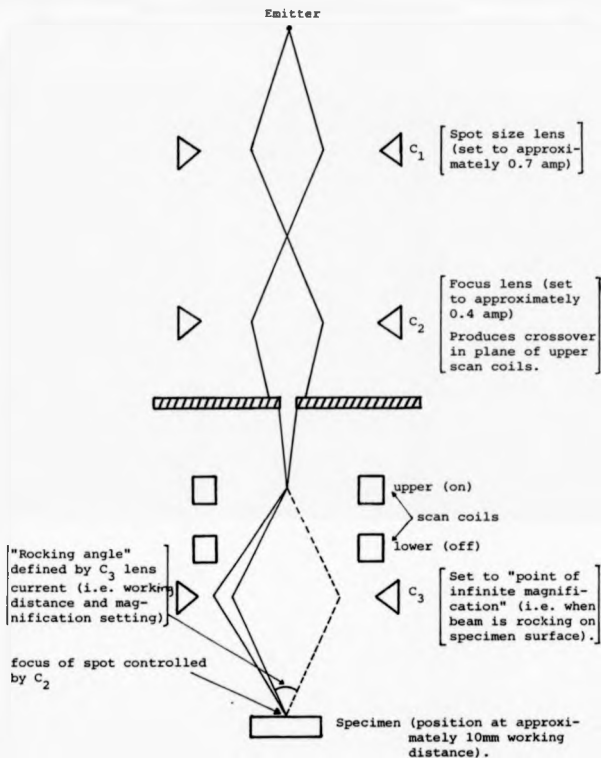


**Figure 4.5** Setting-up procedures for obtaining selected area electron channelling pattern in the Cambridge Stereoscan 250 MK 1.

- (12)  $C_1$  is set to 0.7 amp and  $C_2$  to 0.4 amp.
- (13) The 'point of infinite magnification' is achieved by adjusting the  $C_3$  lens current (this was found to be about 1.3 amp when the specimen was at WD = 8mm).
- (14) An adequately large amount of contrast is used to obtain a good s.a.c.p.
- (15) The s.a.c.p. is focussed by adjusting the  $C_2$  lens current.
- (16) The 'small' aperture is re-aligned by wobbling the  $C_2$  lens current if the image is desired (optional).
- (17) The s.a.c.p. is re-focussed by adjusting the  $C_2$  lens current and step (13) is re-checked.

#### An Instrumental problem

To image<sup>a</sup> s.a.c.p., it is highly desirable to use the maximum available electron gun accelerating potential. This has the distinct advantage of giving narrower channelling bands together with higher signal levels especially when using the backscattered mode. The narrower bands make the orientation determination much easier. In the Cambridge Stereoscan 250 Mk 3, this maximum potential is about 40 kV. During the earlier stage of the present work, the use of such a maximum accelerating potential produced no difficulties. However, when a new instrument of the same type was installed, considerable instrumental problems arose when using 40 kV. Severe discharges in the gun occurred causing further logic circuit problems, which meant that a compromise in accelerating potential of about 30 kV had to be used for a substantial amount of the work. The setting-up procedure given above was similar for all voltages. A later



modification to the anode design enabled higher voltages to be used again.

#### 4.3 Orientation determinations using s.a.c.p.'s

##### 4.3.1 The stereographic projection

Since most of our work is dealing with the use of the stereographic projection for representing, in two dimensions, the three-dimensional relationships between crystal faces, so it is appropriate here to discuss briefly its basic properties and general features. A detailed explanation on this subject is covered elsewhere (e.g. Cullity 1978, Johari and Thomas 1969).

The use of perspective drawings to illustrate the faces exhibited by a crystal is unsatisfactory since they are difficult to construct and do not yield quantitative information easily. In the stereographic projection a sphere is imagined to surround the crystal and from the centre of the sphere, normals are drawn to the crystal planes. The point at which each normal intersects the sphere is then projected back through the equatorial plane, which is the plane of projection, to the pole of the lower hemisphere. The points where these lines cut the equatorial plane are the stereographic poles of the corresponding faces. The stereographic poles of faces whose normal cut the sphere in the lower hemisphere will project outside the projection of the equator (or primitive circle), but they may also be projected inside this circle by using the upper pole as the pole of projection.

A complete stereographic projection of some particular set of

poles is usually called a stereogram. The curves connecting the poles are great circles (i.e. circles whose planes pass through the centre of the original sphere) or zones. A set of faces whose normals are co-planar are said to lie in a zone and the edges formed by their intersections are all parallel to a single direction which is called the zone axis. It is a property of the stereographic projection that all zones project as circles on the stereogram and pass through diametrically opposite points on the primitive circle. A small circle or projection sphere is the locus of points which are at equal angular distances from a point on the sphere. Small circles project as circles, but in general the centre of the small circle will not project as the centre of the circle on the stereogram.

It is often more convenient to prepare stereograms with the help of stereographic nets. A stereographic net is simply a stereographic projection of the lines of latitude and longitude of a sphere on to a central plane. The most commonly useful stereographic net is the Wulff net. This net is available in various sizes, one of which is 20cm diameter graduated at  $2^{\circ}$  intervals giving an accuracy of about  $1^{\circ}$ . The latitude lines on a Wulff net are small circles extending from side to side and the longitude lines (meridians) are great circles connecting the north and south poles of the net, as also is the equator.

In order to construct stereograms with the help of the Wulff net, it is most convenient to work on tracing paper over the net, using the same scale and centre as the net. Angles between poles are measured along the great circles. Thus, to measure angles

between two poles, the tracing paper is rotated about the centre until either (a) the poles both lie on the same meridian, when the required angle is the latitude difference measured along that meridian, or (b) the poles both lie on the equator of the net, in which case the required angle is obtained from the angle scale along the equator. The zone axis or pole of a great circle can easily be located on the stereogram since it is  $90^\circ$  from all points in the zone. The angle  $\phi$  between two poles  $(h_1k_1l_1)$  and  $(h_2k_2l_2)$  can also be calculated by using the formula, for cubic crystals

$$\cos \phi = \frac{h_1h_2 + k_1k_2 + l_1l_2}{[(h_1^2 + k_1^2 + l_1^2)(h_2^2 + k_2^2 + l_2^2)]^{1/2}} \quad (4.3)$$

#### 4.3.2 The Generation and indexing of the unit triangle map

If the zones and poles which make up the channelling pattern can be identified and indexed as arising from known crystallographic planes, then the orientation of a particular crystal can be determined. The simplest way of doing this is by matching the pattern from the sample with a reference pattern whose orientation is already known. In the case of cubic crystals, this reference pattern is usually obtained within the "unit triangle" defined by the  $[001]$ ,  $[011]$  and  $[111]$  poles, which then is usually referred to as a "unit triangle map".

For a given cubic crystal, a unit triangle map can be built up by joining together a series of channelling patterns taken from a single crystal of the material as it is successively tilted to new

positions within the unit triangle. For an angle of rock of about  $10^\circ$ , a map can then be assembled from about 15 carefully chosen exposures. A map can of course be assembled from a fewer number of exposures obtained with a larger angle of rock, but the inevitable distortion in the scanning system will bend the lines and bands on the pattern and make it difficult to assemble the exposures. Equally, the map can also be made from a larger number of exposures obtained with a small angle of rock, but in this case, the visibility of detail is decreased because of the difficulty of matching up the boundaries between exposures.

It might appear, at first, necessary to make a map for every particular crystal and accelerating potential of interest. This is fortunately not the case. The angles between planes in the cubic system are the same for all lattice parameters, so the position of the poles on all cubic maps will be the same. However, the visibility of any given band or pole will depend on whether the crystal is simple cubic, face centred cubic (f.c.c.), body centred cubic (b.c.c.), or diamond cubic. There will thus be detailed differences between the maps for each of these systems. The appearance of the maps will also be a function of the accelerating potential of the microscope and the lattice parameter of the specimen.

The channelling pattern obtained from a particular crystal can of course be identified by comparing with ~~the~~ <sup>one of</sup> different lattice parameter but of the same lattice type. However, this method is not justified since the detailed structures between the two differ. This is similar to the case where the pattern and the reference map have the same

lattice parameter but differ in accelerating potential. A better way to identify the unknown pattern is to compare with the reference map of the same lattice parameter and accelerating potential. For the purposes of the present work, unit triangle maps for copper at 20kV and 40kV were generated, as shown in Figs. 4.6 and 4.7 respectively. These maps were assembled from a number of exposures taken from individual grains in a polycrystalline copper sheet which were successively tilted about  $10^\circ$  to new positions within the unit triangle. Of course, a better way to generate the map is by using exposures taken from a hemispherical shape crystal. In this case, the mean angle of incidence of the beam to the specimen surface is always the same regardless of tilt and such difficulties like uneven illumination of the pattern, asymmetric channelling contrast, etc., as can be seen in both maps shown in Figs. 4.6 and 4.7, are then eliminated. Fig. 4.8 shows the construction of the unit triangle map for <sup>the</sup> f.c.c. system showing major zones and poles which were indexed using the following steps:

- ( i ) The major low index poles [001], [011] and [111] were positioned.
- ( ii ) The important zones were then inserted. The zones which appeared were those which satisfied the allowed reflection rules. For instance, in a f.c.c. crystal, the lowest important zones allowed are (111), (200), (220), (311), etc., i.e. hkl all odd or all even. The zone (uvw) passing through the pole [hkl] must satisfy the Equation

$$hu + kv + lw = 0 \quad (4.4)$$



Figure 4.6 Unit triangle map of copper at 20kV in backscattered mode.

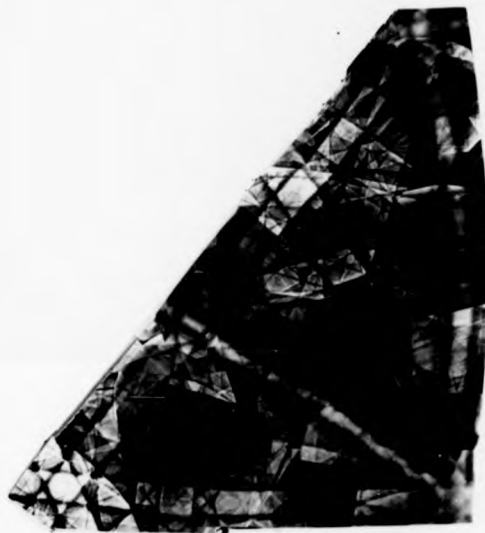
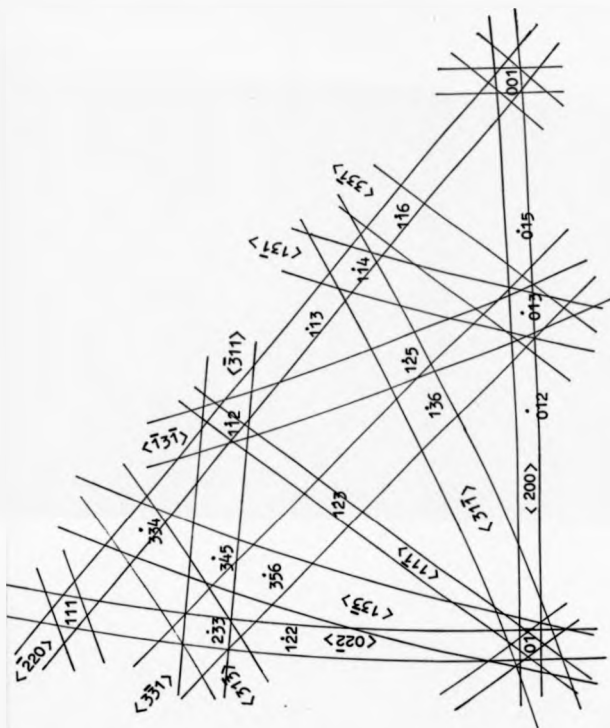


Figure 4.7 Unit triangle map of copper at 40kV in backscattered mode.



**Figure 4.8** Indexing guide for the f.c.c. system showing the major bands and poles.



(iii) The indices of other zones and poles were then identified.

The pole  $[hkl]$  lying at the intersection of the zones  $(u_1 v_1 w_1)$  and  $(u_2 v_2 w_2)$  has indices satisfying the simultaneous Equations

$$\begin{aligned} hu_1 + kv_1 + lw_1 &= 0 \\ hu_2 + kv_2 + lw_2 &= 0 \end{aligned} \quad (4.5)$$

that is  $h = (v_1w_2 - v_2w_1)$ ,  $k = (w_1u_2 - w_2u_1)$  and  $l = (u_1v_2 - u_2v_1)$ . As standard <sup>the</sup> <sub>index</sub> in Miller notation, the lowest common denominator of the  $hkl$  values represents the correct value.

Thus, for example, the  $\{200\}$  and  $\{220\}$  zones intersect at the  $[002]$  pole and the  $\{111\}$  and  $\{220\}$  zones intersect at  $[\bar{2}20]$  pole.

#### 4.2.3 Relative rotation between s.a.c.p. and normal micrographs

When <sup>the</sup> crystallographic orientation of the crystals is to be determined using s.a.c.p.'s, both normal and s.a.c.p.'s micrographs have to be taken separately. There is a relative rotation between a particular crystallographic direction in the s.a.c.p. and the corresponding direction in the normal micrograph which occurs because of the change in the optical ray paths between the normal and s.a.c.p. modes of operation. This effect has been reported for some particular types of instruments (Van Essen and Verhoeven 1974, Verhoeven and Gibson 1975, Joy and Maruszewski 1975, Davidson 1976). However, the magnitude of the rotation varies from one instrument to another as well as with the exact operating conditions used. It must, therefore,

be experimentally determined for each microscope to be used, before accurate orientation determinations of the crystals are attempted, since the correction can be large. The same effect also occurs in the Cambridge Stereoscan 250 Mk 3 used in the present work and is reported here.

The relative rotation between s.a.c.p. and normal micrographs was measured in the following way. A polycrystalline copper specimen was set at zero tilt i.e. the specimen surface was set normal to the optic axis of the microscope. A particular grain which has a number of coherent  $\Sigma 3$  twin boundaries running in many directions was chosen and set to be about the centre of the viewing screen. Ordinary micrographs of both sides of the specimen surface which contain this particular grain as well as the edge of the specimen were taken. By matching the specimen edge, the direction of the boundary plane was then determined using the method as will be described in Chapter 6. The orientation of this particular grain was then obtained by plotting all the  $\langle 111 \rangle$  poles on the stereographic projection. The orientation of the corresponding grain was also determined using the s.a.c.p. as will be described in detail in the next section. This work was carried out for a number of similar grains at several accelerating potentials and working distances.

A possible "tilting effect" between s.a.c.p. and ordinary micrograph was also checked. This was done by plotting a particular direction of  $\{111\}$  plane, measured from both ordinary and s.a.c.p. micrographs, on the stereographic projection with the surface normal and the centre of the pattern always coinciding with the centre of the

stereographic net. As a result, it was found that the corresponding poles have the same "tilt angle" (measured in degree on the stereogram). When the relative rotation between s.a.c.p. and ordinary micrographs were taken into consideration, these poles were found to coincide. This means that there is no tilting effect between s.a.c.p. and ordinary micrograph. In other words, it is always true that at zero tilt, the direction of the specimen surface normal is parallel to the optic axis of the microscope. This effect was checked several times and the same result obtained to an accuracy better than  $2^{\circ}$ .

There are two types of relative rotation between s.a.c.p. and ordinary micrographs. The first type is a variable rotation dependent on the working distance. When an angle made between one of the lines (or bands) on the s.a.c.p. and any reference directions (e.g. "line set" on the display screen) is measured, it is found that there is a variation in the angle as a function of working distance. This rotation occurs in a clockwise sense as the working distance is increased as can be seen in Fig. 4.9. The same effect also occurs for the ordinary micrograph. However, the amount of rotation at the same working distance for the s.a.c.p. is greater than for the ordinary micrograph, thus relative rotation results. The second type is a rotation of  $180^{\circ}$  of the s.a.c.p. with respect to the ordinary micrograph. Thus the net relative rotation between the s.a.c.p. and micrograph is therefore a combination of these two types of rotation which is in a clockwise sense. The result of this effect at 30 kV accelerating voltage as a function of working distance and final lens ( $C_3$  lens) current is shown in Figs. 4.10 and 4.11 respectively. Not

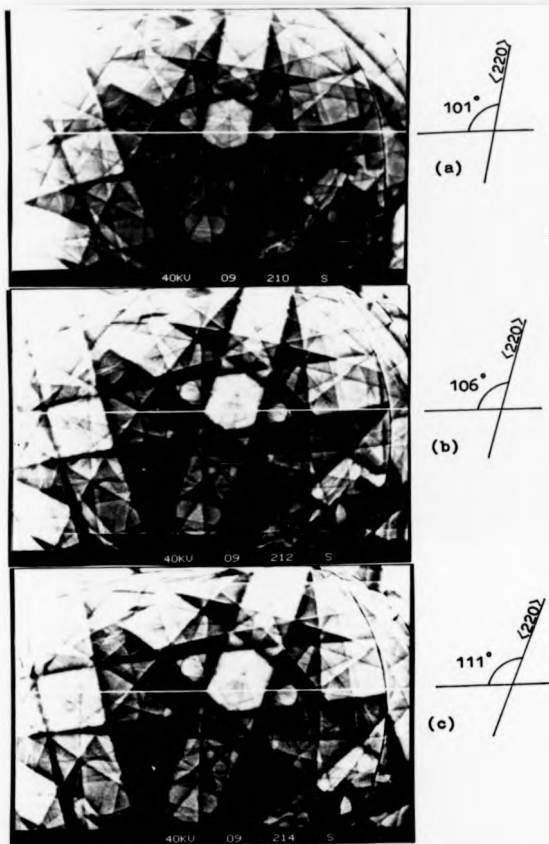


**Figure 4.9** Rotation of a.s.c.p. at 40kV for different "working distance" settings (a) 7mm, (b) 9mm and (c) 11mm.

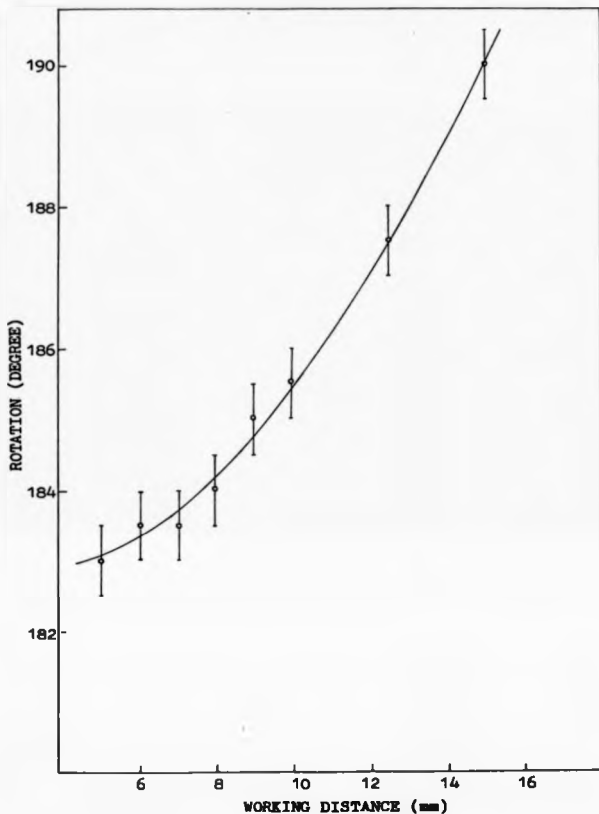


Figure 4.10 Relative rotation between s.a.c.p. and ordinary micrograph as a function of working distance at 30kV. Note that the relative rotation is in a clockwise sense.

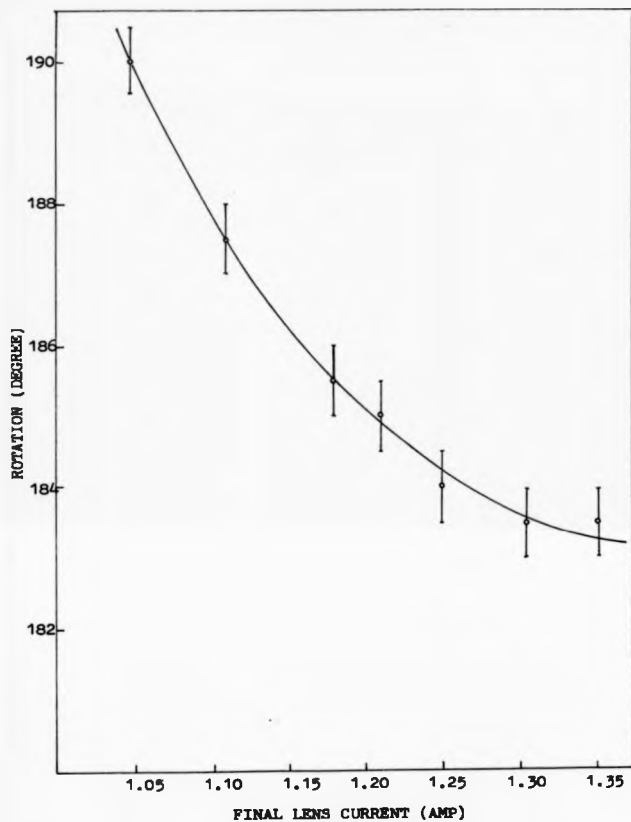


Figure 4.11 Relative rotation between s.a.c.p. and ordinary micrograph as a function of final lens current at 30kV. Note that the relative rotation is in a clockwise sense.

much variation of the amount of relative rotation between the two as a function of accelerating voltage for the same working distance was observed (i.e. less than  $2^\circ$ ) as shown in Fig. 4.12. Thus the results shown in Figs. 4.10 and 4.11 can also be used if s.a.c.p.'s are taken at different accelerating voltages; for example, if s.a.c.p.'s are taken at 20 kV or 40 kV instead of at 30 kV.

This rotation effect arises from the presence of stray fields in the back bore of the lens in the SEM. The ray paths traversed by the beam through this region are different in the s.a.c.p. and normal conditions. In general, it would be possible to correct this effect by <sup>a</sup>mechanical or electrical method. However, in practice it is simpler to calibrate and allow for the effect without correction at the source.

This relative rotation effect must be taken into account when accurate absolute orientation determinations are being made, or when crystallographic directions of the planes in the specimen are being found. However, when just orientations are being compared, as for example between two crystals in the same specimen, these effects cancel out.

#### 4.3.4 Complete orientation determinations

For many purposes, it is important to define a complete orientation of the crystals, particularly when twinning relationships or orientation relationships across a boundary are being investigated. This can be deduced from s.a.c.p.'s by the following method.

The method consists, in brief, of plotting on the stereographic

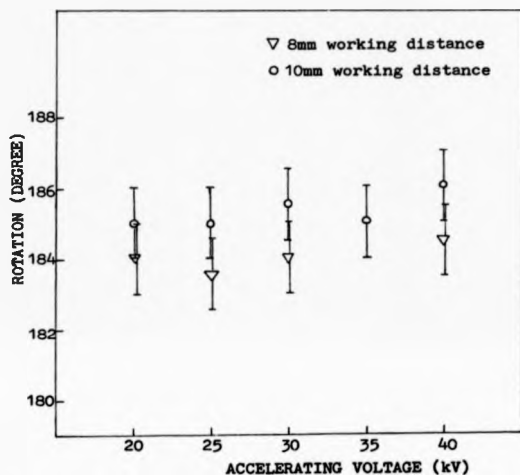
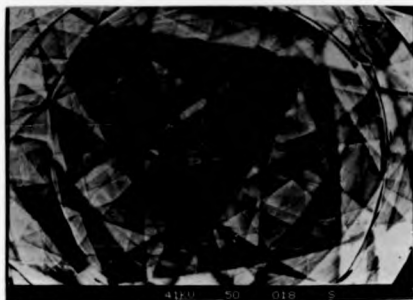


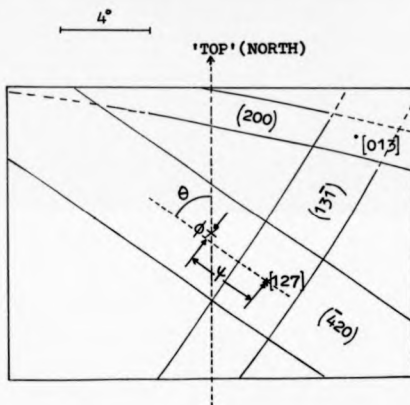
Figure 4.12 Relative rotation between s.a.c.p. and ordinary micrograph as a function of accelerating voltage for a given working distance. Note that the relative rotation is in a clockwise sense.



projection the zone axis of one band from the s.a.c.p. together with the pole defined by the crossing of this band with one or more additional bands. These two poles are then used to plot the positions of any other poles desired for the crystallographic analysis. Fig. 4.13 shows an example of the application of the method to a pattern taken from a copper specimen. The bands and poles on the pattern were identified and indexed by comparing with the appropriate unit triangle map. In order to transfer the chosen band and pole from the pattern on to the stereographic projection, it was necessary to locate the surface normal and to define one additional reference direction. The surface normal of an s.a.c.p. is just the position of the undeflected electron beam and corresponds to the centre of the pattern. This point was conveniently located from each sequence of the pattern by means of a perforated template cut to the shape of the pattern and it was always made to coincide with the centre of the stereographic net during the operation. The second reference direction selected for this operation was the vertical line running from the top to bottom through the centre of the pattern and corresponds to the North-South axis on the Wulff net. The appropriate angles and distances which define the positions of the chosen band and pole were measured relative to the reference directions defined above. For example, as shown in Fig. 4.13(b), the angles  $\phi$  and  $\psi$  are measured (to within  $\pm 0.2^\circ$ ) relative to the centre of the pattern, and the angle  $\theta$  (plus the rotation correction) is measured (to within  $\pm 1^\circ$ ) relative to the vertical line. The linear distances on the pattern were converted into angular values in degrees by using the appropriate calibration



(a)



(b)

**Figure 4.13** A complete orientation determination on copper showing: (a) s.c.p., and (b) the schematic drawing of some of the bands and poles in (a), the angles  $\theta$ ,  $\phi$  and  $\psi$  are defined in the text.

factor (which was determined from the pattern by using the index poles).

With the notation of Fig. 4.13(b), the  $[\bar{4}20]$  zone axis, which is normal to the  $(\bar{4}20)$  zone, is plotted  $90^\circ$  east of north and  $0^\circ$  (on a great circle) in from the perimeter. With the  $[\bar{4}20]$  pole set on the east-west axis (equator) of the Wulff net,  $[127]$  pole is located  $0^\circ$  west and  $90^\circ$  south of the origin. Any other desired directions which lie in the  $(\bar{4}20)$  zone, such as  $(001)$  and  $(122)$  can then be plotted at the appropriate angles from the  $[127]$  pole. Care must be taken to ensure that these poles are plotted in the correct direction from the  $[127]$  pole since this last operation defines the third direction necessary for the full description of the crystallographic orientation. Finally the other poles which are important for crystallographic analysis such as the  $\langle 100 \rangle$  directions can be inserted by using standard stereographic techniques. Fig. 4.14 shows the stereographic projection of the s.a.c.p. shown in Fig. 4.13(a) resulting from the operation described above. It should be recognised that the initial choice of the zones and poles for the operation was arbitrary, and any other combinations such as  $[1\bar{1}\bar{1}]$  and  $[127]$  may be used. The same result will be obtained to an accuracy set mainly by the cumulative error in plotting from the Wulff net as will be discussed in Section 4.5.

#### 4.4 Disorientation across a boundary

##### 4.4.1 Rotation matrix

Following Mykura (1980), the relative orientation between two

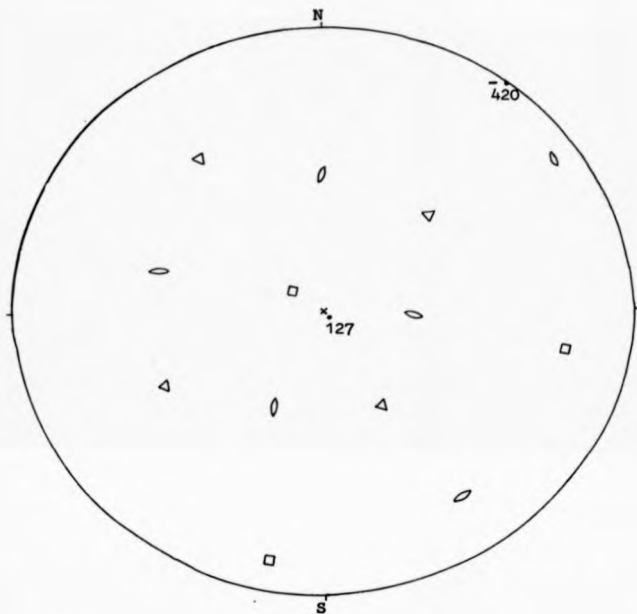


**Figure 4.14** The stereographic projection of the s.a.c.p. shown in Figure 4.13 (a).

crystals can be described by the rotation of one crystal which brings its crystal axes into parallelism with those of the other crystal. Three independent parameters are needed to define such a rotation. There are a number of different mathematical notations available for describing rotation (Lange 1967). Following Grimmer et al. (1974), the appropriate notation used in the present work to describe the orientation relationship between two adjacent grains is the rotation matrix.

For a given orientation relation, a 3 x 3 rotation matrix can be written as

$$R = \begin{pmatrix} A_{11} & A_{12} & A_{13} \\ A_{21} & A_{22} & A_{23} \\ A_{31} & A_{32} & A_{33} \end{pmatrix} \quad (4.6)$$

where the nine elements  $A_{ij}$  are column vectors of direction cosines between the cartesian axes in one grain and those in the other which can be measured as will be described later. The sums of the squares of each row and each column are unity. The dot products between column vectors are zero, so only three independent parameters are involved. By standard matrix procedures it is easily demonstrated that the rotation angle  $\theta$  is given by

$$\theta = \cos^{-1} \{ (A_{11} + A_{22} + A_{33} - 1) / 2 \} \quad (4.7)$$

and the direction of the rotation axis  $\langle hkl \rangle$  is given by

$$hkl = (A_{32} - A_{23}) : (A_{13} - A_{31}) : (A_{21} - A_{12}) \quad (4.8)$$

The relative orientation of two cubic crystals can be described

in 24 different ways, as the three cube axes are equivalent. By convention, right-handed coordinate systems are used and the right-handed screw direction outward along the rotation axis is the positive rotation direction. When the poles of 24 rotation axes are plotted onto the stereographic projection, then (in the absence of symmetry) one pole falls in each unit triangle. One of the 24 rotation axes will (in the absence of special symmetry) be associated with the smallest rotation angle  $\theta_{\min}$ . This angle-axis pair is usually chosen to describe the orientation relationships.

For C.S.L.'s of coincidence fraction  $\frac{1}{n}$ , the rotation matrix can be written as

$$R = \frac{1}{n} \sum \begin{pmatrix} a_{11} & a_{12} & a_{13} \\ a_{21} & a_{22} & a_{23} \\ a_{31} & a_{32} & a_{33} \end{pmatrix} \quad (4.9)$$

where  $a_{ij}$  are integers.

To check whether the disorientation between two crystals is a C.S.L. or not, the  $\langle 100 \rangle$  directions of one crystal are measured in the coordinate system of  $\langle 100 \rangle$  directions of the other crystal. These angular measurements can be done graphically as shown in Fig. 4.15 in which the direction cosines  $A_{ij}$  are measured along great circles of the Wulff net. These values are then written as column vectors in a  $3 \times 3$  matrix like Equation (4.6). Then, the rotation angle and the Miller indices of the rotation axis are computed using Equations 4.7 and 4.8 respectively. If the leading diagonal contains the three largest matrix elements, the angle-axis pair will be the one with the smallest rotation angle, otherwise it will be one of the other 23

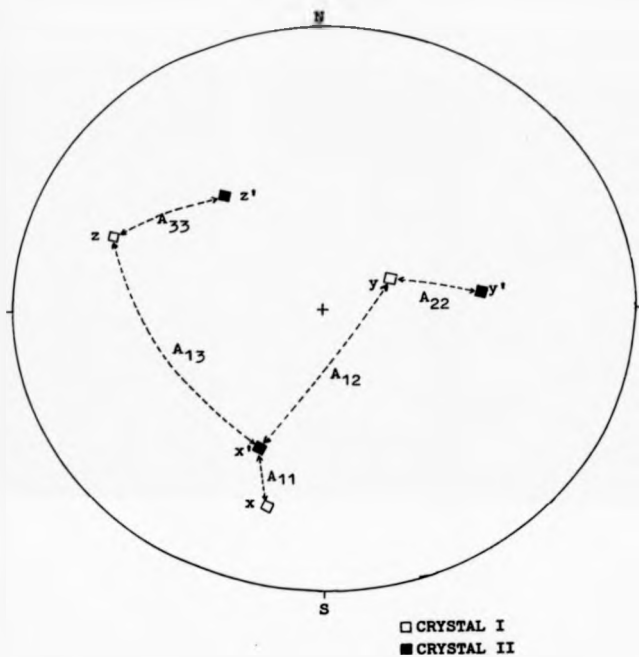


**Figure 4.13** Graphical measurements in the stereographic projection of the direction cosines  $A_{ij}$  between the  $\langle 100 \rangle$  directions of one crystal and the  $\langle 100 \rangle$  directions of the other crystal.

angle-axis pairs. If the latter is the case, the axes can be relabelled (i.e. the matrix permuted) in order to obtain the smallest angle and hence the angle-axis pair. Then by checking through the table due to Mykura (1980), the corresponding C.S.L. can be identified.

The axis and the angle of rotation through which a single rotation will cause orientation coincidence of the two grains can also be determined by graphical construction in the stereographic projection as shown in Fig. 4.16. This axis is defined by the intersection of the perpendicular bisectors of the angles between corresponding poles. The angle of rotation can then be measured as shown in the drawing.

#### 4.5 Accuracy of disorientation determination

The accuracy of disorientation determination using the method described in the previous section was found to be better than  $2^\circ$ . This discrepancy of up to  $2^\circ$  was attributable to several factors. Inaccuracy arose during the stereographic analysis, <sup>but</sup> with careful work using 20cm diameter projections, the cumulative errors should be not more than  $1^\circ$ . Electronic aberration leading to "barrel distortions" in the CRT display; such distortion can introduce uncertainties in orientation determination to 5% or more. The effects of this distortion were minimized by performing the stereographic analysis on bands and poles which were nearer to the centre of the s.a.c.p. image which suffered less distortion. In such a way, uncertainties in the angular direction of the bands was generally  $0.5^\circ$  or less, but in the



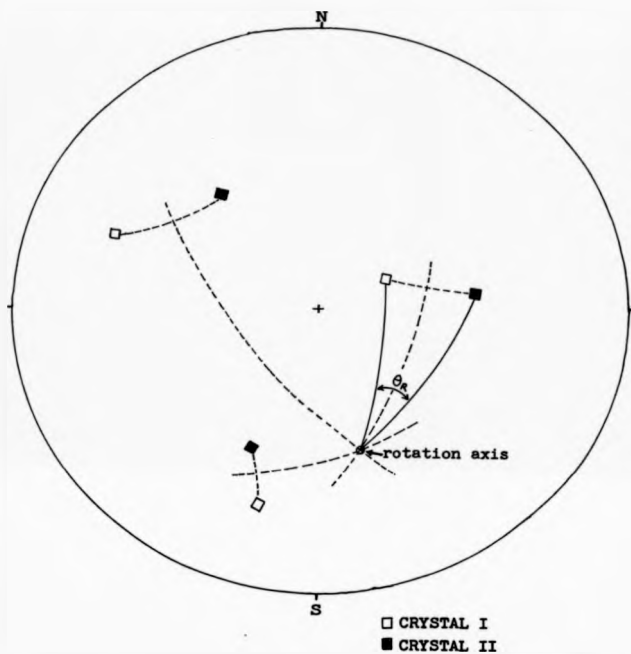


**Figure 4.16** Graphical construction in the stereographic projection of the axis about which a single rotation of angle  $\theta_R$  will cause coincidence of one crystal with the other.

case of more diffuse bands it was sometimes as much as  $1^\circ$ . In determining absolute orientation using s.a.c.p.'s, care should be exercised since there is, in general, relative rotation between s.a.c.p. and normal micrograph and this effect can amount to several degrees as described in Section 4.3.3. Careful measurement showed that in the present work, the error due to this effect was never greater than  $2^\circ$  and usually less than  $1^\circ$ .

CHAPTER 5: MEASUREMENT ON GRAIN BOUNDARIES IN "BAMBOO STRUCTURE"

COPPER WIRES

5.1 Experimental arrangements

5.1.1 Preparation of specimens

The copper wire used in this work was 99.99% nominal purity and of  $0.125 \pm 0.001$  mm in diameter, obtained from Goodfellow Metals Ltd. Two types of specimen arrangement were employed in order to study the crystal and grain boundary orientations. These are the horizontal and hanging wires.

The horizontal wire specimens were prepared by cutting the straightened wire into several lengths of approximately 30 mm and laying them horizontally on a graphite block (Fig. 5.1(a)). This block was then placed in a ceramic boat and annealed in a furnace at  $1000 \pm 5^\circ\text{C}$  in a dry 10%  $\text{H}_2$ : 90%  $\text{N}_2$  atmosphere surrounded by a copper sheet cover (in order to prevent net evaporation of the specimens). The furnace used was a split type tube furnace (manufactured by W. C. Heraeus GmbH) and the 10%  $\text{H}_2$ : 90%  $\text{N}_2$  gas was obtained from British Oxygen. In order to obtain a stable bamboo structure, the specimens were annealed for 70 - 200 hours.

The hanging wire specimens were prepared using the technique similar to the 'zero-creep' experiment. In this technique, a small box whose size was approximately 10 x 25 x 40 mm was made by folding a piece of the same nominal purity copper sheet. The wire was straightened and cut into several pieces approximately of the same length as the horizontal wire and hung through a small hole on top of

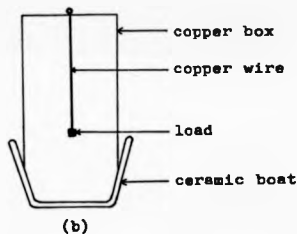
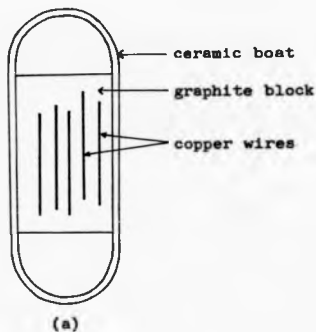


**Figure 5.1** Experimental set-up used for (a) horizontal wires (top view) and (b) hanging wires (side view) preparation. The systems were placed inside a furnace and annealed at 1000°C in a dry 10% H<sub>2</sub>: 90% N<sub>2</sub> atmosphere for 70-200 hours.

the box (Fig. 5.1(b)). A small weight  $W_0$ , made from a piece of copper sheet of the same nominal purity, was fixed to the bottom of the hanging wire in order to keep the wire straight. This box was then placed in a ceramic boat and annealed under the same conditions as the horizontal wire specimens.

The value of the tensile load  $W_0$  ( $\text{kg. m/sec}^2$ ) which would just counteract the tendency of the wire to reduce its surface area by shrinking was found using the simplified expression (Mykura 1966)

$$W_0 = \pi r \gamma_s \quad (5.1)$$

where  $r$  is the wire radius and  $\gamma_s$  is the specific surface energy of the solid. For the wire used in the present work, an approximate calculation gives  $W_0 \approx 10^{-3} \text{N}$ . Masses of 50 to 100  $\mu\text{g}$  were used.

### 5.1.2 Microscopy

The high temperature equilibrium shapes of the specimens were then "quenched-in" by cooling to room temperature. The specimens were then mounted for inspection in the SEM. It is assumed that the high temperature equilibrium shape is maintained during cooling for low temperature examination. The disorientation across a boundary was determined by using s.a.c.p.'s taken from adjacent individual grains in the specimen, as described in Chapter 4. The tilt angle  $\theta$  of the boundary plane was determined by the method described in the next section. The grain boundary groove profiles were measured from highly magnified micrographs (Fig. 5.2) taken by using a specimen holder, capable of rotating the specimen in the electron beam about the wire axis. With care using this method, the groove angles could be measured to within  $\pm 1^\circ$ .

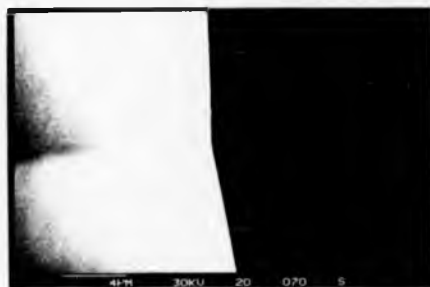


Figure 5.2 A typical SEM micrograph in backscattered mode of a grain boundary groove in copper annealed at 1000°C in a dry 10% H<sub>2</sub>: 90% N<sub>2</sub>

### 5.1.3 Tilt angle $\phi$ of boundary plane determinations

A typical grain boundary in a bamboo structure wire is assumed to be flat and of elliptical shape as shown schematically in Fig. 5.3. If  $A = \pi r^2$ , where  $r$  is the radius of the wire,  $A$  is the area of the boundary plane which is perpendicular to the wire axis (horizontal plane), then the area of a grain boundary plane which makes an angle  $\phi$  with the horizontal plane is given by

$$A_\phi = \frac{A}{\cos \phi} \quad (5.2)$$

The total grain boundary energy is therefore

$$E = \frac{\gamma_b A}{\cos \phi} \quad (5.3)$$

where  $\gamma_b$  is the specific grain boundary energy.

As the boundary is at an equilibrium position, the change in total grain boundary energy with a small increase in tilt angle  $d\phi$ , must be equal and opposite to the change in total grain boundary energy due to the accompanying increase in boundary area, that is

$$\frac{\partial E}{\partial \phi} = \frac{A}{\cos \phi} \left( \frac{\partial \gamma_b}{\partial \phi} \right)$$

hence

$$\frac{1}{\gamma_b} \left( \frac{\partial \gamma_b}{\partial \phi} \right) = -\tan \phi \quad (5.4)$$

This relation in fact has been derived by Hess (1952). The left hand side of the Equation (5.4) is the normalized torque term which

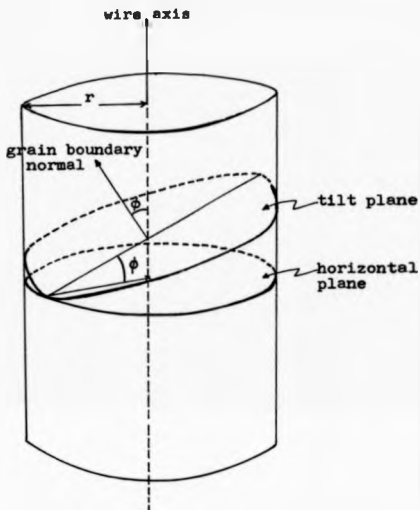


Figure 5.3 A schematic diagram of a "bamboo structure" wire defining the tilt angle  $\phi$ , the area of the horizontal plane  $A = \pi r^2$  and the area of the tilt plane which makes an angle  $\phi$  with the horizontal plane  $A_t = A/\cos\phi$  where  $r$  is the radius of the wire (ignoring the depth of the grain boundary groove).



can be determined simply by measuring the tilt angle  $\phi$  of boundary plane with respect to the wire axis in the following way. When the boundary is rotated so that the major axis is perpendicular to the line of view as shown schematically in Fig. 5.4(a), then it is easily seen that  $\tan \phi = \ell/D$ , where  $D$  is the diameter of the wire and  $\ell$  is the vertical distance as shown in the figure (neglecting the depth of the grain boundary groove). Neither  $\ell$  or  $D$  changes as the wire is rotated, so  $\tan \phi$  can easily be found for other boundary orientations. An example is shown in Fig. 5.4(b). In order to get a good value of  $\phi$ , the wires were photographed at  $0^\circ$  and  $\pm 60^\circ$ , which was achieved by rotating the specimen holder in the beam about the wire axis. In this way, the value of the normalized torque term could be determined to  $\pm 0.01$  in good conditions.

#### 5.1.4 Boundary type determinations

The pure tilt and twist boundaries are defined as described in Section 2.2.1. The general grain boundary with the axis of disorientation rotation of the two adjacent grains neither perpendicular nor parallel to the boundary plane has mixed tilt and twist character. The graphical method of determining the boundary type is illustrated in Fig. 5.5. The orientation of each crystal was determined using the method described in Section 4.3. The stereogram was constructed with the centre of the s.a.c.p. micrograph at the centre of the stereogram, and with the wire axis as the North-South axis of the stereogram. The rotation axis  $P$  was found using the method described in Section 4.4. The pole  $Q$ , which is the pole of the

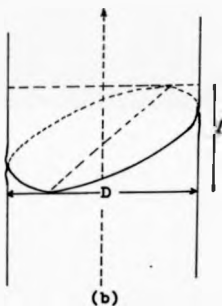
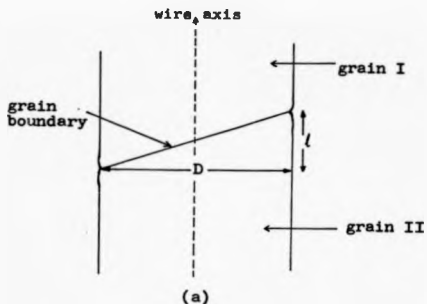


Figure 5.4 Normalized torque term determinations;  $\tan \phi = l/D$ , where  $l$  is the vertical distance and  $D$  is the diameter of the wire: (a) the boundary plane parallel to the line of view and (b) the boundary plane inclined with respect to the line of view (neglecting the depth of grain boundary groove).



boundary plane trace AB ( $90^\circ$  away), was plotted from measurements made on the geometry of the boundary plane, as described in the above section. By measuring the angle  $\alpha$  between the rotation axis P and the boundary plane trace AB along the great circle PQ, the boundary type can be found

$$\begin{aligned} \cos^2 \alpha & \text{ a tilt component} \\ \text{or} \quad \sin^2 \alpha & = 1 - \cos^2 \alpha \text{ a twist component} \quad (5.5) \end{aligned}$$

For a given orientation relationship between two adjacent crystals: if the rotation axis P is on the boundary plane trace AB (i.e.  $\alpha = 0$ ), then the boundary is a pure tilt; if the pole P coincides with the pole Q, then the boundary is a pure twist; whereas if the pole P is anywhere between the boundary plane trace AB and pole Q, then the boundary is of a mixed tilt and twist type. By using the graphical method described above, with care, the boundary type can be determined to an accuracy within  $\pm 5\%$ .

## 5.2 Results and discussion

### 5.2.1 Orientations and Herring torques measured

Of twenty-five grain boundaries (excluding  $\Sigma 3$  boundaries) which were fully analysed using horizontal wire specimens, three were found to separate adjacent crystals with low angle disorientation, one was  $\Sigma 19b$  and the others were random high angle boundaries.

Seventy-seven grain boundaries (excluding  $\Sigma 3$  boundaries) were fully analysed using hanging wire specimens. Sixteen were low angle boundaries. Twenty-seven were CSL boundaries of which five were  $\Sigma 11$ , three were  $\Sigma 25b$ , two each of  $\Sigma 27b$ ,  $\Sigma 33a$  and  $\Sigma 33c$  and one each of  $\Sigma 13b$ ,

$\angle 17a$ ,  $\angle 19a$ ,  $\angle 19b$ ,  $\angle 21a$ ,  $\angle 27a$ ,  $\angle 29a$ ,  $\angle 29b$ ,  $\angle 31a$ ,  $\angle 31b$ ,  $\angle 37a$ ,  $\angle 41b$  and  $\angle 45c$ .

As is generally accepted, the boundary was categorized as a low angle type when the rotation angle  $\theta$  was found to be less than  $15^\circ$ . The boundary was classified as special when the relative orientation between the two adjoining grains corresponded to any CSL orientation, within experimental error ( $\pm 2^\circ$ ) and when  $\angle \leq 45$  (i.e.  $\angle_{max}$ ). As explained in Section 2.2.3, the  $\angle_{max}$  was set because for high values of  $\angle$ , the rotation angles become so close to one another that it is difficult to distinguish between special and random boundaries. Consequently, the boundaries which were found to be not in the above range were classified as random high angle boundaries.

The much lower frequency of low angle and CSL boundaries found in horizontal specimens than in hanging specimens was expected. This is probably due to the fact that crystals in horizontal wires are not free to rotate into positions of minimum energy because they are constrained by the graphite block used during the annealing treatment, thus resulting in random boundaries. Crystals in hanging wires are quite free to rotate about the vertical axis when the boundary is perpendicular to that axis (Pond and Smith (1977) mechanism), but much less able to rotate about the two horizontal axes (Shewmon (1966) mechanism) as it requires diffusional mass transport and introduces gravitational torques (see Section 5.2.2.) to reach equilibrium conditions.

The distribution of the normalized (Herring) torque terms measured from grain boundaries in horizontal wires is shown in Fig.

5.6(a) and from boundaries in hanging wires in Fig. 5.6(b). The mean value of the normalized torque term in horizontal wires was  $0.19 \pm 0.03 \text{ rad}^{-1}$  and in hanging wires was  $0.24 \pm 0.03 \text{ rad}^{-1}$ . However, it can be seen that, in general, the CSL and low angle boundaries are associated with high values of torque, whereas random high angle boundaries with low values of torque. Table 1 contains full details of typical examples of grain boundaries analysed from both kinds of specimens. The details of  $\Sigma 11$  and  $\Sigma 25b$  boundaries are listed in Table 2 and Table 3 respectively.

One of the  $\Sigma 25b$  boundaries (No. 1 in Table 3) was found to incline at  $46.6^\circ \pm 1.5^\circ$  to the wire axis which has the highest torque measured, except for  $\Sigma 3$  boundaries. The orientation of this boundary is shown in Fig. 5.7. The other two boundaries have high torques too, but the third one was  $18^\circ \pm 2^\circ$  from the (543) mirror plane (see Table 3). Of all boundaries analysed in both kinds of specimen, 18% were found to rotate toward their mirror planes ( $<20^\circ$ ), 13% were found to incline more than  $20^\circ$  to the wire axis. Only 15% of all boundaries analysed were found to be pure tilt and 4% were pure twist type (within  $\pm 5\%$  experimental error), most of them were mixed tilt and twist boundaries with a larger tilt component. This result in fact is to be expected for randomly oriented crystals in polycrystalline specimens.

One of the most interesting results of this analysis is that the  $\Sigma 11$  boundaries were found to be of significant lower energies than other special boundaries, except for the coherent twin ( $\Sigma 3$ ) boundaries. A detailed analysis of these boundaries will be given in

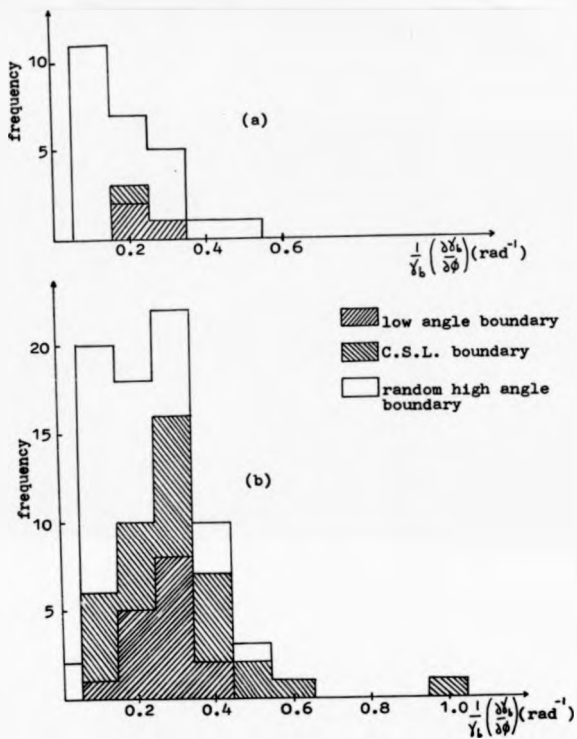


**Figure 5.6** Distribution of normalized torque terms measured in, (a) horizontal wires and (b) hanging copper wires, annealed at 1000°C in a dry 10% H<sub>2</sub>: 90% N<sub>2</sub>.

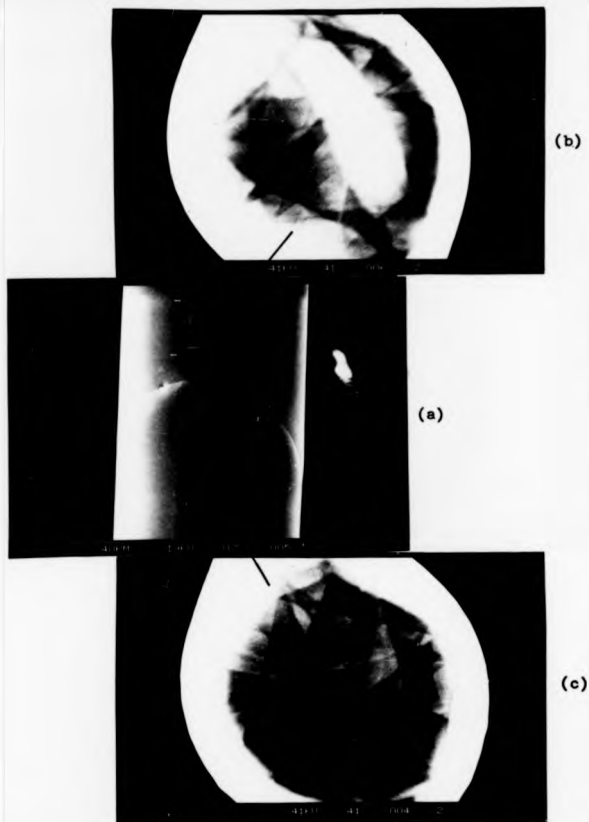


**Figure 5.7** The highest measured torque term in "hanging" copper wire annealed at 1000°C: (a) micrograph, (b) and (c) s.a.c.p.'s of the two grain, and (d) the orientation showing to be  $\Sigma 25b$ .



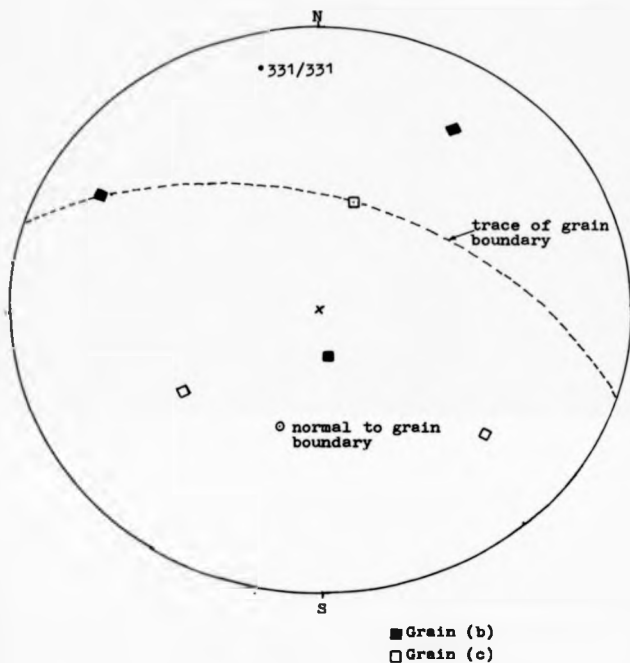


Figure 5.7(d)

TABLE 1  
Details of 10 typical boundaries measured in copper wires

| No. | Boundary | Disorientation                                    | $\frac{1}{\gamma_b} \frac{\partial \gamma_b}{\partial \phi}$ (rad <sup>-1</sup> ) | $\frac{\gamma_b}{\gamma_s}$ | Boundary type                |
|-----|----------|---|---|-----------------------------|------------------------------|
| 1   | E17a     | $27.3^\circ \pm 1^\circ$ on $\langle 100 \rangle$ | $0.17 \pm 0.02$   | $0.32 \pm 0.01$             | $60^\circ \pm 5^\circ$ tilt  |
| 2   | E19b     | $46.5^\circ \pm 1^\circ$ on $\langle 111 \rangle$ | $0.23 \pm 0.02$   | $0.30 \pm 0.01$             | $90^\circ \pm 5^\circ$ tilt  |
| 3   | E31b     | $51.7^\circ \pm 1^\circ$ on $\langle 211 \rangle$ | $0.26 \pm 0.02$   | $0.30 \pm 0.01$             | $80^\circ \pm 5^\circ$ twist |
| 4   | E33c     | $56.0^\circ \pm 1^\circ$ on $\langle 110 \rangle$ | $0.15 \pm 0.03$   | $0.28 \pm 0.01$             | $80^\circ \pm 5^\circ$ tilt  |
| 5   | LAB      | $11.0^\circ \pm 1^\circ$ on $\langle 211 \rangle$ | $0.25 \pm 0.03$   | $0.19 \pm 0.01$             | $90^\circ \pm 5^\circ$ twist |
| 6   | LAB      | $5.5^\circ \pm 1^\circ$ on $\langle 110 \rangle$  | $0.31 \pm 0.02$   | $0.12 \pm 0.01$             | $75^\circ \pm 5^\circ$ tilt  |
| 7   | LAB      | $8.0^\circ \pm 1^\circ$ on $\langle 331 \rangle$  | $0.28 \pm 0.02$   | $0.19 \pm 0.01$             | $80^\circ \pm 5^\circ$ tilt  |
| 8   | RHAB     | $52.4^\circ \pm 1^\circ$ on $\langle 544 \rangle$ | $0.09 \pm 0.02$   | $0.35 \pm 0.01$             | $70^\circ \pm 5^\circ$ twist |
| 9   | RHAB     | $49.0^\circ \pm 1^\circ$ on $\langle 441 \rangle$ | $0.12 \pm 0.03$   | $0.33 \pm 0.01$             | $80^\circ \pm 5^\circ$ tilt  |
| 10  | RHAB     | $44.5^\circ \pm 1^\circ$ on $\langle 533 \rangle$ | $0.09 \pm 0.02$   | $0.35 \pm 0.01$             | $55^\circ \pm 5^\circ$ tilt  |

LAB = Low angle boundary

RHAB = Random high angle boundary

TABLE 2

Details of I11 boundaries

(Actual disorientation: 50.48° on &lt;110&gt;)

| No. | Disorientation         | $\frac{1}{\gamma_b} \left( \frac{\partial \gamma_b}{\partial \theta} \right) (\text{rad}^{-1})$ | $\gamma_b / \gamma_s$ | Boundary type | Boundary position   |
|-----|------------------------|---|-----------------------|---------------|---|
| 1   | 50.0° ± 1°<br>on <110> | 0.32 ± 0.02   | 0.24 ± 0.01           | 95% ± 5% tilt | 12° ± 2° to <311><br>80° ± 2° to <332><br>85° ± 2° to <110> |
| 2   | 51.2° ± 1°<br>on <110> | 0.25 ± 0.02   | 0.25 ± 0.01           | 90% ± 5% tilt | 18° ± 2° to <311><br>72° ± 2° to <332><br>82° ± 2° to <110> |
| 3   | 50.6° ± 1°<br>on <110> | 0.42 ± 0.03   | 0.24 ± 0.01           | 95% ± 5% tilt | 6° ± 2° to <311><br>89° ± 2° to <332><br>85° ± 2° to <110>  |
| 4   | 49.8° ± 1°<br>on <110> | 0.40 ± 0.02   | 0.26 ± 0.01           | 95% ± 5% tilt | 10° ± 2° to <311><br>81° ± 2° to <332><br>84° ± 2° to <110> |
| 5   | 50.5° ± 1°<br>on <110> | 0.29 ± 0.02   | 0.25 ± 0.01           | 95% ± 5% tilt | 83° ± 2° to <311><br>8° ± 2° to <332><br>86° ± 2° to <110>  |

TABLE 3

Details of 125b boundaries  
(Actual disorientation:  $51.68^\circ$  on  $\langle 331 \rangle$ )

| No. | Disorientation                                       | $\frac{1}{Y_D} \left( \frac{\delta Y_D}{\delta \theta} \right) (\text{rad}^{-1})$ | $Y_D / r_s$     | Boundary type       | Boundary position  |
|-----|--|---|-----------------|---------------------|--|
| 1   | $50.5^\circ \pm 1^\circ$<br>on $\langle 331 \rangle$ | $1.06 \pm 0.03$   | $0.29 \pm 0.01$ | $65\% \pm 5\%$ tilt | on $\langle 530 \rangle \pm 2^\circ$<br>$90^\circ \pm 2^\circ$ to $\langle 543 \rangle$<br>$57^\circ \pm 2^\circ$ to $\langle 331 \rangle$           |
| 2   | $50.8^\circ \pm 1^\circ$<br>on $\langle 331 \rangle$ | $0.50 \pm 0.02$   | $0.31 \pm 0.01$ | $45\% \pm 5\%$ tilt | $9^\circ \pm 2^\circ$ to $\langle 751 \rangle$<br>$86^\circ \pm 2^\circ$ to $\langle 543 \rangle$<br>$40^\circ \pm 2^\circ$ to $\langle 331 \rangle$ |
| 3   | $52.2^\circ \pm 1^\circ$<br>on $\langle 331 \rangle$ | $0.55 \pm 0.02$   | $0.29 \pm 0.01$ | $85\% \pm 5\%$ tilt | $18^\circ \pm 2^\circ$ to $\langle 543 \rangle$<br>$77^\circ \pm 2^\circ$ to $\langle 331 \rangle$   |

the next section. The commonest of coherent twin ( $\Sigma 3$ ) boundaries in f.c.c. metals is well known. This type of boundary was studied in copper sheet specimens as will be discussed in Chapter 6. Nine boundaries were found to be multiply twinned. Of the higher CSL boundaries listed above, the  $\Sigma 45c$  is twin-related to  $\Sigma 15$ ,  $\Sigma 33a$  and  $\Sigma 33c$  are twins of  $\Sigma 11$ ,  $\Sigma 27a$  and  $\Sigma 27b$  are twins of  $\Sigma 9$ , and  $\Sigma 21a$  is a twin of  $\Sigma 7$ . This property can be checked graphically or analytically by using a rotation matrix (see Section 4.4.1).

The distribution of the ratio of grain boundary energy to surface energy,  $\gamma_{gb}/\gamma_s$ , for all boundaries analysed using horizontal and hanging wires is shown in Figs. 5.8(a) and 5.8(b) respectively. These values were computed using Equation (3.2). These evaluations obviously only give approximate values since both  $\gamma_{gb}$  and  $\gamma_s$  were assumed to be isotropic. Measurements of the anisotropy of  $\gamma_s$  in nickel at 1000°C (Mykura 1961) show that this anisotropy can be as great as 8% and that surface torques approach  $0.3 \text{ rad}^{-1}$  at low index orientations. Even for more general surface orientations with relatively low surface energy, the surface torques can be appreciable in magnitude; for surface orientations having slightly less than 1% anisotropy in  $\gamma_s$  still give rise to torques of  $0.05 \text{ rad}^{-1}$ . Although these are the results for nickel, the results for copper <sup>also</sup> in fact very similar. However, for a large number of random boundaries, the surface torques are equally likely to be positive or negative and therefore should not affect the average value of a large number of  $\gamma_{gb}/\gamma_s$  ratio measurements, provided that there is no marked preferred orientation in the specimen used. The grain boundary torque makes no

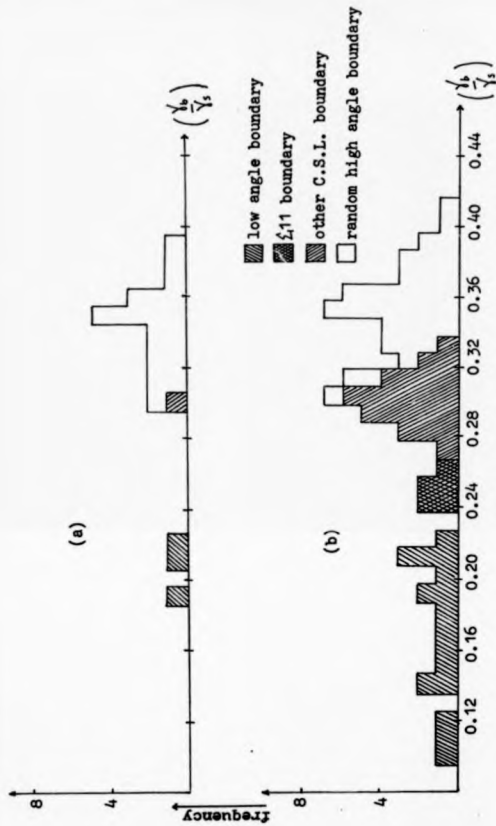


Figure 5.8 Distribution of the ratio of grain boundary energy to surface energy measured from (a) horizontal and (b) hanging wires of copper annealed at 100°C.

contribution to the equilibrium groove shape and hence the ratio of  $\gamma/\gamma_0$  and provided that the grain boundary is perpendicular to the specimen surface. However, when the grain boundary is inclined with respect to the surface, as frequently observed in the present work, the grain boundary torque will then contribute some significant effect to the value of  $\gamma/\gamma_0$ . Nevertheless the values of  $\gamma/\gamma_0$  ratio shown in the two histograms (Fig. 5.8) give some valuable information on grain boundary energies of low angle, CSL and high angle boundaries.

It has been stated that if the grain boundary grooves formed in the wires are not opposite to each other, the grain boundaries have not yet been equilibrated (Ahmad and Murr 1975). They also said that, normally, when the grain boundaries achieve equilibrium, they will become normal to the surface and grooves formed in the wire also become parallel and opposite to each other. This argument in fact is untrue since our result shows that the lower energy boundaries were inclined at angles given by the Hoss equation (Equation 5.4) to the surface of the wire after 70-200 hours annealing.

It has been shown that there is considerable experimental evidence for special boundaries retaining their ordered relatively low energy structures at the disorientations deviating slightly from the exact CSL orientations (Pumphrey 1976). Several criteria for estimating the maximum deviation at which a boundary remains special have been proposed and adopted. One of the most commonly used is the Brandon criterion (Brandon 1966) for which the maximum deviation is specified by

$$\Delta\theta = 15^\circ (\bar{L})^{-\frac{1}{2}} \quad (5.6)$$

In general, his criterion is based on the dislocation core overlapping in small angle boundaries where dislocations in the boundary come closer to each other with an increasing disorientation. Any such criterion is difficult to check experimentally as it is difficult to prepare specimens (bicrystals in particular) with predetermined deviations from special disorientations. Consequently, the characterization of the specialness of a grain boundary using the Brandon criterion is in question since it can lead to misinterpreted results. The value of the maximum deviation given by Equation (5.6) for  $\delta = 1, 3, 17$  and  $25$  is  $15^\circ, -4^\circ, -3.5^\circ$  and  $3^\circ$  respectively. For our purposes, the Brandon criterion is thus not appropriate since we are only interested in the exact CSL orientation.

#### 5.2.1.1 Detailed analysis of $\Sigma 11$ boundaries

There exists a  $\bar{V}$ -plot for a grain boundary between two adjacent crystals of fixed crystal disorientation. The symmetry of the  $\bar{V}$ -plot must be the same as the CSL symmetry. Thus for the  $\Sigma 11$ , the symmetry of CSL unit cell is orthorhombic (Grimmer et al. 1974, Vlachavas 1985), for which the three mutually perpendicular symmetry planes are, for example,  $(01\bar{1})$ ,  $(311)$  and  $(\bar{2}33)$ .

Of five  $\Sigma 11$  boundaries found, four were within  $6^\circ$ - $18^\circ$  to the  $(311)$  mirror plane and one was  $8^\circ \pm 2^\circ$  to the  $(322)$  mirror plane (see Table 2). The orientation of one of the  $\Sigma 11$  boundaries near the  $(311)$  mirror plane (no. 1 in Table 2) is shown in Fig. 5.9. The values of the torque term of  $\Sigma 11$  boundaries near  $(311)$  are shown in Fig. 5.10 and the grain boundary energy anisotropy obtained (by graphical integra-



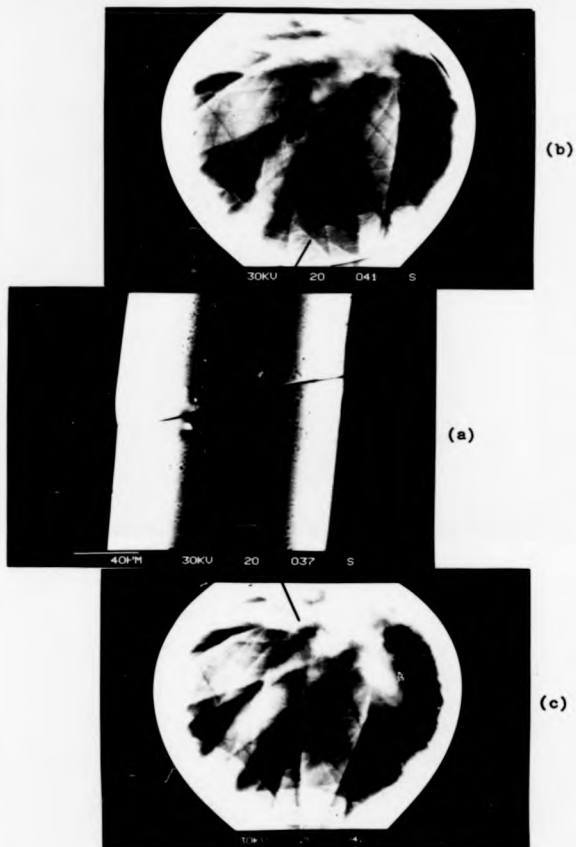


**Figure 5.9** A typical grain boundary in "bamboo structure" copper wire annealed at 1000°C: (a) micrograph, (b) and (c) s.a.c.p.'s of the two grains and (d) the orientation shown to be  $\{111\}$ .

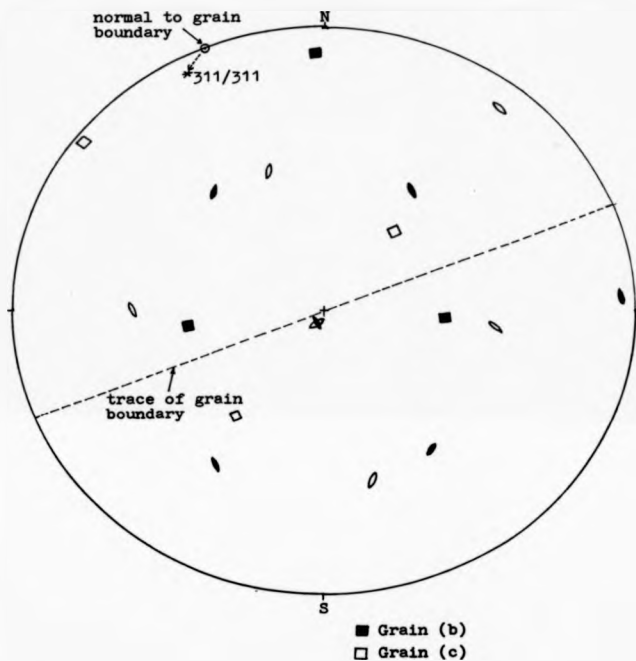
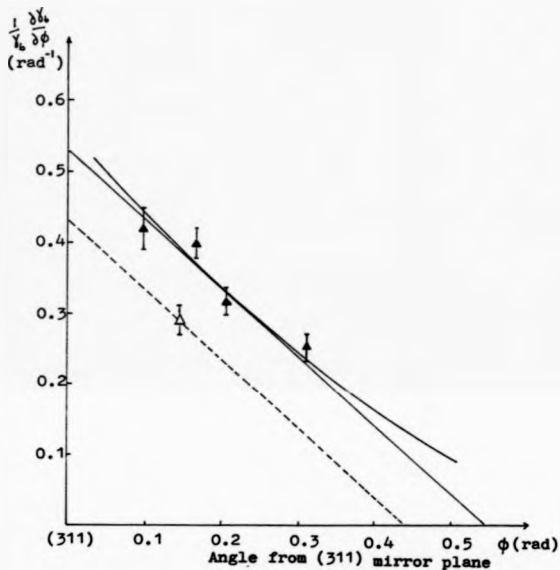


Figure 5.9(d)



**Figure 5.10** Torque terms  $\frac{1}{6} \left( \frac{\delta\delta}{\delta\phi} \right)$  for  $\bar{L}_{11}$  boundaries in copper near (311) mirror plane. The area under the solid line from zero to  $\phi$  is equal to the difference in grain boundary energy of a boundary at angle  $\phi$  from (311) and a (311) boundary. The torque term for  $\bar{L}_{11}$  boundary  $8^\circ$  from (311) mirror plane is marked by an open triangle. The area under the broken line gives the difference in energy at (311) orientation from those boundaries angle  $\phi$  away from that orientation.

tion] from this torque term curve is shown in Fig. 5.11(a). It can be seen that the energy of the  $\Sigma_{11}$  boundary at the (311) plane is  $15\% \pm 2\%$  lower than the  $\Sigma_{11}$  boundary energies away from the mirror plane. No accurate variation of the torque term and grain boundary energy anisotropy near (332) and (110) can be deduced because of the lack of data. If the broken line drawn through the one available point near the (332) mirror plane, as shown in Fig. 5.10, is used to fit a torque term graph for  $\Sigma_{11}$  boundaries centred on <sup>the</sup> (332) orientation, then the energy of  $\Sigma_{11}$  boundary at this mirror plane (obtained by graphical integration) is  $10\% \pm 3\%$  lower than the energies of  $\Sigma_{11}$  boundaries away from it (Fig. 5.11'(b)). There is evidence from the sphere sintering experiments that the energy of  $\Sigma_{11}$  boundary centred on (110) orientation is also minimum (Mykura 1979). The (110) section through the  $\gamma$ -plot for  $\Sigma_{11}$  boundary is shown in Fig. 5.12.

In the above analysis, the simplifying assumption was made that ~~the~~ torque term near <sup>the</sup> (311) orientation was due to the conical cusp in the  $\gamma$ -plot centred on this low index orientation. In some cases the assumption of conical cusps centred on low index orientations would be quite valid. In other cases, however, it would lead to an error of about 30% at some other orientations.

A  $\Sigma_{11}$  boundary has been reported to be a low energy boundary in copper (McLean 1973) and in aluminium (Hasson and Goux 1971). Our result for the boundary of the same type in copper annealed at 1000°C agrees quite well with the above observations.

## 5.2.2 'Winking' in wires

Some parts of the bamboo structure in hanging wires were found

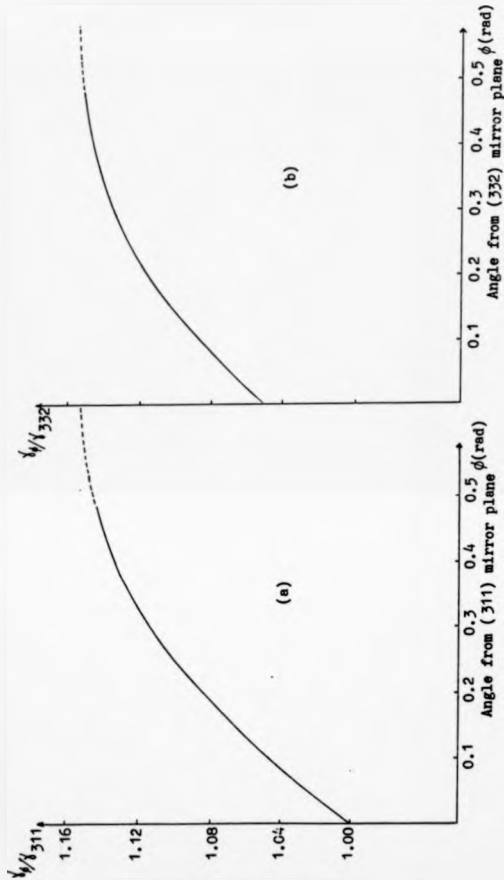
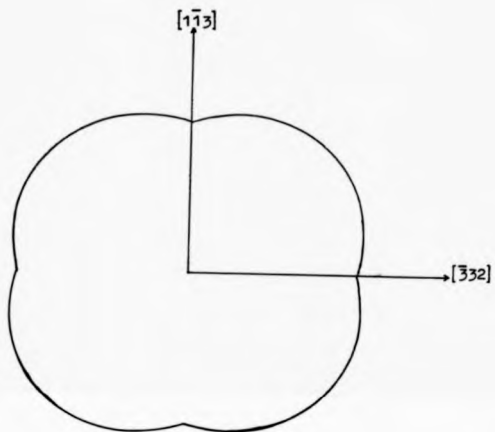


Figure 5.11 Grain boundary energy anisotropy for  $\Sigma 11$  boundaries

centred on (a) (311) mirror plane, and (b) (332) mirror plane,

obtained by integration of Figure 5.10.



**Figure 5.12** An (110) section through the  $\gamma$ -plot for the  $\Sigma_{11}$  boundary. Scale:  $10\text{mm} = 89 \text{ mJm}^{-2}$ , evaluated from  $\gamma_s = 1.78 \text{ Jm}^{-2}$  (Murr 1972) and  $\gamma_{\Sigma_{11}}/\gamma_s = 0.25$  (from Table 2).

to show 'kinking' at some boundaries as can be seen in Fig. 5.13(a). The occurrence of this geometry can, in principle, be explained in terms of the Shewmon torque terms (Shewmon 1966) and the gravitational torque (Mykura and Gleiter 1979).

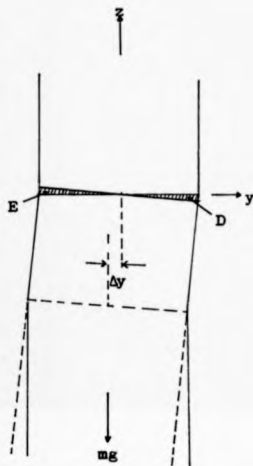
We take a Cartesian coordinate system with x and y axes in the boundary plane (taken to be normal to the specimen surface) and z axis perpendicular to this plane (Fig. 5.13(b)). The Shewmon torque term of magnitude  $A \frac{\partial \gamma}{\partial \theta_i}$ , (where A is the grain boundary area and  $\theta_i$  specifies the rotation of the crystal about the x axis) acts about the x axis and drives the crystal rotation about this axis by the Shewmon mechanism. This mechanism involves the net diffusive motion of a wedge of material from D to E and introduces a gravitational torque  $mg\Delta y$  (taking mg to act in the z direction), where m is the mass of the wire below the boundary, g the acceleration due to gravity and  $\Delta y$  the displacement between the centre of the 'top' and 'bottom' boundaries (Fig. 5.13(b)). The Shewmon torque will continue to act on the crystal and causes it to rotate until it becomes equal to gravitational torque, that is

$$A \frac{\partial \gamma}{\partial \theta_i} = mg\Delta y \quad (5.7)$$

If the Shewmon torque  $A \frac{\partial \gamma}{\partial \theta_i}$  at the 'bottom' boundary is zero, then because there is the weight of the bottom wire, the wire will tend to straighten back due to the gravitational torque which thus results in 'kinking'.



(a)



(b)

**Figure 5.13** (a) SEM micrograph of copper wire showing "kinking" at grain boundaries. (b) The terms used to define the Shewmon mechanism and gravitational torques.



### 5.2.3 Grain boundary sliding

Grain boundary sliding is the relative displacement of crystals along grain boundaries. This form of motion was found to occur at some boundaries in copper wires studied. When the weight at the bottom of the wire is less than that required for the 'zero-creep' condition, then the wire can shorten itself by sliding up an inclined boundary (Fig. 5.14). This is energetically favourable as the decrease in (surface area  $\times \gamma_s$ ) is greater than the work done against gravity.

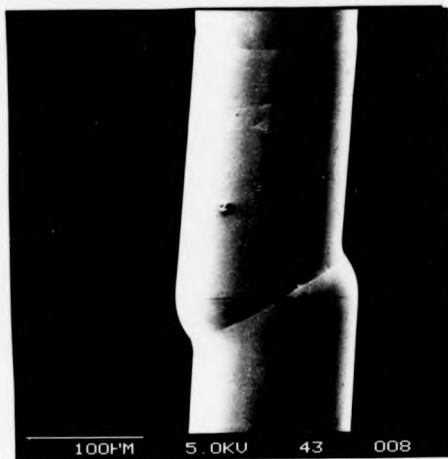


Figure 5.14 SEM micrograph of copper wire showing an "upward" sliding.

## CHAPTER 6: MEASUREMENT OF SPECIAL BOUNDARIES IN COPPER SHEETS

A number of models have been proposed to explain the formation of annealing twins in f.c.c. metals (e.g. Kopecky et al. 1985). In the present work,  $\Sigma 3$  (coherent and incoherent) and  $\Sigma 9$  boundaries in copper sheet at 1000°C were investigated. The results of measurements of Herring torque terms of these boundaries are discussed here. Their  $\gamma$ -plots have been investigated. The criterion for the break-up of  $\Sigma 9$  boundary into two  $\Sigma 3$  boundaries has been examined. The morphology of a  $\Sigma 9$  boundary constrained by coherent twin  $\Sigma 3$  boundaries was also studied. The  $\Sigma 9$  rotation matrix is equal to the product of two  $\Sigma 3$  rotation matrices. The CSL unit cell for  $\Sigma 3$  is hexagonal, and for  $\Sigma 9$  is orthorhombic (Grimmer et al. 1974).

### 6.1 Experimental arrangements

#### 6.1.1 Specimens preparation

The experiments were performed by using 99.99% nominal purity copper sheet of 0.05mm and 0.10mm thick, obtained from Goodfellow Metals Ltd. The effect of impurity was also studied. For this purpose, 0.1mm thick copper sheet 99.999% nominal purity, obtained from the same manufacturer, was also used. The sheet materials were cut into specimens of about 5mm x 10mm. In order to determine the inclination of boundary plane much more easily, by the method described in section 6.1.3, the edges of specimens were marked using a razor blade. The specimens were then flattened and annealed under the same conditions as the wire specimen (see Section 5.1.1), supported in

an alumina crucible with a lid of the specimen material to prevent net evaporation.

#### 6.1.2 Microscopy

There is no difficulty in cooling the specimens rapidly enough so that the high temperature equilibrium shape is retained for measurement at room temperature. The specimens were examined optically and in a SEM. The disorientation between adjacent grains was determined using s.e.c.p.'s taken from each grain as described in Chapter 4. In certain cases, the disorientation was obtained by the twin-trace technique (Mykura 1958). The grain boundary groove profiles and dihedral angles were evaluated from enlarged prints taken by using a Baker interference microscope (Hodgson 1972). The wedge angles were measured to an accuracy of better than  $\pm 10\%$ .

#### 6.1.3 Tilt angle $\phi$ of boundary plane determinations

When a  $\Sigma 3$  twin has an incoherent boundary (as at B in Figure 6.1(a)), then the area perpendicular to the coherent boundary  $A_1A_2$  and the specimen surface is the minimum area for the incoherent boundary. If this surface is not the local minimum energy interface for the incoherent  $\Sigma 3$  boundary, then it will rotate due to the Herring torque terms. The Hess relation (Equation 5.4) will apply, as the two coherent boundaries are at a fixed separation and the specimen thickness is fixed. The normalized (Herring) torque term could then be determined simply by measuring the tilt angle  $\phi$  of the boundary plane as described below. In order to make measurements easier, almost all

boundaries chosen for investigation were near to the specimen edge. By matching the edge of the specimen from photographs taken on both sides of the specimen surface, the distance  $d$  between <sup>the</sup> boundary trace on the front surface and the projection of the trace of the same boundary on the back surface of the specimen (Figure 6.1(b)) could then be measured. The specimen thickness  $t$  is already known. So the inclination angle  $\phi$  between the boundary plane and the specimen surface could then be evaluated from the expression

$$\tan \phi = \frac{t}{d} \quad (6.1)$$

When the interesting boundary was quite far away from the edge of the specimen, it was difficult to photograph it and the specimen edge together. However, the inclination of the boundary could still be determined provided that the directions of <sup>the</sup>  $L_3$  {111} plane normals were known (from the orientation of that grain which was obtained by using s.a.c.p.).

With care, using the method described above, the tilt angle  $\phi$  of <sup>the</sup> boundary plane could be determined to an accuracy better than  $\pm 1^\circ$ .

## 6.2 Condition for a boundary (like B in Figure 6.1(a)) not to migrate

The various possible driving pressures for grain boundary migration have been discussed by Stuve (1978). If two crystals have different free energies, then the boundary separating them will move in a direction which will increase the size of the lower energy crystal. The movement of the grain boundary occurs by a diffusional



(a)

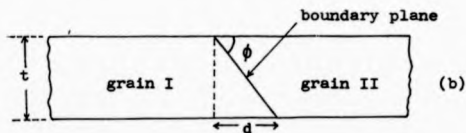
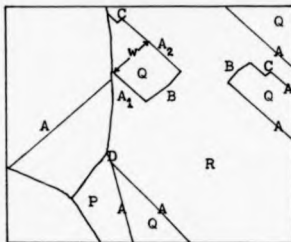


**Figure 6.1** (a) SEM micrograph of a polycrystalline copper sheet annealed at 1000°C showing: A = coherent  $\Sigma 3$  {111} planes, B = incoherent twin boundary at the end of A, C = step of incoherent twin boundary along the side of A, and D =  $\Sigma 9$  boundary; (b) A schematic section of the sheet defining the terms used for the determination of boundary inclination.

motion of atoms across the boundary.

The  $\Sigma_3$  twin band which runs across a grain can be regarded as being a stable configuration, as both their ends are anchored. When a  $\Sigma_3$  twin band ends within a grain (as at B in Figure 6.1(a)), the condition whether such a boundary may migrate or not is given by the balance force equation which can be written as (ignoring the torque terms for a moment)

$$2(\gamma_{s_Q} - \gamma_{s_R})w + 2\gamma_t \left( \frac{t}{\sin \phi} \right) = F_{\text{TOTAL}} \quad (6.2)$$

where  $\gamma_{s_Q}$  and  $\gamma_{s_R}$  are the surface energies of grain Q and grain R,  $\gamma_t$  is the energy of  $\Sigma_3$  coherent twin boundary,  $w$  is the width of the twin band  $A_1A_2$  and  $t$  is the specimen thickness. The value of  $\gamma_t$  is well known to be very small ( $\frac{\gamma_t}{\gamma_s} \approx 0.01$  (Robertson and Shewmon 1962)). If the total force  $F_{\text{TOTAL}}$  is equal to zero, then the boundary will not move. The effective pressure across the end of the grain (boundary B) is  $F/A$ , where  $A$  is the area of the boundary plane. If this pressure is sufficiently small, then boundary B can be regarded as being stationary.

The  $\Sigma_3$  twin Q that ends within a grain may disappear during annealing by migration of the incoherent boundary at its end (boundary B). This may occur if the width  $w$  of the band  $A_1A_2$  is much smaller than the specimen thickness  $t$ , so  $\gamma_t$  will dominate and the boundary will migrate. The condition for the local stability of the steps of incoherent twin boundary along the side of coherent  $\Sigma_3$  twin boundaries (as at C in Figure 6.1(a)) is given by the surface energy term in Equation (6.2).

### 6.3 $\Sigma 3$ boundaries

#### 6.3.1 Results and discussion

The  $\Sigma 3$  twin boundaries selected for investigation were those which appeared on both sides of the specimen surface. They were assumed to be stationary. It is also assumed that the boundary plane is a flat interface.

Twenty-seven  $\Sigma 3$  twin boundaries which have incoherent twin boundaries at the end of coherent  $\Sigma 3$  twin boundaries were analysed. Of these boundaries, sixteen were measured from 0.10mm thick copper sheet of 99.99% nominal purity, five were measured from 0.05mm thick copper sheet of the same nominal purity, and the rest were measured from 0.10mm thick copper sheet of 99.999% nominal purity.

The incoherent twin boundaries at the end of coherent  $\Sigma 3$  twin boundaries were usually observed to facet into two segments (see Figure 6.2). Figure 6.3 shows the orientation of one of the  $\Sigma 3$  twin boundaries appearing in Figure 6.2. The orientations of the two segments of incoherent twin boundary (lettered X and Y) are also shown. The full details of 8 typical groups of incoherent  $\Sigma 3$  twin boundaries are listed in Table 4.

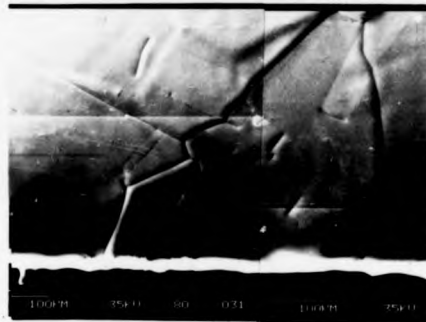
If it is assumed that the incoherent  $\Sigma 3$  boundary is in the minimum area orientation (i.e. perpendicular to the specimen surface and to the coherent {111} planes), then the orientation of the incoherent boundary, as deduced from the crystal orientation, would be as shown in Figures 6.4 and 6.5. These boundaries were found not to be in the minimum area orientation, as they were observed to facet and to be inclined at angles which we assume are given by the Hess relation (Equation 5.4).



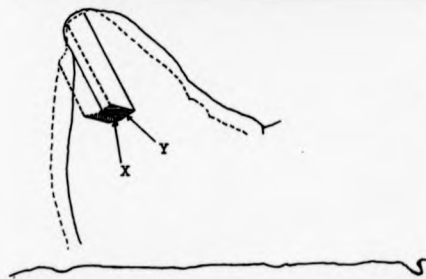
Figure 6.2 (a) and (b) SEM micrographs of front and back surfaces of copper sheet specimen annealed at 1000°C, (c) the trace of one of the  $\Sigma 3$  twin systems when seen from (a) with (b) in the proper position, as seen through the specimen; X and Y are the two segments of incoherent  $\Sigma 3$  twin boundary.



(a)



(b)



(c)

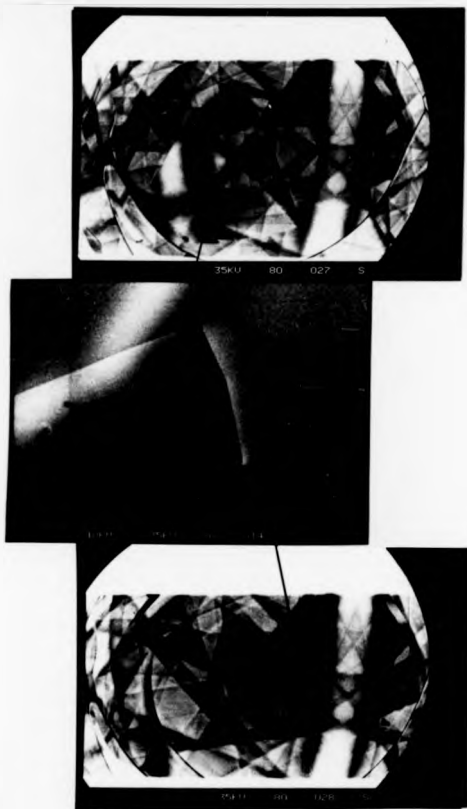


**Figure 6.3** (a) JEM micrograph of one of the  $\frac{1}{2}$  twin boundaries appearing in Figure 6.2 and the corresponding s.a.c.p.'s.

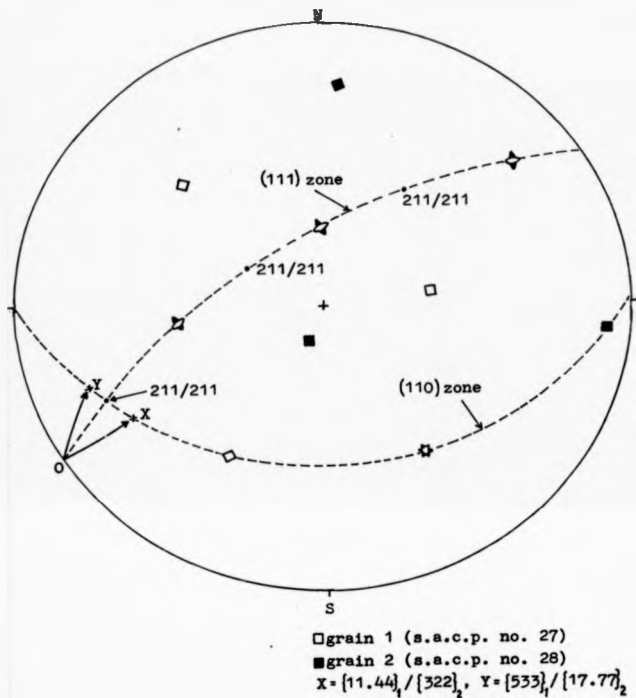


Figure 6.1 (b) The orientation of the  $\Sigma 3$  twin boundary shown in Figure 6.3 (a). The orientations of the two segments of incoherent twin boundary (lettered X and Y in Figure 6.2) are also shown, O would be the orientation of the incoherent twin boundary if it is perpendicular to the specimen surface and coherent  $\Sigma 3$  {111} planes.

TABLE 4: Full details of eight typical examples of the incoherent E3 twin boundary in

copper at 1000°C

| No. | Tilt of coherent<br>No. {111} plane from<br>the vertical | Displacement of<br>{211} from<br>vertical<br>≡ torque toward<br><110> zone (rad <sup>-1</sup> ) | Incoherent<br>boundary<br>X                  | Displacement of<br>X from {211}<br>≡ torque away<br>from {211} | Incoherent<br>boundary<br>Y                   | Displacement of Y<br>from {211}<br>≡ torque away<br>from {211} |
|-----|--|---|--|--|---|--|
| 1   | 22° ± 2°   | 16° ± 1° ± 0.29 ± 0.02  | {755} <sub>1</sub> /({311}) <sub>2</sub>     | 10° ± 1° ± 0.18 ± 0.02   | {733} <sub>1</sub> /({19.11.11}) <sub>2</sub> | 4° ± 1° ± 0.07 ± 0.02  |
| 2   | 45° ± 2°   | 6° ± 1° ± 0.10 ± 0.02   | {411} <sub>1</sub> /({877}) <sub>2</sub>     | 16° ± 1° ± 0.29 ± 0.02   | {211} <sub>1</sub> /({211}) <sub>1</sub>      | 0° ± 1° ± 0.00 ± 0.02  |
| 3   | 27° ± 2°   | 8° ± 1° ± 0.14 ± 0.02   | {322} <sub>1</sub> /({11.44}) <sub>2</sub>   | 8° ± 1° ± 0.14 ± 0.02  | {17.77} <sub>1</sub> /({533}) <sub>2</sub>    | 5° ± 1° ± 0.09 ± 0.02  |
| 4   | 32° ± 2°   | 13° ± 1° ± 0.23 ± 0.02  | {311} <sub>1</sub> /({755}) <sub>2</sub>     | 10° ± 1° ± 0.18 ± 0.02   | {19.11.11} <sub>1</sub> /({733}) <sub>2</sub> | 4° ± 1° ± 0.07 ± 0.02  |
| 5   | 18° ± 2°   | 14° ± 1° ± 0.25 ± 0.02  | {11.44} <sub>1</sub> /({322}) <sub>2</sub>   | 8° ± 1° ± 0.14 ± 0.02  | {533} <sub>1</sub> /({17.77}) <sub>2</sub>    | 5° ± 1° ± 0.09 ± 0.02  |
| 6   | 23° ± 2°   | 8° ± 1° ± 0.14 ± 0.02   | {522} <sub>1</sub> /({13.88}) <sub>2</sub>   | 6° ± 1° ± 0.10 ± 0.02  | {13.88} <sub>1</sub> /({522}) <sub>2</sub>    | 6° ± 1° ± 0.10 ± 0.02  |
| 7   | 17° ± 2°   | 25° ± 1° ± 0.47 ± 0.02  | {11.87} <sub>1</sub> /({11.83}) <sub>2</sub> | 10° ± 1° ± 0.18 ± 0.02   | {632} <sub>1</sub> /({643}) <sub>2</sub>      | 7° ± 1° ± 0.12 ± 0.02  |
| 8   | 27° ± 2°   | 16° ± 1° ± 0.29 ± 0.02  | {432} <sub>1</sub> /({11.53}) <sub>2</sub>   | 10° ± 1° ± 0.18 ± 0.02   | {11.53} <sub>1</sub> /({432}) <sub>2</sub>    | 10° ± 1° ± 0.18 ± 0.02   |

- Cu 99.99%, 0.10mm thick
- △ Cu 99.99%, 0.05mm thick
- Cu 99.999%, 0.10mm thick

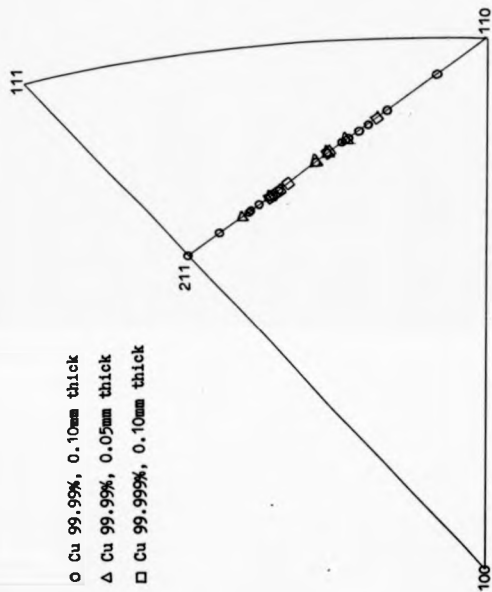


Figure 5.4 The orientation of the incoherent  $\Sigma_3$  twin boundaries if they were perpendicular to the specimen surface and coherent  $\Sigma_3$  {111} planes.

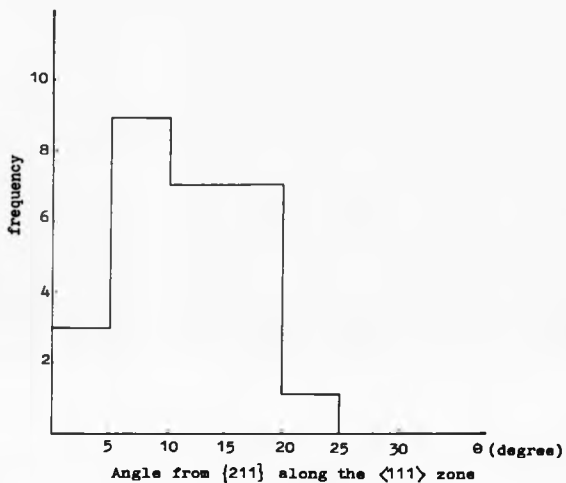


Figure 6.5 Distribution of the incoherent  $\Sigma_3$  twin boundaries if they were perpendicular to the coherent  $\Sigma_3$  {111} planes and specimen surface.

From all the incoherent  $\Sigma 3$  twin boundaries analysed, 85% were found to have orientations along  $\langle 110 \rangle$  zones (Figure 6.6.). Only 14% were found to lie on the common {211} planes. Most of them are clustered around a {322} orientation of one grain and {11.44}\* orientation of the other grain (shortly written as  $\{322\}_1/\{11.44\}_2$ ). This orientation is about  $8^\circ$  from a common {211} pole. The low frequency<sub>found</sub> for {211} planes as incoherent twin boundaries indicates that such interfaces may also be expected to be marginally unstable against faceting.

The occurrence of such clustered orientations may be regarded as being due to two mutually perpendicular types of torque term. The first torque acts on the vertical plane and rotates it toward a common {211} pole along a common  $\langle 111 \rangle$  zone. The second torque then acts on this plane and rotates it along  $\langle 110 \rangle$  zone away from a common {211} pole. However, in an actual case, these two torques may well act simultaneously.

None of the incoherent  $\Sigma 3$  twin boundaries analysed were found to have a {110} orientation. The smallest angle between adjacent {110} planes that are common to twin crystals is  $60^\circ$ . All the assumed vertical planes, including the largest one which is  $25^\circ$  away from a common {211} pole, were found to rotate toward a common  $\langle 110 \rangle$  zone, rather than to a common {110} pole. It is assumed that this is due to the energy of  $\Sigma 3$  twin boundary at the {211} orientation being lower than the energy of the incoherent boundary at the {110} orientation. In fact, we deduce later in the next section that  $\gamma_{110} > 1.15 \gamma_{211}$  for  $\Sigma 3$  boundaries.

---

\*Miller indices greater than 9 are followed by a dot, for example, {11.4.4} is written as {11.44}



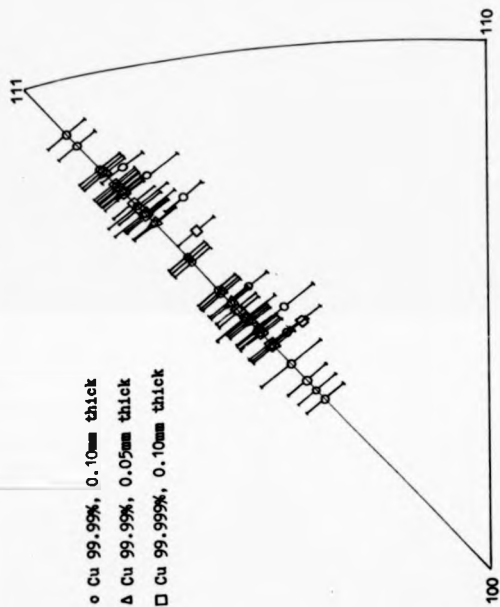


Figure 6.6 The orientations of the incoherent  $\Sigma 3$  twin boundaries measured from copper sheets annealed at 1000°C.

The plot of the Herring torque term for incoherent  $\Sigma_3$  twin boundary against the angle from  $\langle 110 \rangle$  zone is shown in Figure 6.7. As the  $\Sigma_3$  unit cell, and therefore the  $\gamma$ -plot, is hexagonal, then the  $\{110\}$  planes in the unique  $\langle 111 \rangle$  zone are mirror planes. Therefore these  $\langle 110 \rangle$  zones are maxima or minima in the  $\gamma$ -plot. As the incoherent plane rotates toward the  $\langle 110 \rangle$  zone, the  $\gamma$ -plot must have a minimum there. A cusped minimum is consistent with our results and the torque terms for such a cusped minimum are shown in Figure 6.7.

The orientations of the steps of incoherent twin boundary alongside a  $\Sigma_3$  boundary (as C in Figure 6.1) were also investigated. It was found that all of them were, within experimental error, parallel to the incoherent twin boundary at the end of coherent  $\Sigma_3$  twin boundary in the same grain.

The results from the specimens of nominal purity 99.99% and 99.999% were indistinguishable, so impurities at this level have negligible effect.

The possible objections that may be raised to the technique used in determining the orientation of the boundary plane is that it is necessary to assume that the boundary is in an equilibrium configuration and that it has a flat interface. The latter could be checked by sectioning the specimen, normal to both surface and grain boundary trace. However, this difficult operation was not attempted. The grain boundary examined may not yet be in a local equilibrium configuration, as it may still involve in the kinetic process due to the Mullins' (1958) grain boundary groove anchoring. However, it would be expected that the occurrence of such situations would lead to

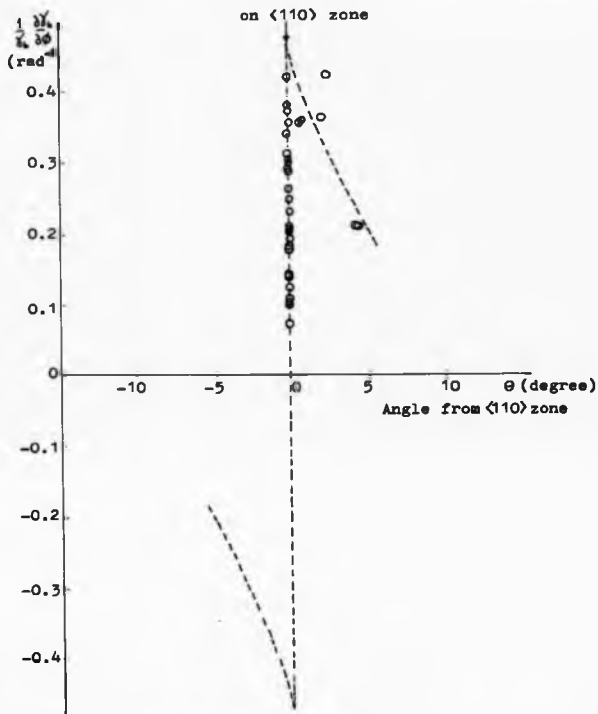


Figure 6.7 Plot of  $\frac{1}{\Delta L} \Delta L_0$  against the angle from  $\langle 110 \rangle$  zone for the incoherent  $\mathcal{L}_3$  boundaries.

random scatter in the observations, rather than a systematic error.

The crystallographic plane of the incoherent twin boundary depends on the material. Our observations in copper at 1000°C appear to be quite consistent with the observations made by Fullman (1951). His observations on copper, after a prolonged anneal at 1040°C that these interfaces were approximately  $\{113\}_1/\{335\}_2$ . These two planes however are not exactly parallel and make an angle of about 5° with each other in the twinned  $\Sigma 3$  structure (see Table 5). The  $\{322\}_1/\{11.44\}_2$  planes of incoherent  $\Sigma 3$  twin boundaries found in the present investigation lie between the planes quoted by Fullman. Sargent (1968) has reported that these interfaces in aluminium are  $\{7\bar{1}1\}_1/\{155\}_2$  and  $\{211\}_1/\{211\}_2$ . The latter type has also been reported by Goodhew et al. (1978) in thin film bicrystals of gold and by Matthews (1962) in evaporated silver specimens. Incoherent twin interfaces in a 78% Ni-Fe alloy have been reported by Dash and Brown (1963) to be  $\{53\bar{1}\}_1/\{351\}_2$ ,  $\{110\}_1/\{110\}_2$  and  $\{533\}_1/\{17.77\}_2$ . The  $\{110\}_1/\{110\}_2$  type has also been reported by Vaughan (1970) in an austenitic stainless steel. He also found in the same specimen the incoherent twin planes of the type  $\{13.55\}_1/\{11.77\}_2$ .

#### 6.3.1.1. $\sqrt{\gamma}$ -plot and $\bar{\Gamma}$ -plot

When the disorientation between two adjacent crystals is well defined and fixed, then the only anisotropy of grain boundary energy is associated with the orientation of the boundary plane. It is convenient to represent this anisotropy by means of a  $\sqrt{\gamma}$ -plot. When the grain boundary energy is sufficiently anisotropic, it is possible

TABLE 5: Typical sets of parallel plane on a common

 $\langle 110 \rangle$  zone in  $\underline{L}_3$ 

| parallel plane on<br>a common $\langle 01\bar{1} \rangle$ zone | Angle from $[211]$ pole<br>along $\langle 01\bar{1} \rangle$ zone |
|--|---|
| $[511]_1/[111]_2$  | $19.47^\circ$   |
| $[411]_1/[877]_2$  | $15.79^\circ$   |
| $[31.88]_1/[766]_2$  | $15.21^\circ$   |
| $[26.77]_1/[655]_2$  | $14.42^\circ$   |
| $[722]_1/[544]_2$  | $13.26^\circ$   |
| $[16.55]_1/[433]_2$  | $11.42^\circ$   |
| $[311]_1/[755]_2$  | $10.02^\circ$   |
| $[11.44]_1/[322]_2$  | $8.05^\circ$  |
| $[833]_1/[20.13.13]_2$   | $7.33^\circ$  |
| $[522]_1/[13.88]_2$  | $5.77^\circ$  |
| $[17.77]_1/[533]_2$  | $5.05^\circ$  |
| $[733]_1/[19.11.11]_2$   | $4.04^\circ$  |

for a high energy boundary to decompose into facets of other orientation. According to Herring (1951), the condition that an interface be stable thermodynamically is that the orientation must be contained on the equilibrium shape. Thus, if a grain boundary facets, it is only for the facet orientation that the grain boundary energy can be measured. For orientations which disappear on faceting, the  $\Gamma$ -plot represents the minimum possible value of the  $\gamma$ -plot (see Section 3.2).

To construct the  $\Gamma$ -plot for  $\Sigma 3$  boundaries, we start with the well-known deep cusps at  $\langle 111 \rangle$ . The energy of the coherent  $\{111\} \Sigma 3$  can be measured in terms of  $\gamma_{111}/\gamma_s$  (Figure 6.8), which gives results of  $0.013 \pm 0.004$ . Using a value of  $\gamma_s = 1.78 \text{ Jm}^{-2}$  (Murr 1972) gives  $\gamma_{111} = 23 \text{ mJm}^{-2}$ . The sharpness of the cusp can be estimated, by analogy with a small angle boundary, in terms of an array of partial dislocations, which rotate the boundary plane away from  $\{111\}$ . This gives the torque terms  $\frac{\partial \gamma}{\partial \theta}$  at  $\{111\}$  to be approximately equal to  $E/b$ , where  $E$  is the dislocation line energy and  $b$  is the Burgers vector. Choosing the values for copper of  $E \approx 2 \times 10^{-9} \text{ Jm}^{-1}$ ,  $b \approx 10^{-10} \text{ m}$  and  $\gamma_{111} = 20 \text{ mJm}^{-2}$  gives  $\frac{1}{\gamma_{111}} \left( \frac{\partial \gamma}{\partial \theta} \right) \approx 1000 \text{ rad}^{-1}$ , which is so large that faceting is inevitable (see Section 3.2).

The energy of  $\Sigma 3$  incoherent  $\Sigma 3$  boundary (which will be approximately the same for  $\gamma_{211}$  or  $\gamma_{322/11.44}$ ) can again be measured in terms of  $\gamma_{111}/\gamma_s$  (Figure 6.9). This ratio is about 0.24, which gives  $\gamma_{211} = 430 \text{ mJm}^{-2}$  (or rather  $\gamma_{322/11.44}$ ). This enables us to draw the  $\{011\}$  section through the  $\Sigma 3$   $\Gamma$ -plot, as shown in Figure 6.10(a); the dotted line is drawn because the energy at  $\langle 211 \rangle$  orientation is not



(Magn. x800)

(a)



(Magn. x930)

(b)

Figure 6.8 (a) Optical micrograph showing a typical pair of coherent  $\Sigma 3$  twin boundary in copper annealed at 1000°C; (b) interferogram of (a), (Hg light, fringe height = 0.29  $\mu\text{m}$ ).



(Magn. x930)

(a)



(Magn. x1330)

(b)

Figure 6.9 (a) Optical micrograph of a typical incoherent  $\Sigma 3$  twin boundary in copper annealed at 1000°C; and (b) interferogram of (a), (Hg light, fringe height = 0.29 $\mu$ m).



reliable.

The  $\{111\}$  section of the  $\Gamma$ -plot can be estimated from the fact that all the measured incoherent  $\Sigma_3$  boundaries rotated to the  $\langle 110 \rangle$  zone (see Figures 6.4 and 6.6). Though none of our specimens had an initial orientation exactly on  $\{110\}$ , the boundary within  $5^\circ$  from  $\{110\}$  rotated toward  $\{211\}$ . We therefore assumed that the  $\chi_{110}$  is so large that it is not part of the  $\chi$ -plot. The  $\{111\}$  section of the Wulff shape therefore consists of a hexagon, as shown in Figure 10(b). From this plot, it can be shown that  $\chi_{110}/\chi_{211} > 1.155$  (i.e.  $1/\cos 30^\circ$ ). In three dimensions, the form of the  $\Sigma_3$   $\Gamma$ -plot looks like a corrugated doughnut, with a central depression, which is not quite a hole.

#### 6.4 $\Sigma_9$ boundaries

$\Sigma_9$  can be considered as two successive  $\Sigma_3$  twinings on different  $\{111\}$  planes. The  $\chi$  and  $\Gamma$  plots for  $\Sigma_9$  have orthorhombic symmetry. As the  $\Sigma_9$  relation is the product of two  $\Sigma_3$  relations, a  $\Sigma_9$  boundary can break up into two  $\Sigma_3$  boundaries. For this to be energetically possible, the  $\Sigma_9$  energy of any given direction must be greater than the sum of the two  $\Sigma_3$  energies in the same direction. As we know the  $\Sigma_3$   $\Gamma$ -plot (Figures 6.10(a) and (b)), we can add together two  $\Sigma_3$   $\Gamma$ -plots in the proper orientation relation. This has been done in Figure 6.11.

The mirror planes for the  $\Sigma_9$  unit cell are  $\{110\}$ ,  $\{11\bar{4}\}$  and  $\{2\bar{2}1\}$ , as shown in Figure 6.11. If a hypothetical  $\Sigma_9$   $\chi$ -plot were spherical (as in Figure 6.11), then the region where the  $\Sigma_9$  plot is inside the sum of the two  $\Sigma_3$  plots (as at A in 6.11) represents the

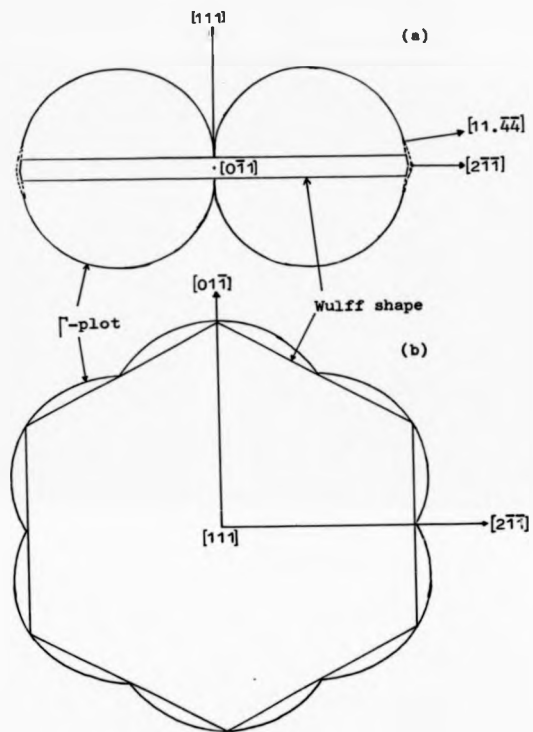
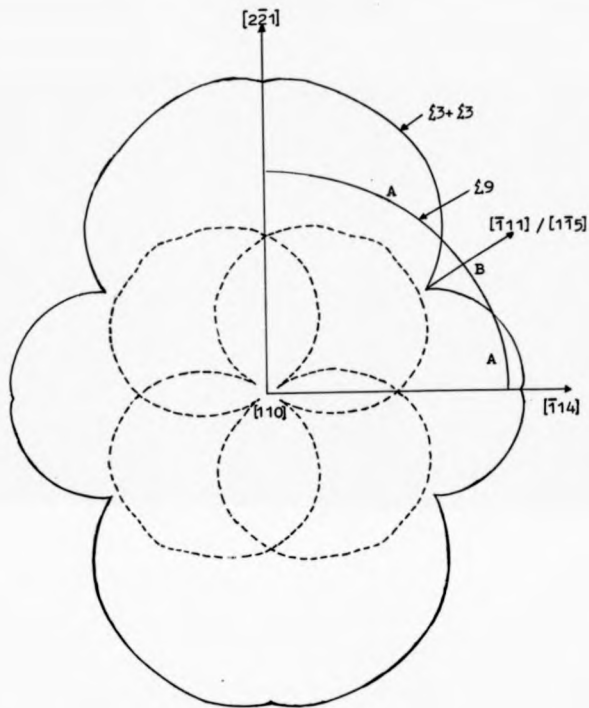


Figure 6.10 (a) (011) and (b) (111) sections through the  $\Gamma$ -plot and the Wulff shape for the  $\Sigma_3$  twin boundaries. Scale:  $10\text{mm} = 86 \text{ mJm}^{-2}$ .



**Figure 6.11** (a), (110) section through the  $\Sigma 9$   $\Gamma$ -plot obtained by adding together two  $\Sigma 3$   $\Gamma$ -plots (dotted curves) in the proper direction. A hypothetical  $\Sigma 9$   $\gamma$ -plot is also drawn (assumed to be a sphere) for describing the criterion for the break up of a  $\Sigma 9$  boundary. Scale  $10\text{mm} = 86\text{ mJm}^{-2}$ .

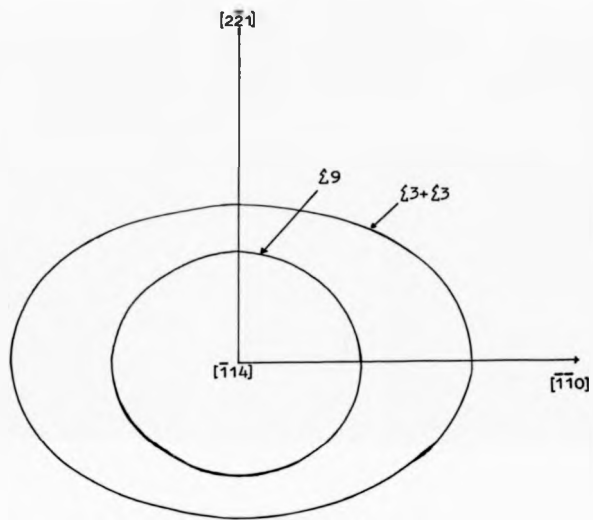


Figure 6.11 (b)  $(\bar{1}14)$  section through the  $L9$   $\Gamma$ -plot obtained by adding together two  $L3$   $\Gamma$ -plots in the  $[1\bar{1}0]$  and  $[2\bar{2}1]$  directions and then drawing an elliptical  $L3 + L3$   $\Gamma$ -plot through them. Scale  $10\text{mm} = 172 \text{ mJm}^{-2}$ .

region where a  $\Sigma_9$  boundary is stable. Where the  $\Sigma_9$  plot is outside the sum of the two  $\Sigma_3$  plots (as at B in Figure 6.11), the  $\Sigma_9$  boundary is unstable and will dissociate into two  $\Sigma_3$  boundaries.

Whereas the incoherent  $\Sigma_3$  boundaries (as at B in Figure 6.1) are free to rotate, the  $\Sigma_9$  boundaries are anchored at one or two lines formed by the intersection of  $\Sigma_3$  {111} planes (Figure 6.12). The  $\Sigma_9$  boundaries fixed at both ends by lines in the  $\langle 110 \rangle$  direction can be flat or curved. If they are flat, their orientation must be on the  $\langle 110 \rangle$  zone. If they are curved (twisted) (Figure 6.13), the direction of the bending gives the direction of the Herring torque term. The other possibility is that the  $\Sigma_9$  boundary can break up into two  $\Sigma_3$  boundaries, as discussed above.

#### 6.4.1 Results and discussion

As for  $\Sigma_3$  boundaries, only those  $\Sigma_9$  boundaries which appeared on both sides of the specimen surface were fully analysed.

Of fifteen macroscopically flat  $\Sigma_9$  boundaries measured, six were found to have interfaces parallel to a common (221) plane, four were oriented parallel to a common (114) plane (one of these is shown in Figure 6.14), one was found parallel to a common (110) plane, two were found to have interfacial planes of the type  $\{111\}_1/\{115\}_2$ , and one each of the type  $\{771\}_1/\{557\}_2$  (see Figure 6.15) and  $\{447\}_1/\{001\}_2$ .

Many more  $\Sigma_9$  boundaries, which show a straight trace on one surface, have been observed in the specimens studied. However, they were not visible on the other side of the specimen, so the direction of the boundary plane could not be determined by the method discussed

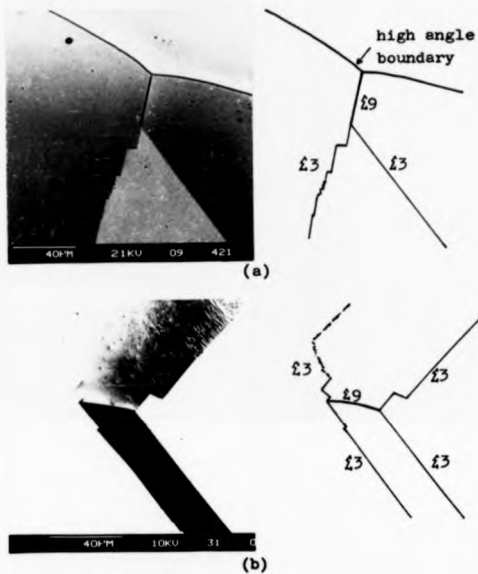


**Figure 6.12** SEM micrographs showing the anchored  $L_9$  boundaries, (a) at one end and (b) at both ends, formed by the intersection of coherent  $L_3$  {111} planes. In (a), the other end of the  $L_9$  boundary intersects with a high-angle boundary which can move.

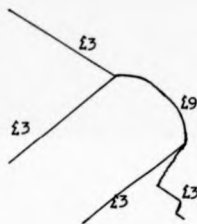


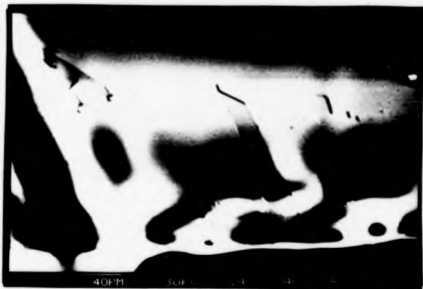
Figure 6.13 SEM micrograph showing a curved 19 boundary.

Figure 6.14 (a) and (b) SEM micrographs showing the same macroscopically flat  $\Sigma 9$  boundary on both sides of the specimen surface. AC =  $\Sigma 3$ , AB =  $\Sigma 3$  and BC =  $\Sigma 9$ . (c) the trace of the boundaries when seen from (a) with (b) in the proper position, as seen through the specimen.

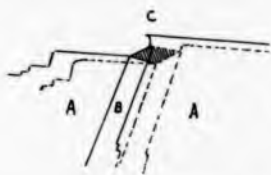




(a)



(b)



(c)



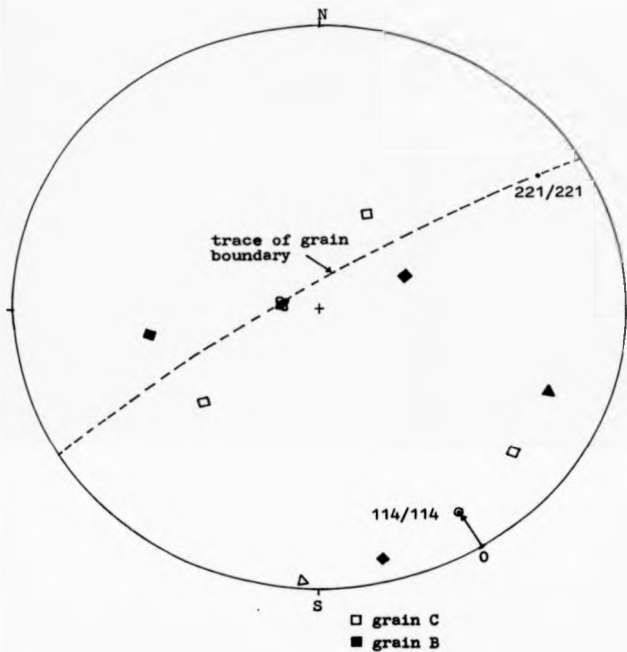


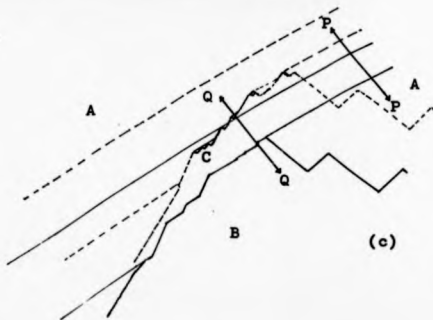
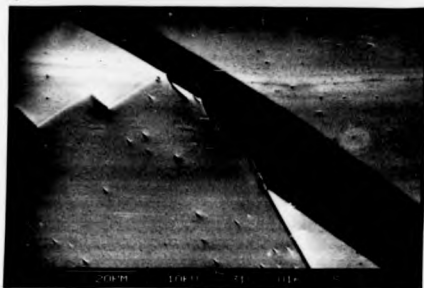
Figure 6.14 (d) The orientation of the  $\{114\}_1/\{114\}_2$  boundary appearing in Figures 6.14 (a) and (b). O would be the  $\{114\}_2$  boundary plane if it were perpendicular to the surface.

above. However, by judging from the direction of their line of intersection with the surface, most of them also lie in the common  $\langle 110 \rangle$  zone.

The occurrence of the  $\{110\}$ ,  $\{221\}$  and  $\{114\}$  interfaces of the  $\Sigma_9$  boundaries is connected with the fact that crystallographically  $\{110\}$ ,  $\{221\}$  and  $\{114\}$  are the three mutually perpendicular symmetry planes in the  $\Sigma_9$  relation. They have highest, but different planar density of coincident sites (Andreyeva 1980). The observation of the  $\Sigma_9$  boundaries which have interfacial planes of the type  $\{111\}_1/\{115\}_2$  is consistent with those of Vaughan (1970) and Sukhomlin (1982).

Triangular twins have been observed to occur quite frequently at some  $\Sigma_9$  boundaries in the specimens studied (Figures 6.15 and 6.17). The crystallography of these twins is such that they are bounded by two coherent  $\Sigma_3$   $\{111\}$  interfaces and one incoherent  $\Sigma_3$  interface. If the latter is parallel to a common  $\{211\}$  plane then these triangular twins will have a prismatic shape with a  $\langle 110 \rangle$  direction. Such triangular twins are visible on one side of the specimen, as can be seen in Figure 6.15, but they are not visible on the other side of the specimen. On the latter side, only a faceted  $\Sigma_9$  is visible. Inside the specimen, the  $\Sigma_9$  boundary in Figure 6.15 is thought to be as shown in Figure 6.16. The  $\Sigma_9$  boundary of the type  $\{771\}_1/\{557\}_2$  does not split up. But when the direction changes it splits into two  $\Sigma_3$  boundaries. Therefore, the reaction  $\Sigma_9 \neq \Sigma_3 + \Sigma_3$  can occur, depending on the spatial orientation of the boundaries, which exerts a direct influence on the energies of the boundaries. Obviously, as discussed above, in directions where the energy of a  $\Sigma_9$  boundary is

Figure 6.15 (a) SEM micrograph showing facets of  $\Sigma 9$  boundary. (b) SEM micrograph on the other side of (a) showing the break-up (triangular  $\Sigma 3$  twins) and non break up of the  $\Sigma 9$  boundary. (c) The trace of the boundaries when seen from (a) with (b) in the proper position, as seen through the specimen.



AB = £3  
AC = £3  
BC = £9

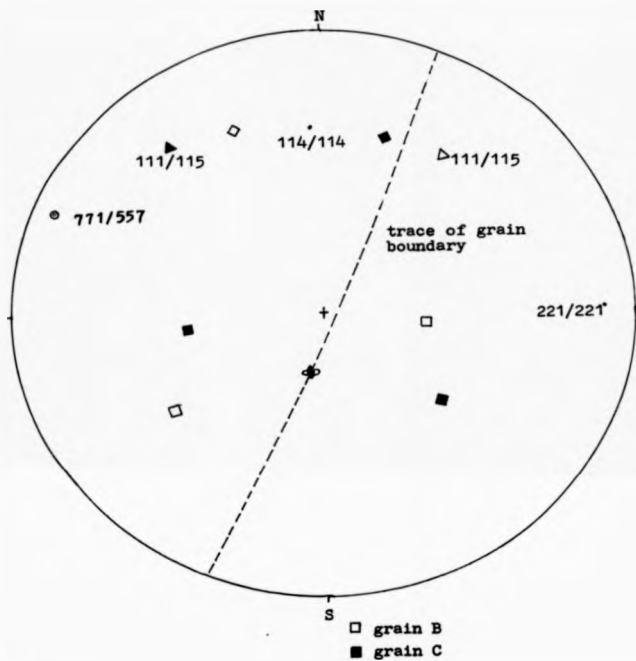
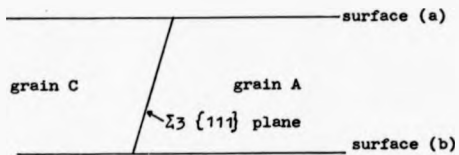
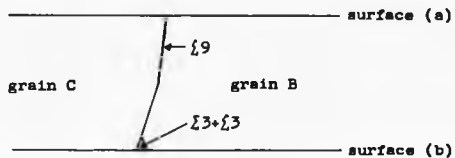


Figure 6.15 (d) The orientation of the  $\Sigma_9$   $(7\bar{7}1)_1/(557)_2$  boundary appearing in Figures 6.15 (a) and (b).



vertical section at PP



vertical section at QQ

Figure 6.16 Vertical sections at PP and QQ through specimen shown in Figure 6.15 (c).

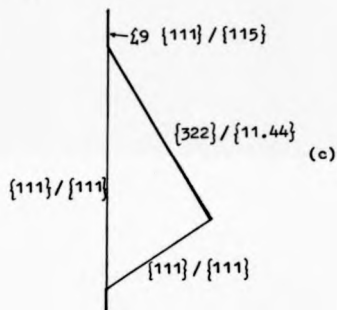
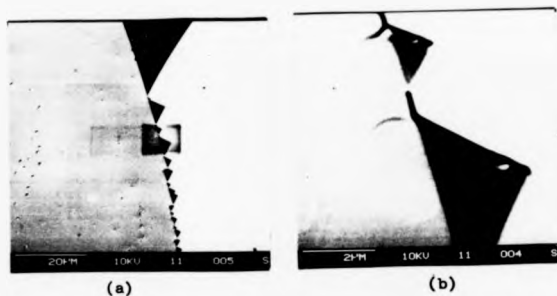


Figure 6.17 (a) SEM micrograph showing typical triangular  $L_3$  twins at the  $L_9$  boundary in copper annealed at  $1000^{\circ}\text{C}$ . (b) The triangular twins and  $L_9$  boundaries appearing in the contaminated area in (a). (c) The crystallographic of the  $L_9$  boundary and triangular twin.



greater than the total energy of two  $\Sigma_3$  boundaries, it will break up into two  $\Sigma_3$  boundaries.

If the incoherent boundary in the split  $\Sigma_3 + \Sigma_3$  boundary is  $\{322\}_1 / \{11.44\}_2$  (Figure 6.17), then instead of prismatic grains, the triangular grains will be tetrahedra and the general orientation of the  $\Sigma_9$  boundary will be tilted away from the  $\langle 110 \rangle$  zone.

Our observation of triangular twins is in fact consistent with those of the other investigators. For example, twin triangles have also been observed by Vaughan (1970) in stainless steel, by Goodhew et al. (1978) in thin film bicrystals of gold, by Howell and Bee (1978) in pure copper, stainless steel, 70/30 brass and nickel-base superalloy. Following Dash and Brown (1963), Vaughan has suggested that the triangular twins are formed due to the interaction between two  $\Sigma_3$  boundaries, rather than by the dissociation process.

As for the  $\Sigma_3$  boundary, the energy of the  $\Sigma_9$  boundary can again be measured in terms of  $\gamma_{\Sigma_3}/\gamma_s$  (Figure 6.18). Using this method, we obtained that  $\gamma_{\Sigma_3}/\gamma_s = 0.22 \pm 0.02$ ,  $\gamma_{\Sigma_9}/\gamma_s = 0.23 \pm 0.02$  and  $\gamma_{\Sigma_9}/\gamma_s = 0.24 \pm 0.02$ . Using the value of  $\gamma_s = 1.78 \text{ Jm}^{-2}$  (Murr 1972) gives  $\gamma_{\Sigma_3} = 392 \text{ mJm}^{-2}$ ,  $\gamma_{\Sigma_9} = 410 \text{ mJm}^{-2}$  and  $\gamma_{\Sigma_9}/\gamma_s = 430 \text{ mJm}^{-2}$  (all  $\pm 10\%$ ). The effective " $\Sigma_9$ " (i.e.  $\Sigma_3 + \Sigma_3$ ) boundary energy, when assumed to consist of segments of  $\{111\}$ ,  $\{111\}$  and  $\{322\}_1 / \{11.44\}_2$  prisms, as shown in Figure 6.17, can be calculated to be 0.25 expressed as  $\gamma_{\Sigma_9}/\gamma_s$ . Because the length of the trace of the  $\Sigma_9$   $\{771\}_1 / \{557\}_2$  and  $\Sigma_9$   $\{447\}_1 / \{001\}_2$  is short, so it is difficult to obtain their interferograms. However by using the faceting theory, and assuming reasonable torque terms, we can then calculate that



(Magn. x300)

(a)



(Magn. x950)

(b)

Figure 6.18 (a) Optical micrograph of a typical  $L_9$  boundary in copper annealed at  $1000^\circ\text{C}$ ; (b) interferogram of (a), (Hg light, fringe height =  $0.29\mu\text{m}$ ).

$\gamma_{111}/557/\gamma_s = 0.25$  and  $\gamma_{442}/66/\gamma_s = 0.24$  (i.e. taking  $\frac{1}{\gamma_s} \left( \frac{\gamma_{111}}{557} \right)$  to be 0.08 and 0.02  $\text{rad}^{-1}$  respectively). Using the measured and the calculated energy values above, we can then replace a hypothetical  $\Sigma 9$   $\gamma$ -plot, as drawn in Figure 6.11, with the  $\Sigma 9$   $\gamma$ -plot consistent with these measurements as shown in Figure 6.19.

Five macroscopically curved  $\Sigma 9$  boundaries have been analysed. The morphology of these boundaries is rather complicated as they were observed to curve toward one grain on one side of the specimen surface and toward the other grain on the other side of the specimen surface (Figure 6.20). Such curvature of the boundary causes difficulties in determining an average direction of the boundary plane. However, from all the boundaries measured, by judging from their average inclinations and the direction of their line of intersection, three interfaces were found to lie approximately parallel to a common  $\{221\}_{\text{para}/h}$  plane and the other two interfaces lie approximately  $\perp$  to a common  $\{114\}$  plane. The existence of such complex curvature of the  $\Sigma 9$  boundaries is expected to be due to the action of grain boundary torque and surface energy anisotropy (Miller and William 1967).

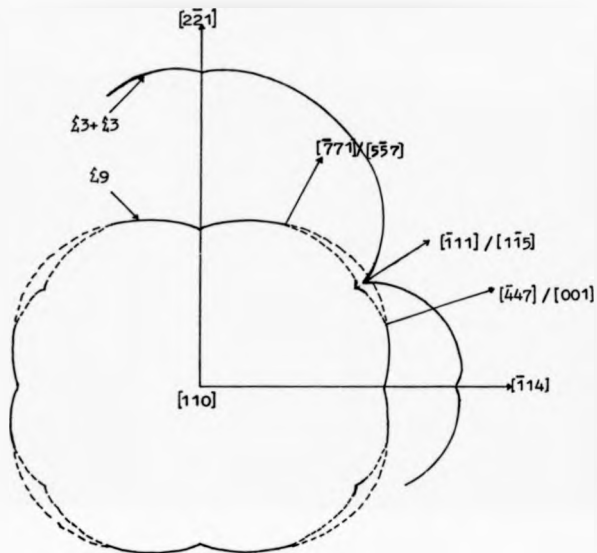


**Figure 6.19** (110) section through the  $L_9$  plot. The dotted line represents the unknown energies. Near the  $L_{111}/[1\bar{1}5]$  orientation, the boundary breaks up into facets consisting for example of section of  $L_9$   $L_{771}/[5\bar{5}7]$  and two  $L_3$  of  $L_{111}/[1\bar{1}5]$ . Scale:  $10\text{mm} = 86$

$\text{mJm}^{-2}$ .

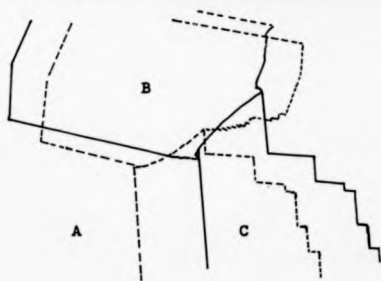
Figure 6.20 (a) and (b) SEM micrographs of front and back surfaces of copper sheet showing a complex curvature of  $\Sigma 9$  boundary. (c) The trace of the boundaries when seen from (a) with (b) at the proper position, as seen through the specimen.



(a)



(b)



(c)

$AB = 2.3$   
 $AC = 2.3$   
 $BC = 2.9$

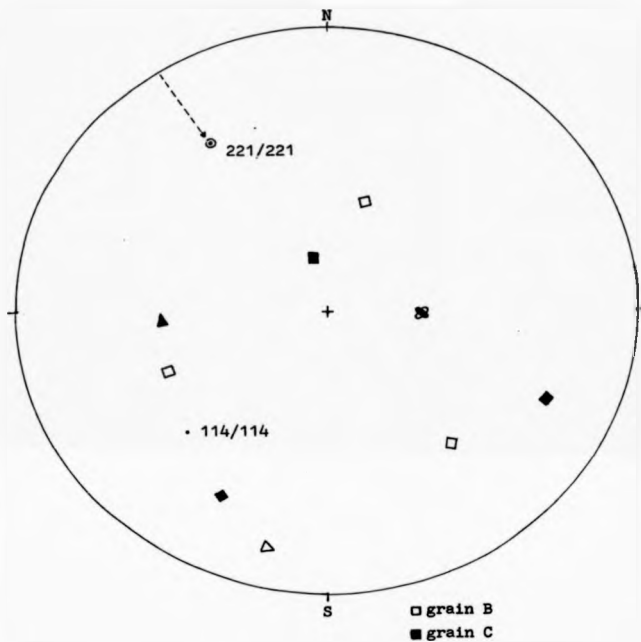


Figure 6.20 (d) The orientation of the curved  $\bar{1}9$  boundary appearing in Figure 6.20 (a) and (b).

#### CHAPTER 7: GENERAL CONCLUSION

Selected area electron channelling patterns (s.a.c.p.'s) are easy to generate in the scanning electron microscope (SEM). They offer, rapidly and conveniently, detailed crystallographic information about the specimen from chosen areas of the sample. The most obvious and widespread <sup>use</sup> of these patterns is for the determination of orientation of crystals. However, there is a relative rotation between the s.a.c.p. and the normal micrograph. In the Cambridge Stereoscan S 250 MK 3 used, this relative rotation was found to be in a clockwise sense, depending on the "working distance" setting, between the s.a.c.p. and normal micrographs, and must be added to the  $180^\circ$  inversion. This relative rotation effect was taken into account when accurate absolute orientations determinations were made, and when crystallographic directions of the boundary planes in the specimens were deduced. When only the disorientation was required, without needing to know the boundary plane orientation, then the rotation matrix could be determined directly, without taking account of relative rotations.

Herring torque terms were measured in high purity copper wires having a "bamboo" structure, annealed at  $1000^\circ\text{C}$ . In such a specimen, the Hess relation (Equation 5.4) applies as the disorientation across a boundary is fixed and the boundary plane rotated (due to the Herring torque terms) into the minimum energy position. The "hanging" wire specimens gave a large number of special boundaries (35% CSL, 21% low-angle boundary), as expected from the freedom of the "bamboo" crystals to rotate. In comparison the "horizontal" wires were more



constrained and had more random high-angle boundaries. In general, the CSL and low-angle boundaries were associated with high value of the torque terms, whereas random high-angle boundaries with low value of the torque terms. Most of the boundaries measured were found to be of mixed tilt and twist types with a larger tilt component. This is to be expected for randomly oriented crystals in polycrystalline specimens.

The crystals in wire specimens rotate easily about the vertical axis, when the boundary plane is perpendicular to that axis, driven by the Pond and Smith (1977) mechanism. But they are rather difficult to rotate about the two mutually perpendicular horizontal axes (in the boundary plane), driven by the Shewmon (1966) mechanism, as it introduces diffusional mass transport and gravitational torques. The "kinking" observed to occur at many boundaries confirm the effect of the Shewmon and gravitational torques.

One of the most interesting conclusions from this analysis is that the  $\Sigma_{11}$  boundaries have been found to have significantly lower energy than the other CSL boundaries (except for  $\Sigma_3$  and  $\Sigma_9$  boundaries). The  $\{110\}$  section of the  $\Sigma_{11}$   $\gamma$ -plot was deduced (Figure 5.12). The occurrence of the cusps at  $\{311\}$  and  $\{3\bar{3}2\}$  is as expected. These planes are the mirror planes in the  $\Sigma_{11}$  relation. A cusp at the  $\{110\}$  symmetry plane is expected but was not observed.

$\Sigma_3$  and  $\Sigma_9$  boundaries were investigated using high purity copper sheet specimens, annealed at  $1000^\circ\text{C}$ . The  $\Sigma_3$  boundaries are well known to facet into coherent and incoherent boundaries. Thus the proper way of analysing such a boundary is by using a  $\gamma$ -plot, as it represents

the minimum possible value of the  $\gamma$ -plot. The Herring torque terms for the incoherent twin boundaries (as at B in Figure 6.1(a)) have been evaluated by using the Hess relation (Equation 5.4). This relation applies as the  $\Sigma_3$  {111} planes are at a fixed separation and the specimen thickness is fixed. As is well known, a sharp cusp occurs in the  $\Sigma_3$   $\gamma$ -plot when the interface is parallel to the {111} twinning plane. It is found that a further (shallower) cusp occurs when the incoherent  $\Sigma_3$  boundary plane is approximately parallel to the {322} plane in one crystal and <sup>the</sup> {11.44} plane in the other crystal.

As the  $\Sigma_9$  relation is equivalent to two  $\Sigma_3$  relations, then in some circumstances, the  $\Sigma_9$  boundary can break up into two  $\Sigma_3$  boundaries. The Hess relation, however, cannot be applied to the  $\Sigma_9$  boundaries in these specimens because the boundary is anchored by intersection <sup>with</sup>  $\Sigma_3$  {111} planes. But the  $\Sigma_9$   $\gamma$ -plot could still be evaluated as the energy of  $\Sigma_9$  boundaries can be measured. This plot has then been related to the " $\Sigma_3 + \Sigma_3$ "  $\gamma$ -plot, in order to yield information about the stability of the  $\Sigma_9$  boundary. It is found that only those  $\Sigma_9$  boundaries which are near the {111} orientations in one crystal (i.e.  $\{111\}_1/\{115\}_2$ ) will break up into facets consisting for example of section of  $\Sigma_9$  of  $\{771\}_1/\{557\}_2$  and two  $\Sigma_3$  of  $\{111\}_1/\{115\}_2$ . Most of the macroscopically flat  $\Sigma_9$  boundaries were found to lie parallel to the common {221} and {114} planes. This is connected with the fact that they are mutually perpendicular symmetry planes in the  $\Sigma_9$  relation. Whereas some of the  $\Sigma_9$  boundaries are planar interfaces, some of the anchored  $\Sigma_9$  boundaries have been observed to have curved interfaces. Such curvature is expected to be due to the grain boundary

torque and surface energy anisotropy.

Although our observations of the  $\Sigma 9$  boundaries are quite consistent with those of the other investigators (e.g. Vaughan 1970), however there is a difference in the specimen used. In their case, the boundaries were observed from specimens which had been sliced from bulk specimens. But in our case, the specimen used was a thin sheet and therefore we can apply the Nesi relation and calculate the Herring torque terms.

The dependence of grain boundary energies on crystal disorientation is well known. The study of the effect of boundary orientation on boundary energies reported here shows that the grain boundary torque has indeed made a significant contribution to the energies of grain boundaries. However, it should be remembered that the crystal geometry is not the sole determinant of the energies of grain boundaries, as the electronic interactions are likely to play a significant part too (see Maurer and Gleiter 1985).

Many special boundaries can be found in the "hanging" wire specimens. Thus, if many more boundaries are measured (for example, ten times more than the measured boundaries in this work), it is possible to deduce the  $\gamma$ -plot of other common special boundaries, as well as the  $\gamma$ -plot of  $\Sigma 11$  boundaries reported here. Though the material used in the present work is pure copper, the study of the same kind can of course be extended to other types of material, for example, aluminium, nickel, molybdenum, etc. Furthermore, the effect of impurities can also be investigated (e.g. Donald 1976). Higher order twin boundaries (e.g.  $\Sigma 27$  and  $\Sigma 81$ ) have also been observed in

the sheet specimens. Therefore, it is possible to study these boundaries in the same way as the  $\mathcal{L}_3$  and  $\mathcal{L}_9$  boundaries reported here.

REFERENCES

- Ahmad, U.M. and Murr, L.E. (1975), Mater. Sci. Eng., 20, 291
- Andreyeva, A.V. (1980), Fiz. Metall. Metalloved, 49, 706
- Astrom, H.U. (1956), Acta Met., 4, 562
- Aust, K.T. and Chalmers, B. (1950), Proc. Roy. Soc. (London), A204, 359
- Aust, K.T. and Rutter, J.W. (1956), Trans. AIME, 215, 119
- Baluuffi, R.W. (1979), "Interfacial Segregation", edited by W.C. Johnson and J.M. Blakely, (Metals Park, Ohio: American Society for Metals), p.193
- Barnes, R.S. and Mazey, D.J. (1960), Phil. Mag., 5, 1247
- Basterfield, J. and Miller, W.A. (1969), Scripta Met., 3, 343
- Bishop, G. and Chalmers, B. (1968), Scripta Met., 2, 113
- Bishop, G.R., Hartt, W.H. and Bruggeman, G.A. (1971), Acta Met., 19, 37
- Bollmann, W. (1970), "Crystal Defects and Crystalline Interfaces", (New York: Springer-Verlag), p.143
- Booker, G.R. and Stickler, R. (1972), J. Mater. Sci., 7, 712
- Brandon, D.G. (1966), Acta Met., 14, 1479
- Brandon, D.G., Ralph, B., Ranganathan, S. and Wald, M.S. (1964), Acta Met., 12, 813
- Chalmers, B., King, R.T. and Shuttleworth, R. (1948), Proc. Roy. Soc. (London), A193, 465
- Christian, J.W. (1975), "The Theory of Transformations in Metals and Alloys", second edition, (Oxford: Pergamon), p.153
- Coates, D.G. (1967), Phil. Mag., 16, 1179

- Cullity, B.D. (1978), "Elements of X-ray Diffraction", second edition,  
(Reading: Addison-Wesley), Chapter 8
- Dash, S. and Brown, N. (1963), Acta Met., 11, 1067
- Davidson, D.L. (1976), J. Phys. E., 9, 341
- Davidson, D.L. (1984), Intern. Metals Rev., 29, 75
- Deschamps, M., Baribier, F. and Marrouche, A. (1987), Acta Met., 35,  
101
- Donald, A. (1976), Phil. Mag., 34, 1185
- Dunn, C.G. (1966), Acta Met., 14, 221
- Erb, U., Abel, W. and Gleiter, H. (1982), 16, 1317
- Ewing, R.M. (1971), Acta Met., 19, 1359
- Fionova, L.K., Andreeva, A.V. and Zhukova, T.I. (1981), Phys. Stat.  
Sol. (a), 67, K15
- Fischmeister, H.F. (1985), J. Physique, 46, C4-3
- Frank, F.C. (1950), "Proceedings of the Symposium on Plastic  
Deformation of Crystalline Solids", Office of Naval Research,  
Pittsburgh, p.150
- Frank, F.C. (1963), "Metal Surfaces: Structure, Energetics and  
Kinetics", edited by N.A. Gjostein and W.D. Robertson, (Metals  
Park, Ohio: American Society for Metals), Chapter 1
- Fullman, R.L. (1951), J. Appl. Phys., 22, 456
- Fullman, R.L. and Fisher, J.C., *ibid.* 1350
- Gifkins, R.C. (1969), "Melbourne Interfaces Conference", edited by  
R.C. Gifkins, (Australian Inst. of Metals), p.29
- Gilman, J.J. (1960), J. Appl. Phys., 31, 2208
- Gjostein, N.A. (1963), Acta Met., 11, 969

- Gjostein, N.A. (1969), Scripta Met., 3, 1
- Gjostein, N.A. and Rhines, F.N. (1959), Acta Met., 7, 319
- Gleiter, H. (1970), Acta Met., 18, 23
- Gleiter, H. (1971), Phys. Stat. Sol. (b), 45, 9
- Gleiter, H. (1982), "Interfacial Aspects of Phase Transformations",  
edited by B. Mutaftschiev, (D. Reidel Publishing Company), p.199
- Gleiter, H. and Chalmers, B. (1972), Prog. Mater. Sci., 16, Chapters 1  
and 2
- Goodhew, P.J., Tan, T.Y. and Balluffi, R.W. (1978), Acta Met., 26, 557
- Goodhew, P.J. (1980), "Grain Boundary Structure and Kinetics", edited  
by R.W. Balluffi, (Metals Park, Ohio: American Soc. for Metals),  
p.155
- Grimmer, H., Bollmann, W. and Warrington, D.H. (1974), Acta Cryst.,  
A30, 197
- Gruber, E. (1963), quoted in Gjostein, N.A. (1963), Acta Met., 11, 957
- Hasson, G.C. and Goux, C. (1971), Scripta Met., 5, 889
- Harrman, G., Gleiter, H. and Baro, G. (1976), Acta Met., 24, 353
- Herring, C. (1951), "Physics of Powder Metallurgy", edited by W.E.  
Kingston, (New York: McGraw-Hill), p.143; and Phys. Rev., 82, 87
- Hess, J.B. (1952), "Metal Interfaces", (Metals Park, Ohio: American  
Society for Metals), p.134
- Hodgson, B.K. (1972), Ph.D. Thesis, Uni. of Warwick
- Hodgson, B.K. and Mykura, H. (1973), J. Mater. Sci., 8, 565
- Handros, E.D. (1969), "Melbourne Interfaces Conferences", edited by  
R.C. Gifkins, (Australian Institute of Metals), p.77
- Handros, E.D. (1970), "Techniques of Metals Research", edited by R.F.  
Bunshah, (Interscience Publishers), Volume IV, p.293

- Howell, P.R. and Bee, J.V. (1978), J. Mater. Sci., 13, 1585
- Innan, M.C., McLean, D. and Tipler, H.R. (1963), Proc. Roy. Soc. A273, 538
- Innan, M.C. and Tipler, H.R. (1963), Met. Rev., 8, 105
- Johari, O. and Thomas, G. (1969), "Technique of Metals Research", edited by R.F. Bunshah, (Interscience Publishers), Volume IIA, Chapter 2
- Joy, D.C. (1974), "Quantitative Scanning Electron Microscope", (London: Academic), p.131
- Joy, D.C. and Booker, G.R. (1972), "Proceedings of the 5th Annual Stereoscan Colloquium", (Cambridge Scientific Company, Chicago), p.77
- Joy, D.C. and Maruszevski, C.M. (1975), J. Mater. Sci., 10, 178
- Joy, D.C., Newbury, D.E. and Davidson, D.L. (1982), J. Appl. Phys., 53, R81
- Kopecki, CH.V., Novikov, V. YU, Fionova, L.R. and Bolshakova, N.A. (1985), Acta Met., 33, 873
- Lange, F.F. (1967), Acta Met., 15, 311
- Masteller, M.S. and Bauer, C.L. (1976), Scripta Met., 10, 1033
- Matthews, J.W. (1962), Phil. Mag., 7, 915
- Maurer, R. and Gleiter, H., Scripta Met., 19, 1009
- McLean, D. (1957), "Grain Boundaries in Metals", (Oxford: Oxford University Press)
- McLean, M. (1973), J. Mater. Sci., 8, 571
- McLean, M. and Mykura, H. (1965), Acta Met., 13, 1291
- McLean, M. and Mykura, H. (1966), Phil. Mag., 14, 1191



- Meijering, J.L. (1963), Acta Met., 11, 847
- Miller, W.A. and Williams, W.M. (1967), Acta Met., 15, 1077
- Moore, A.J.W. (1963), "Metal Surfaces: Structure, Energetics and Kinetics", (Metals Park, Ohio: American Society for Metals).

Chapter 5

- Mullins, W.W. (1956), Acta Met., 4, 421
- Mullins, W.W. (1957), J. Appl. Phys., 28, 333
- Mullins, W.W. (1958), Acta Met., 6, 414
- Mullins, W.W. (1960), Trans. AIME, 218, 354
- Mullins, W.W. (1963), "Metal Surfaces: Structure, Energetics and Kinetics, (Metals Park, Ohio: American Society for Metals).

Chapter 2

- Mullins, W.W. and Sekerka, R.F. (1962), J. Phys. Chem. Solids, 23, 801
- Murr, L.E. (1968), Acta Met., 16, 1127
- Murr, L.E. (1969), Phil. Mag., 20, 1245
- Murr, L.E. (1972), Scripta Met., 6, 203
- Murr, L.E., Horylev, R.J. and Wong, G.I. (1971), Surf. Sci., 26, 184
- Mykura, H. (1954), Proc. Phys. Soc., B67, 281
- Mykura, H. (1957), Acta Met., 5, 346
- Mykura, H. (1958), Bulletin Inst. Met., 4, 102
- Mykura, H. (1961), Acta Met., 9, 570
- Mykura, H. (1966), "Solid Surfaces and Interfaces", edited by L. Jacob, (London: Routledge and Kegan Paul Ltd.), Solid-State Physics, p.17
- Mykura, H. (1979), Acta Met., 27, 243

- Mykura, H. (1980), "Grain Boundary Structure and Kinetics", edited by R.W. Belluffi, (Metals Park, Ohio: American Society for Metals), p.445
- Mykura, H. and Gleiter, H. (1979), Scripta Met., 13, 137
- Mykura, H. and Rhead, G.E. (1963), J. Sci. Inst., 40, 313
- Nakagawa, S. (1986), JEOL News, 24B-1, 7
- Pond, R.C. and Smith, D.A. (1977), Scripta Met., 11, 77
- Pumphrey, P.H. (1972), Scripta Met., 6, 107
- Pumphrey, P.H. (1976), "Grain Boundary Structure and Properties", edited by G.A. Chadwick and D.A. Smith, (New York: Academic Press), p. 139
- Read, W.T. (1953), "Dislocations in Crystals", (New York: McGraw-Hill)
- Read, W.T. and Shockley, W. (1950), Phys. Rev., 78, 275
- Robertson, W.M. and Shewmon, P.G. (1962), Trans AIME, 224, 804
- Robinson, A.L. (1986), Science, 233, 842
- Sargent, C.M. (1968), Trans AIME, 242, 1188
- Sauter, H., Gleiter, H. and Baro, G. (1977), Acta Met., 25, 467
- Schulson, E.M. (1977), J. Mater. Sci., 12, 1071
- Shewmon, P.G. (1966), "Recrystallization, Grain Growth and Textures", edited by H. Margolin, (Metals Park, Ohio: American Society for Metals), p.165
- Smith, C.S. (1948), J. Inst. Metals, 74, 747
- Smith, D.A. and Pond, R.C. (1976), Inter. Met. Rev. 205, 61
- Stuwe, H.P. (1978), "Recrystallization of Metallic Materials", edited by F. Haessner, (Stuttgart: Dr. Riederer-Verlag GmbH), p.11
- Sukhomlin, G.D. (1982), Fiz. Metall. Metalloved, 54, 178

- Sutton, A.P. (1984), *Inter. Met. Rev.*, 29, 377
- Thomas, G. (1970), "Modern Diffraction and Imaging Techniques in Material Science", edited by S. Amelinckx, R. Gevers, G. Remant and J. Van Landuyt, (Amsterdam: North Holland), p.159
- Tolmon, F.R. and Wood, J.G. (1956), *J. Sci. Instr.*, 33, 236
- Udin, H. (1952), "Metal Interfaces", (Metals Park, Ohio: American Society for Metals), p. 114
- Van der Merwe, J.H. (1952), *Proc. Roy. Soc. (London)*, A212, 576
- Van Essen C.G. and Verhoeven, J.D. (1974), *J. Phys. E*, 7, 768
- Van Vlack, L.H. (1951), *Trans AIME*, 191, 251
- Vaughan, D. (1970), *Phil. Mag.*, 22, 1003
- Verhoeven, J.D. and Gibson, E.D. (1975), *J. Phys. E*, 8, 15
- Vlachavas, O.S. (1985), *Acta Cryst.*, A41, 530
- Warrington, D.M. and Grimmer, H. (1974), *Phil. Mag.*, 30, 461

THE BRITISH LIBRARY DOCUMENT SUPPLY CENTRE

TITLE

GRAIN BOUNDARY ENERGIES  
IN COPPER

AUTHOR

RAMLI OMAR

INSTITUTION  
and DATE

University of Warwick 1984

Attention is drawn to the fact that the copyright of  
this thesis rests with its author.

This copy of the thesis has been supplied on condition  
that anyone who consults it is understood to recognise  
that its copyright rests with its author and that no  
information derived from it may be published without  
the author's prior written consent.

|     |   |   |   |   |   |
|-----|---|---|---|---|---|
| 1   | 2 | 3 | 4 | 5 | 6 |
| cms |   |   |   |   |   |

THE BRITISH LIBRARY  
DOCUMENT SUPPLY CENTRE  
Boston Spa, Wetherby  
West Yorkshire  
United Kingdom

20

REDUCTION X .....

CAMERA

8

D85765